The Duration and Characteristics of Magmatic Differentiation from Basalt to Trachyte within the Matan Volcanic Center, Northern Harrat Rahat, Kingdom of Saudi Arabia

Chapter F of

Active Volcanism on the Arabian Shield—Geology, Volcanology, and Geophysics of Northern Harrat Rahat and Vicinity, Kingdom of Saudi Arabia

U.S. Geological Survey Professional Paper 1862
Saudi Geological Survey Special Report SGS–SP–2021–1

U.S. Department of the Interior
U.S. Geological Survey

Cover. Aerial view (facing southeast) of the crater that formed during the eruption of the trachyte of Gura 3 at 142.4±2.2 thousand years ago. This eruption produced a 0.6-kilometer-diameter crater and pyroclastic-flow deposits that reached at least 3 kilometers from the source crater. Features in the background consist of cryptodomes, lava spines, block-and-ash-flow deposits, pyroclastic-flow deposits, and scoria cones of several nearby units. Light yellowish-tan sediment on crater floor is alluvium. U.S. Geological Survey photograph by Hannah Dietterich, 2016. Background image shows northern Harrat Rahat lava flows, maars, and lava domes. U.S. Geological Survey photograph by Andrew Calvert, January 25, 2012.

The Duration and Characteristics of Magmatic Differentiation from Basalt to Trachyte within the Matan Volcanic Center, Northern Harrat Rahat, Kingdom of Saudi Arabia

By Mark E. Stelten, Drew T. Downs, Hannah R. Dietterich, Gail A. Mahood, Andrew T. Calvert,
Thomas W. Sisson, Molly R. Witter, Hani M. Zahran, and Jamal Shawali

Chapter F of

Active Volcanism on the Arabian Shield—Geology, Volcanology, and Geophysics of Northern Harrat Rahat and Vicinity, Kingdom of Saudi Arabia

Edited by Thomas W. Sisson, Andrew T. Calvert, and Walter D. Mooney

U.S. Geological Survey Professional Paper 1862
Saudi Geological Survey Special Report SGS–SP–2021–1

U.S. Department of the Interior
U.S. Geological Survey

U.S. Geological Survey, Reston, Virginia: 2023

Suggested citation:
Stelten, M.E., Downs, D.T., Dietterich, H.R., Mahood, G.A., Calvert, A.T., Sisson, T.W., Witter, M.R., Zahran, H.M., and Shawali, J., 2023, The duration and characteristics of magmatic differentiation from basalt to trachyte within the Matan volcanic center, northern Harrat Rahat, Kingdom of Saudi Arabia, chap. F *of* Sisson, T.W., Calvert, A.T., and Mooney, W.D., eds., Active volcanism on the Arabian Shield—Geology, volcanology, and geophysics of northern Harrat Rahat and vicinity, Kingdom of Saudi Arabia: U.S. Geological Survey Professional Paper 1862 [also released as Saudi Geological Survey Special Report SGS–SP–2021–1], 56 p., https://doi.org/10.3133/pp1862F.

Associated data for this publication:
Stelten, M.E., 2021, Ar isotope data for volcanic rocks from the northern Harrat Rahat volcanic field and surrounding area, Kingdom of Saudi Arabia: U.S. Geological Survey data release, https://doi.org/10.5066/P92FB6AQ.

Stelten, M.E., and Downs, D.T., 2022, Electron microprobe data for plagioclase, olivine, pyroxene, and spinel in volcanic rocks from the Matan volcanic center located within the Harrat Rahat volcanic field, Kingdom of Saudi Arabia: U.S. Geological Survey data release, https://doi.org/10.5066/P9ENRS8U.

ISSN 1044-9612 (print)
ISSN 2330-7102 (online)

هيئة المساحة الجيولوجية السعودية
SAUDI GEOLOGICAL SURVEY

Ministry of Industry and Mineral Resources
BANDAR BIN IBRAHIM BIN ABDULLAH AL-KHORAYEF, Minister and SGS Chairman

Saudi Geological Survey
Abdullah bin Mufter Al-Shamrani, Chief Executive Officer

Saudi Geological Survey, Jiddah, Kingdom of Saudi Arabia: 2023

Contents

Figures

Tables

Conversion Factors

International System of Units to U.S. customary units

Multiply	By	To obtain
	Length	
centimeter (cm)	0.3937	inch (in.)
millimeter (mm)	0.03937	inch (in.)
meter (m)	3.281	foot (ft)
kilometer (km)	0.6214	mile (mi)
kilometer (km)	0.5400	mile, nautical (nmi)
meter (m)	1.094	yard (yd)
	Volume	
cubic kilometer (km^3)	0.2399	cubic mile (mi^3)
	Mass	
gram (g)	0.03527	ounce, avoirdupois (oz)
	Density	
gram per cubic centimeter (g/cm^3)	62.4220	pound per cubic foot (lb/ft^3)

Temperature in degrees Celsius (°C) may be converted to degrees Fahrenheit (°F) as follows:

$$°F = (1.8 \times °C) + 32.$$

Abbreviations

C.E.	Common Era
DI	deionized
EMP	electron microprobe
ICP-AES	inductively coupled plasma atomic emission spectrometry
ICP-MS	inductively coupled plasma mass spectrometry
ka	kilo-annum
k.y.	thousand years
LOI	loss on ignition
Ma	mega-annum
mASL	meter above sea level
mg	milligram
mm/k.y.	millimeter per thousand years
µm	micrometer
MSWD	mean square of weighted deviates
nA	nanoampere
ppm	part per million
PRIME	Purdue Rare Isotope Measurement
s	second
XRF	X-ray fluorescence
±	plus or minus

Active Volcanism on the Arabian Shield
Edited by T.W. Sisson, A.T. Calvert, and W.D. Mooney
U.S. Geological Survey Professional Paper 1862
Saudi Geological Survey Special Report SGS–SP–2021–1

Chapter F

The Duration and Characteristics of Magmatic Differentiation from Basalt to Trachyte within the Matan Volcanic Center, Northern Harrat Rahat, Kingdom of Saudi Arabia

By Mark E. Stelten,[1] Drew T. Downs,[1] Hannah R. Dietterich,[1] Gail A. Mahood,[2] Andrew T. Calvert,[1] Thomas W. Sisson,[1] Molly R. Witter,[2] Hani M. Zahran,[3] and Jamal Shawali[3]

Abstract

A fundamental goal of igneous petrology is to quantify the durations required to produce evolved magmas following influx of basalt into the crust. However, in many cases, complex field relations and (or) the presence of a long-lived magmatic system make it difficult to assess how basaltic inputs relate to more evolved magmas, therefore precluding calculation of meaningful timescales. Here we present field relations, geochemistry, ^{40}Ar/^{39}Ar ages, and ^{36}Cl surface-exposure ages for volcanic rocks from the Matan volcanic center, located in the northern part of the Harrat Rahat volcanic field, in the Kingdom of Saudi Arabia. These data document a systematic and repeated temporal progression from alkali basalt to trachyte for the youngest eruptive products. From ~155–17 thousand years ago, the following eruptive sequence occurred four times: (1) alkali basalt, (2) hawaiite, mugearite, or benmoreite, and (3) trachyte. We interpret each eruptive sequence to result from injection of basalt into the crust, and its subsequent differentiation and eruption of progressively evolved magmas. We use the interval time between successive eruptions within a given sequence to calculate the timespans required to produce trachyte from alkali basalt. Differentiation from alkali basalt to intermediate compositions (hawaiite, mugearite, and benmoreite) took ≤3 thousand years (k.y.) on average. Differentiation from intermediate compositions to trachyte took a maximum of 6.7±3.6 to 22.9±1.7 k.y. Thus, the total duration of differentiation was ~10–25 k.y. Timescales presented here are independent of the processes evoked to drive differentiation because they are based solely on the ages and compositions of eruptive products from a system characterized by a simple, repeated differentiation sequence.

Introduction

The generation of evolved magmas in subduction zones or extensional tectonic settings is typically driven by the input of basaltic magmas into the crust. As such, a fundamental goal of igneous petrology is to quantify the duration of time needed to produce evolved magmas after the injection of basalt into the crust. In most natural systems, constraining the duration of time over which evolved magmas were generated is not straightforward. Complex spatio-temporal field relations at a given volcanic field, such as alternating compositions of eruptive products through time that is common in arc systems (for example, Fierstein and others, 2011; Calvert and others, 2018), make it difficult to assess how evolved magmas are temporally related to the input of basaltic magmas in the crust. It has long been known that basaltic magmas are underrepresented at the surface in arc systems because of fractionation at depth and crustal assimilation (Hildreth and Moorbath, 1988). Indeed, eruption of basalt is commonly hampered in rhyolitic systems (for example, Yellowstone Plateau volcanic field or the Taupo volcanic zone), where the presence of a large volume of low-density rhyolite prevents basalts from reaching the surface. Additionally, open-system processes in long-lived or large-volume magma reservoirs can result in complex petrogenetic histories for a given batch of magma (for example, Hildreth and others, 1991; Eppich and others, 2012), making it difficult to directly assess the timescales of magmatic differentiation.

In this contribution, we characterize the nature and duration of magmatic differentiation from alkali basalt to trachyte at Harrat Rahat, which is an alkalic volcanic field in the west-central part of the Kingdom of Saudi Arabia (fig. 1) investigated as part of a larger joint project between the Saudi Geological Survey and the U.S. Geological Survey to study volcanism on the Arabia Plate in the vicinity of Al Madīnah al Munawarrah. Volcanism at Harrat Rahat has persisted since ~10 million years ago (Ma), predominantly erupting basalt throughout its lifetime. The most recent eruption in

---

[1] U.S. Geological Survey.

[2] Stanford University.

[3] Saudi Geological Survey.

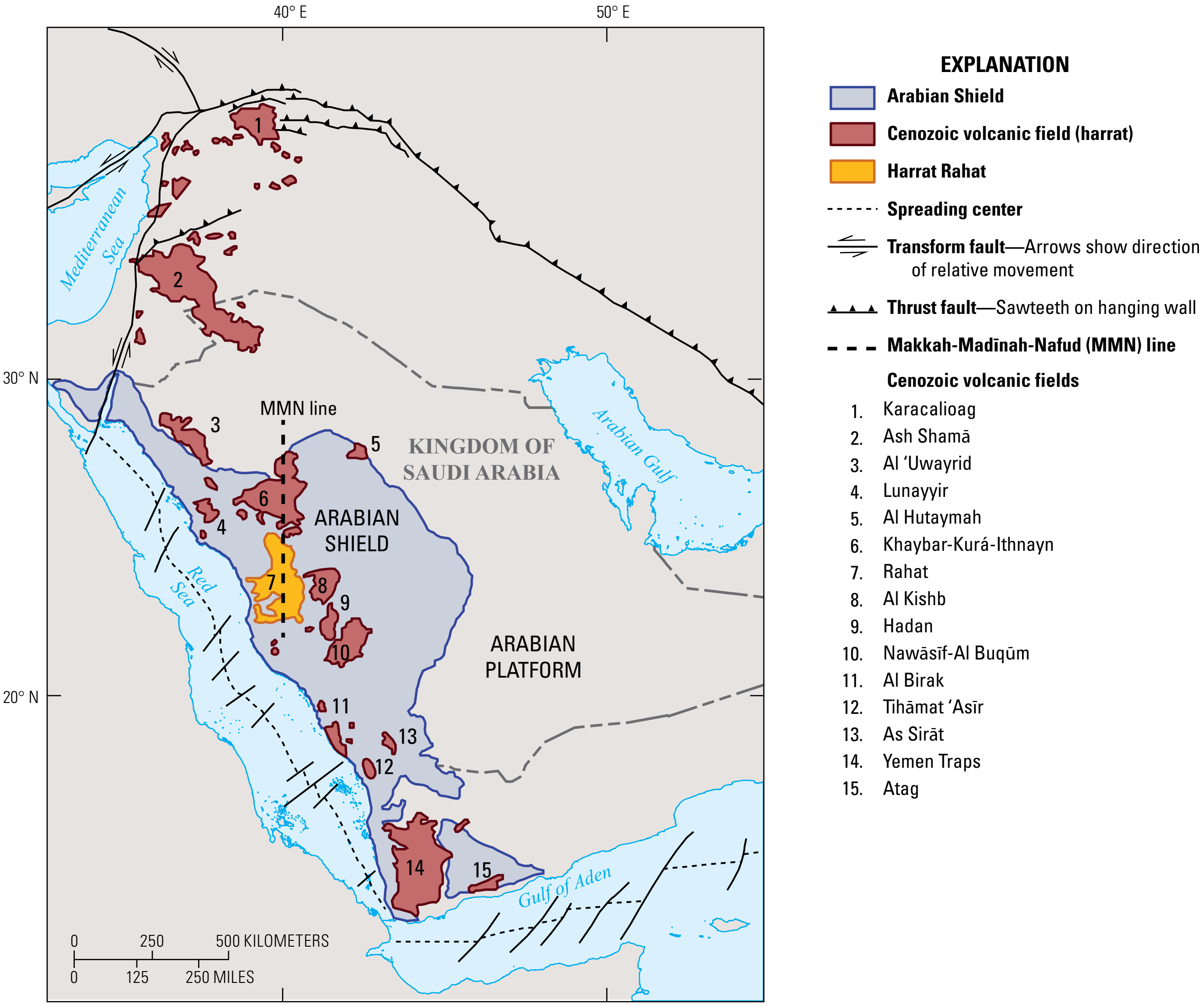

Figure 1. Map of the Kingdom of Saudi Arabia and the surrounding tectonic setting. Red areas show Cenozoic volcanic fields; Harrat Rahat is highlighted in orange (no. 7). Proterozoic rocks of the Arabian Shield are shown in purple and major regional tectonic features (from Stern and Johnson, 2010) are also shown. The Makkah-Madīnah-Nafud (MMN) volcanic line is defined by north trending linear vent systems that mark the main vent axes of Harrats Rahat, Khaybar, and Ithnayn (for example, Camp and Roobol, 1992). Locations of Cenozoic lava fields are from Coleman and others (1983) and Camp and Roobol (1989).

1256 C.E. produced a basaltic lava flow in the northern part of the volcanic field (fig. 2; Camp and Roobol, 1989; Moufti and others, 2013). For several reasons, Harrat Rahat presents an ideal opportunity to quantify the durations required to produce evolved alkalic magmas following the injection of basalt into the crust. First, field relations demonstrate that most trachytes are present among the stratigraphically youngest eruptive products within Harrat Rahat (Camp and Roobol, 1989, 1991). The region lacks a Quaternary caldera or calderas, large-volume ignimbrites, significant hydrothermal activity, or silicic magmas erupted over long time periods that would indicate a persistently active, sizeable silicic crustal magma body or silicic magmatic system (Camp and Roobol, 1989, 1991). These observations indicate that a long-lived silicic magmatic system was not present at Harrat Rahat prior to the most recent episode of volcanism. Second, prior work at Harrat Rahat demonstrates that mugearite, benmoreite, and trachyte eruptive products are isotopically similar to the basalts (Moufti and others, 2012), and, therefore, it is likely that the evolved magmas are derived from basalt by

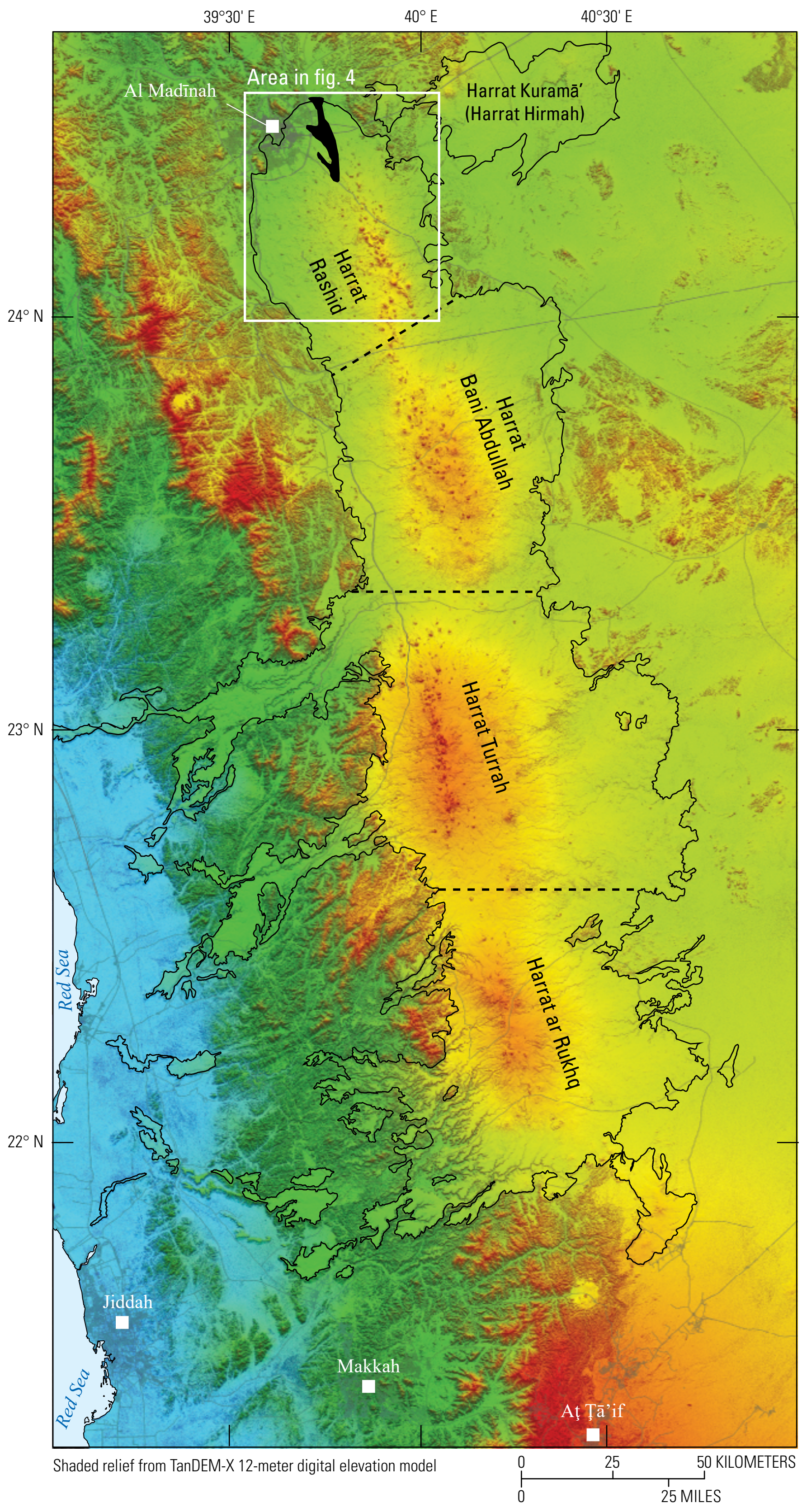

Shaded relief from TanDEM-X 12-meter digital elevation model

Figure 2. Color shaded-relief map of Harrat Rahat (outlined in black) and the surrounding region. Four distinct harrats make up Harrat Rahat, each of which are characterized by an elongate, shield-shaped morphology centered around a north- to north-northwest-trending main vent axis. Located just east of northernmost Harrat Rahat is Harrat Kuramā´ (also known as Harrat Hirmah) (Pellaton, 1981; Coleman and others, 1983). The historical (1256 C.E.) basaltic lava flow in northernmost Harrat Rahat is shown in black.

partial melting or crystallization differentiation, with only minor crustal assimilation (Salters and others, 2023). Third, field relations document a repeated, systematic temporal progression from basalt to trachyte in the youngest Harrat Rahat eruptive products, which is consistent with the injection of basalt into the crust and its subsequent differentiation to form evolved magmas.

We use these field relations and isotopic characteristics along with new $^{40}Ar/^{39}Ar$ eruption ages, ^{36}Cl cosmogenic surface-exposure ages, and geochemical data to constrain the durations of magmatic differentiation from alkali basalt to trachyte. Additionally, we provide the first detailed characterization of the composition of mineral phases hosted in basaltic through trachytic magmas at Harrat Rahat, which provides valuable information for understanding the geochemical evolution of Harrat Rahat magmas.

Geologic Background

The Arabian Peninsula hosts at least 16 Cenozoic harrats (Arabic for basaltic lava field) that stretch ~3,000 kilometers (km) from the Gulf of Aden to northeast of the Mediterranean Sea (fig. 1). Broadly, Cenozoic volcanism on the Arabia Plate can be divided into two periods. An older period of volcanism associated with first-stage spreading of the Red Sea between 30 and 15 Ma is fundamentally tholeiitic, although local extrusion of continental alkali basalt flows occurred at Harrat as Sirāt and Harrat Hadan (fig. 1) (Almond, 1986a,b; Camp and Roobol, 1989). In contrast, volcanism after 15 Ma is dominantly alkalic, and most volcanism has occurred along the Makkah-Madīnah-Nafud line (fig. 1), which is defined by the north-trending linear vent systems of Harrats Rahat, Khaybar, and Ithnayn, which have smaller and more alkaline fields flanking to the southeast and northwest (Coleman and others, 1983; Camp and Roobol, 1992). The driving force behind volcanism in the younger (<15 Ma) harrats remains unclear, but has variously been attributed to (1) uplift and extension associated with impingement of the Afar mantle plume on the lithosphere (Almond, 1986b; Camp and Roobol, 1989, 1992), (2) melting related to Red Sea rifting and left-lateral movement along the Aqaba-Dead Sea transform boundary (Coleman and McGuire, 1988; Stein and Hofmann, 1992; Bosworth and others, 2005; Moufti and others, 2012), or (3) regional lithospheric thinning coupled with northward flow of hot asthenosphere related to the Afar plume (Duncan and others, 2016). Harrat Rahat volcanic rocks have distinct isotopic compositions relative to the Afar plume and any direct involvement of the Afar plume in the formation of the Harrat Rahat magmas is likely minor (Bertrand and others, 2003; Shaw and others, 2003; Moufti and others, 2012; Salters and others, 2023). Although the exact cause for volcanism over the past ~15 million years is unclear, most models (described above) suggest that volcanism in the Arabian harrats is driven by decompression melting, possibly in concert with a temperature increase from the upwelling Afar plume.

The Harrat Rahat volcanic field, which has a total erupted volume of ~2,000 cubic kilometers (km^3) (Camp and Roobol, 1989), is one of the largest of the Arabian harrats. Harrat Rahat is primarily basaltic and consists of a 75-km-wide volcanic plateau extending ~310 km north-south between the cities of Makkah and Al Madīnah al Munawwarah (Camp and others, 1987; Camp and Roobol, 1989). Unlike tholeiitic basalts associated with the Red Sea spreading center, volcanism that comprises the Arabian harrats is generally alkalic (fig. 3). Harrat Rahat itself coalesced from four smaller harrats, which are each characterized by an elongate, shield-shaped morphology centered around a north- to north-northwest-trending axis of vents (fig. 2). Initiation of volcanism at each of these harrats is inferred to have been broadly contemporaneous at ~10 Ma (Camp and Roobol, 1989; Moufti and others, 2013). However, a concentration of minimally eroded lava flows and vent complexes indicates that the northernmost part of Harrat Rahat, also known as Harrat Rashid or Harrat Al Madīnah, hosted the most recent eruptive phase, including a historically documented eruption of basalt in 1256 C.E. (fig. 2; Camp and others, 1987; Camp and Roobol, 1989; Moufti and others, 2012, 2013).

More than 230 distinct eruptive units are exposed in northern Harrat Rahat (Pellaton, 1981; Coleman and others, 1983; Camp and Roobol, 1989, 1991; Downs and others, 2019; Robinson and Downs, 2023). Camp and Roobol (1989, 1991) assigned relative ages to eruptive units in northern Harrat Rahat based largely on geomorphic criteria, such as degree of weathering and the amount of sediment accumulated on the surface of lava flows. Because of the scale of their mapping and the limited geochronology available at the time, the geomorphic age groups suggested by Camp and Roobol (1989, 1991) for northern Harrat Rahat were anchored by only eight K-Ar ages. Camp and Roobol (1989, 1991) suggested that the oldest volcanic deposits in northern Harrat Rahat erupted between ~2.5 and 1.7 Ma, and that most eruptions occurred before 600 thousand years ago (ka). Moufti and others (2013) reassessed the age of volcanic deposits in northern Harrat Rahat by measuring 25 $^{40}Ar/^{39}Ar$ ages. These $^{40}Ar/^{39}Ar$ ages largely support the age groups proposed by Camp and Roobol (1989, 1991), except that Moufti and others (2013) suggested volcanism in northern Harrat Rahat began at ~10 Ma. More recently, Downs and others (2018) measured 19 $^{40}Ar/^{39}Ar$ ages and 3 ^{36}Cl surface-exposure ages from volcanic strata exposed at the northwest terminus of Harrat Rahat, near the city of Al Madīnah, and demonstrated that volcanism in this area occurred from at least 1,014±14 ka (1σ uncertainty) to 1256 C.E.

Volcanic products within Harrat Rahat consist of alkalic and transitional basalts (hereafter referred to collectively as basalt), hawaiites, mugearites, benmoreites, and trachytes (fig. 3). Volumetrically, Harrat Rahat is dominated by basalt (~90 percent) accompanied by subequal amounts of hawaiite, mugearite, benmoreite, and trachyte (Camp and Roobol, 1989; Downs, 2019; Sisson and others, 2023). Petrologic studies at Harrat Rahat have largely focused on basaltic magmatism

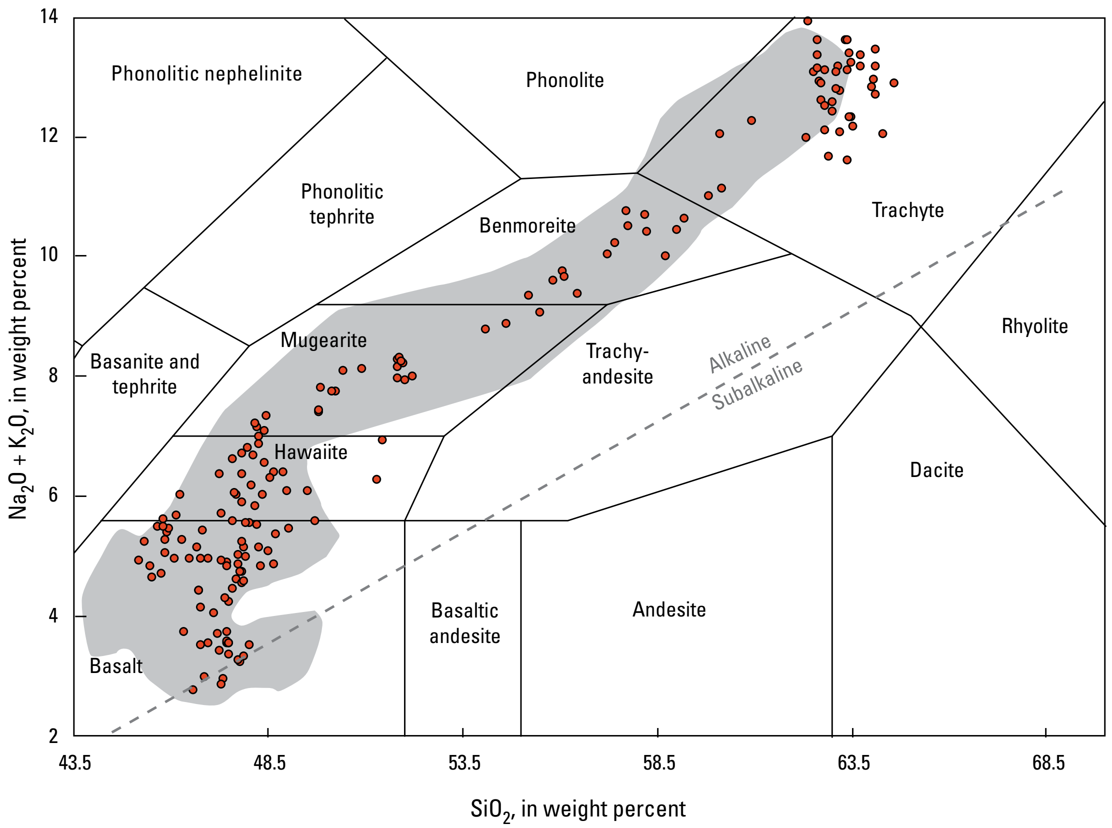

Figure 3. Plot of total alkali ($Na_2O + K_2O$) versus silica (SiO_2) for volcanic rocks from the Matan volcanic center. Note that volcanic rocks from the Matan volcanic center (red dots) span the entire compositional array of the Harrat Rahat volcanic field (gray area). Data for Matan volcanic center eruptive products are from this study and Downs and others (2018), and data for all Harrat Rahat eruptive products are from Downs (2019). Compositional fields are from Cox and others (1979); alkaline-subalkaline line is from Macdonald and Katsura (1964).

(for example, Camp and Roobol, 1989; Moufti and others, 2012; Murcia and others, 2017; Sisson and others, 2023); more evolved compositions have received little attention. Only sparse chemical analyses have been reported for mineral phases hosted in mafic rocks of Harrat Rahat (Camp and others, 1987; Camp and Roobol, 1991; Murcia and others, 2017) and only summaries have been reported for the chemical compositions of minerals in intermediate to silicic rocks (Camp and Roobol, 1991), thus hampering the ability to completely describe chemical differentiation of Harrat Rahat magmas. Major element, trace element, and isotopic data for basalts through trachytes within Harrat Rahat have been used by previous authors to interpret that the more evolved magmas were generated by fractional crystallization of their mafic progenitors with only minor crustal assimilation (Camp and Roobol, 1989; Moufti and others, 2012; Salters and others, 2023; Sisson and others, 2023). However, prior to this study, the timescale of this differentiation process was unconstrained because of the scarcity of high-precision ages of the eruptive products.

Trachytic eruptive products are dominantly located in the northern part of the volcanic field (Harrat Al Madīnah; fig. 2). Most trachytes erupted as Peléan domes with small-volume pyroclastic-flow deposits consisting dominantly of poorly inflated juvenile clasts and lithic clasts that formed as the domes occasionally collapsed. Some trachytes erupted explosively, excavating craters ~0.15–1.8 km in diameter and generating pyroclastic-surge and -flow deposits that extend ~1–10 km from the vent (fig. 4; Moufti, 1985; Camp and Roobol, 1989; Downs and others, 2019). In nearly all cases, the trachytes are among the stratigraphically youngest eruptive products in northern Harrat Rahat (fig. 4; Camp and Roobol, 1989; Downs and others, 2019), and only rarely are trachytes observed in stratigraphically older volcanic deposits. This demonstrates that trachytes dominantly erupted in the more recent history of the northern part of the volcanic field and suggests that no large silicic magmatic systems capable of erupting trachyte were present at Harrat Rahat prior to that time. Prior to this study, the ages of the trachytes were poorly known. Early K-Ar dating yielded ages from trachyte units of 2.13 and 1.47 Ma (Pellaton, 1981), whereas more recent ^{40}Ar/^{39}Ar dating by Moufti and others (2013) yielded an age of 114.4±16.9 ka (2σ uncertainty) for one of the trachytes in northern Harrat Rahat.

Trachyte predominantly erupted from two volcanic centers, the Matan volcanic center and the Al Efairia volcanic center, both located in northern Harrat Rahat (fig. 4). Trachyte additionally erupted from Al Wabarah, located to the southwest of the Al Efairia volcanic center. The Matan and Al Efairia volcanic centers erupted magmas that range in composition from basalt to trachyte. In this study, we present new ^{40}Ar/^{39}Ar ages, ^{36}Cl ages, whole-rock chemical compositions, mineral compositions, and field observations of basalt through trachyte from the Matan volcanic center. These new data place age constraints on the recent eruptive history of the volcanic center, reveal the timescales encompassed by magmatic differentiation from alkali basalt to trachyte, and provide a detailed characterization of the chemical and mineralogical characteristics of Matan volcanic center eruptive products.

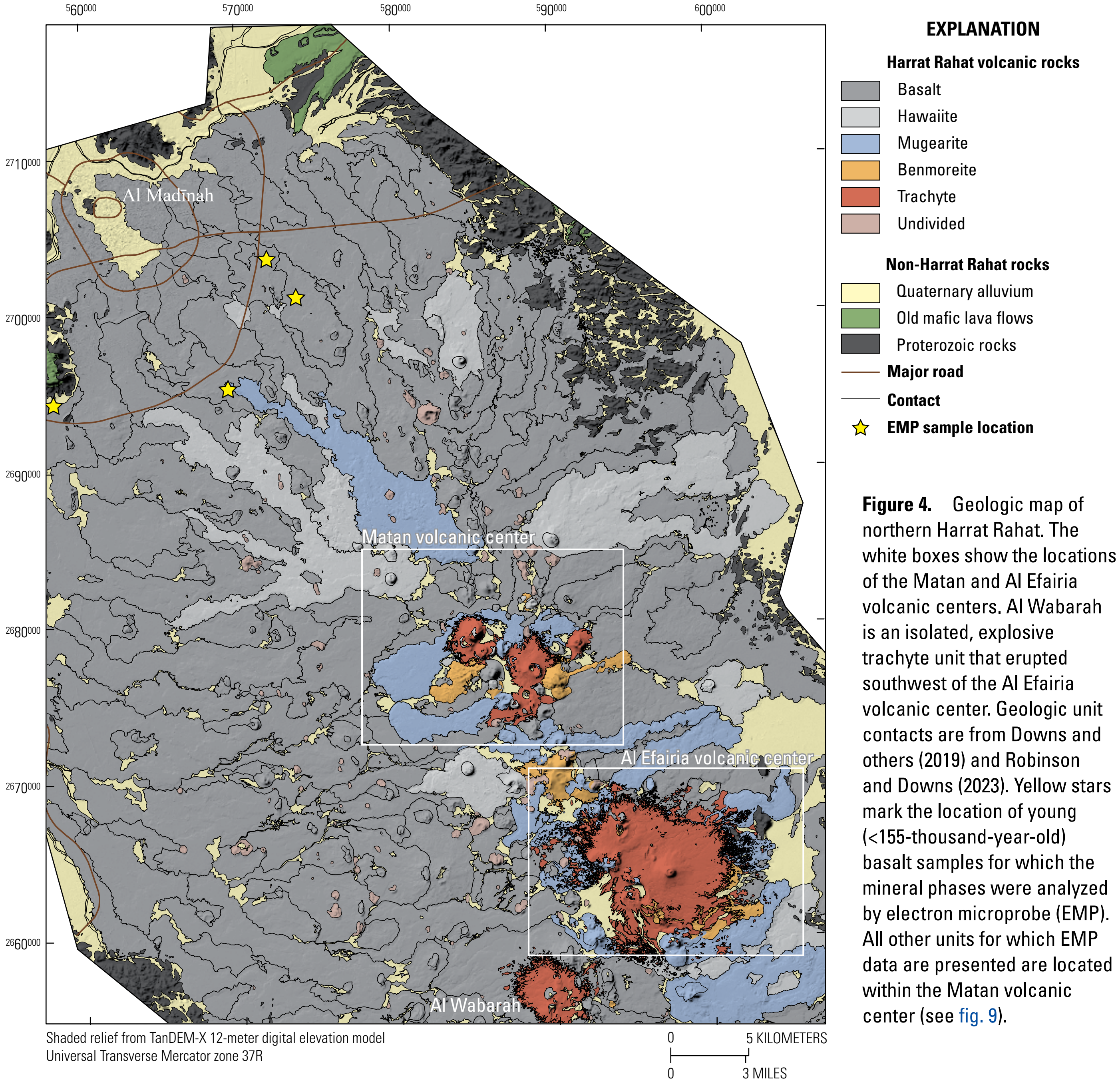

Shaded relief from TanDEM-X 12-meter digital elevation model
Universal Transverse Mercator zone 37R

Figure 4. Geologic map of northern Harrat Rahat. The white boxes show the locations of the Matan and Al Efairia volcanic centers. Al Wabarah is an isolated, explosive trachyte unit that erupted southwest of the Al Efairia volcanic center. Geologic unit contacts are from Downs and others (2019) and Robinson and Downs (2023). Yellow stars mark the location of young (<155-thousand-year-old) basalt samples for which the mineral phases were analyzed by electron microprobe (EMP). All other units for which EMP data are presented are located within the Matan volcanic center (see fig. 9).

Analytical Methods

Whole-Rock Major- and Trace-Element Analyses

Major- and trace-element concentrations for rocks collected during the joint Saudi Geological Survey-U.S. Geological Survey study of northern Harrat Rahat, including 173 samples from the Matan volcanic center, were analyzed by X-ray fluorescence (XRF) spectrometry and inductively coupled plasma mass spectrometry (ICP-MS) at the GeoAnalytical Laboratory at Washington State University in Pullman, Washington, and are reported by Downs (2019). Analyses followed the procedures outlined by Knaack and others (1994) and Johnson and others (1999). Long-term precision for trace-element analysis via ICP-MS is typically better than 5 percent for rare earth elements and better than 10 percent for other trace elements. Prior to submission, samples were chipped to ≤5 millimeters (mm) in diameter, and visibly altered pieces were removed by hand. A few of the mafic lavas contained vesicles filled with zeolite, carbonate, gypsum and anhydrite, clay, or loess, which were analyzed in the absence of any fresher material. Samples with these secondary minerals were first cleaned by heating in deionized (DI) water to 60 degrees Celsius (°C) for an hour to dissolve any gypsum and anhydrite, then heating in DI water to 90 °C for an hour to dissolve any zeolites, and finally put in an ultrasonic bath for ~8 hours to disaggregate and remove any remaining adhering foreign material. Samples containing minor amounts of calcium carbonate were placed in 1-molar HCl for ~30 minutes and then submerged in DI water and ultrasonicated for ~8 hours. These processes were repeated until the samples were free of visible secondary minerals. Analyses of fresh samples and cleaned samples (whose vesicles were previously filled) from the same flows, were compared and showed no evidence of fractionation during the cleaning process.

Electron Microprobe Analyses

Electron microprobe (EMP) chemical compositions of most feldspar, olivine, pyroxene, and Fe-Ti oxide grains were collected with a five-spectrometer JEOL-8900 Superprobe by wavelength dispersive methods. All analyses were made with a 15-kilovolt accelerating voltage and specific conditions: for plagioclase, 10 nanoamperes (nA) faraday current, 10 micrometer (µm) diameter beam; for Fe-Ti-Cr-Al oxide minerals, 20 nA, focused beam; for pyroxene and olivine, 15 nA, focused beam. Count times were 30 seconds (s) per peak and 10 s on positive and negative backgrounds for all elements except sodium, in which case it was 10 s on peak and 5 s on backgrounds. Sodium and potassium were measured first to mitigate loss under the beam. Background-corrected count rates were converted to oxide mass concentrations with the JEOL proprietary version of the CITZAF reduction scheme (Armstrong, 1995).

^{40}Ar/^{39}Ar Dating

Groundmass separates from basalt, hawaiite, mugearite, benmoreite, and trachyte were prepared for dating via the ^{40}Ar/^{39}Ar method. Dense samples with a crystalline groundmass were chosen for analysis. Samples were crushed, ultrasonicated, and sieved to 250–355 µm. Groundmass was separated from phenocrysts using a Frantz magnetic separator and careful handpicking under a binocular microscope. For trachyte and some benmoreite samples, feldspar separates (anorthoclase or sanidine) were prepared from the 250–355-µm-size fraction of crushed whole-rock samples by standard magnetic and density separation techniques. Approximately 150 milligrams (mg) of material was prepared for each groundmass separate and ~50 mg of material for feldspar separates. ^{40}Ar/^{39}Ar ages for groundmass and bulk feldspar separates were measured using a molybdenum crucible in a custom resistance furnace attached to a MAP 216 mass spectrometer at the U.S. Geological Survey in Menlo Park, California. For a subset of samples, ^{40}Ar/^{39}Ar ages were measured for single feldspar crystals (sanidine or anorthoclase) by laser total fusion using a CO_2 laser connected to the same mass spectrometer. ^{40}Ar/^{39}Ar ages are calculated relative to Bodie Hills sanidine with an age of 9.7946±0.0033 Ma, equivalent to Fish Canyon sanidine at 28.0985±0.0126 Ma (Fleck and others, 2019), and using the decay constants of Steiger and Jäger (1977). Uncertainties for reported ^{40}Ar/^{39}Ar ages include propagated uncertainties in counting statistics and J values. Age uncertainties are reported at the 1σ level unless otherwise noted. See appendix 1 for details on analytical methods, irradiation parameters, and data reduction.

^{36}Cl Cosmogenic Surface-Exposure Dating

Two samples for ^{36}Cl surface-exposure dating were collected from the basalt of Musawda’ah (unit bms; all unit symbols used in this study are from Downs and others, 2019, and Robinson and Downs, 2023). Sample R15MS004 is a whole-rock sample collected using a hammer and chisel from a flat surface on the rim of the vent of unit bms and is composed of vesicular basalt with 3–5 percent plagioclase phenocrysts as large as 5 centimeters (cm). Sample R15TS189 consists of 0.5- to 1.5-cm-long plagioclase phenocrysts collected from a flat part of unit bms at ~3.7 km distance from its vent. The plagioclase phenocrysts collected were loose on the surface of the lava flow but are petrographically identical to plagioclase phenocrysts within unit bms and are interpreted to be derived from the top centimeter of the lava flow surface.

Chemical separation and analysis of samples via accelerator mass spectrometry took place at the Purdue Rare Isotope Measurement (PRIME) Laboratory at Purdue University in West Lafayette, Indiana. Splits of each sample were analyzed for their major-element concentrations via wavelength dispersive XRF and their trace-element concentrations via inductively coupled plasma atomic emission spectrometry (ICP-AES) and ICP-MS at the U.S. Geological

Survey in Denver, Colorado, following the methods of Taggart (2002). Cosmogenic surface-exposure ages were calculated using the online CRONUScalc ^{36}Cl Exposure Age Calculator ver. 2.0 (Marrero and others, 2016). Ages were calculated using the Lal and Stone time-independent scaling model (Lal, 1991; Stone, 2000). See appendix 1 for details on analytical methods, sample characteristics, and data reduction methods.

Results

Whole-Rock Major- and Trace-Element Concentrations

We employ 173 whole-rock major- and trace-element analyses from 33 distinct volcanic units in the Matan volcanic center (Downs, 2019; sample numbers in appendix 2). Rock types are classified following Cox and others (1979) to be consistent with recent mapping at Harrat Rahat by Downs and others (2018, 2019) and Robinson and Downs (2023). Eruptive products from the Matan volcanic center range from basalt to trachyte, where SiO_2 ranges from 45.2 to 64.6 weight percent (fig. 3). These new whole-rock chemical analyses are consistent with previously published compositions of Harrat Rahat eruptive products (Camp and others, 1987; Camp and Roobol, 1989; Murcia and others, 2015, 2017). Trachytes in Harrat Rahat plot between the granitic and phonolitic minima in the SiO_2-$NaAlSiO_4$-$KAlSiO_4$ system, as is typical of trachytes around the world (Tuttle and Bowen, 1958; Hamilton and MacKenzie, 1965; Wolff, 2017), and are dominantly nepheline normative.

Mineral Compositions by Electron Microprobe

We present EMP chemical analyses of feldspar (number [*n*] =893), olivine (*n*=400), pyroxene (*n*=212), and Fe-Ti-Cr-Al oxides (*n*=127) hosted in rocks that span the entire compositional spectrum of northern Harrat Rahat. Mineral compositions by EMP are presented in figures 5–8 and reported by Stelten and Downs (2022). EMP mineral compositions were measured as part of a larger survey of mineral chemistry throughout northern Harrat Rahat and, as a result, EMP analyses are not available for all the eruptive units for which ^{40}Ar/^{39}Ar and ^{36}Cl ages are determined. Compositions of minerals hosted in hawaiite, mugearite, benmoreite, and trachyte eruptive products presented in this study are from eruptive units within the Matan volcanic center. EMP analyses were only performed on plagioclase hosted in one basaltic magma in the Matan volcanic center (basalt of Dabaa 1 [unit bd1]). To address this issue, we present EMP analyses from four basalt flows located to the north of the Matan volcanic center (fig. 4) that erupted after 155 ka and are coeval with the eruptive sequences that are the focus of this study. Given the overall compositional similarity of basalts throughout Harrat Rahat, the decoupling of EMP mineral compositions from geochronologic eruption ages does not impede our ability to describe the mineralogical variations observed in Harrat Rahat eruptive products.

^{40}Ar/^{39}Ar Ages and ^{36}Cl Cosmogenic Surface-Exposure Ages

We present 38 new ^{40}Ar/^{39}Ar ages and 2 new ^{36}Cl cosmogenic surface-exposure ages for eruptive products associated with the Matan volcanic center. New ^{40}Ar/^{39}Ar age data are presented in table 1 (full dataset available from Stelten [2021]) and new ^{36}Cl surface-exposure ages are presented in table 2 (full dataset is in appendix 3). Sample compositions used in the calculation of ^{36}Cl surface-exposure ages are presented in table 3. ^{40}Ar/^{39}Ar age spectra and isochron diagrams are presented in appendix 4. Ages, stratigraphic relations, and volumes for eruptive products within the Matan volcanic center are presented in figure 9. Uncertainties for the ages reported hereafter are 1σ unless otherwise specified. In general, ages of volcanic rocks exposed near the Matan volcanic center span from 1,112.1±17.6 to 17.6±1.9 ka. Volcanism before 200 ka was dominated by basalt and hawaiite with intermittent mugearite and benmoreite eruptions whereas volcanism after 155 ka was characterized by basalt, mugearite, benmoreite, and trachyte eruptions (fig. 9). New ^{40}Ar/^{39}Ar dating of trachytes in the Matan volcanic center yields ages from 142.4±2.2 to 17.6±1.9 ka. Although these are not the same trachyte units dated by Pellaton (1981), our new ages are in marked contrast to those of 2.13 and 1.47 Ma reported by Pellaton (1981). Moufti and others (2013) presented an age of 114.4±16.9 ka (2σ) for the trachyte of Gura 3 (unit tg3), which is broadly consistent with our age of 142.4±2.2 ka for this unit.

New ^{36}Cl surface-exposure ages for the whole-rock and plagioclase samples from the basalt of Musawda'ah (unit bms) are 66.0±11.0 ka and 56.5±6.7 ka, respectively. These ages overlap at the 1σ level and yield a weighted mean age of 59.1±5.7 ka, which we take to represent the eruption age of unit bms. These new ^{36}Cl surface-exposure ages are consistent with field relations and previous dating, which demonstrate that unit bms underlies the 51.0±9.0 ka hawaiite of Al Anahi 3 (unit han3) (Downs and others, 2018).

Discussion

Mineralogy of Matan Volcanic Center Eruptive Products

The phenocryst assemblage varies systematically with composition in the Matan volcanic center, and by extension within eruptive products throughout northern Harrat Rahat as well. Basalts and hawaiites are dominated by olivine ± plagioclase phenocrysts. Forsterite (Fo) content of olivine hosted in young (<155 ka) basalts and hawaiites ranges from Fo_{88} to Fo_{51} (fig. 5), and groundmass olivine crystals extend to lower forsterite contents than phenocrysts. Plagioclase hosted in young basalts and hawaiites ranges from bytownite to andesine, and rare groundmass plagioclase extends to more alkalic compositions (fig. 6). In general, olivine from hawaiite has lower average forsterite contents and

Table 1. Summary of ^{40}Ar/^{39}Ar ages for volcanic rocks of the Matan volcanic center.

[Weighted mean ages for samples with multiple analyses, where available, and preferred ages, where one age is available, are shown in bold and noted by a footnote. Initially, ages and mass discrimination were calculated assuming ^{40}Ar/^{36}Ar$_{\text{atmosphere}}$ is 295.5±0.5 (Steiger and Jäger, 1977), but starting in May 2016, the Menlo Park Argon Laboratory began calculating ages and mass discrimination assuming ^{40}Ar/^{36}Ar$_{\text{atmosphere}}$ is 298.56±0.31 (Lee and others, 2006). The change in the assumed ^{40}Ar/^{36}Ar of atmospheric argon does not result in a bias in ages because both monitors and unknowns from each irradiation were calculated in the same manner. Unit names and symbols are from Downs and others (2019). ^{40}Ar/^{36}Ar$_i$, ^{40}Ar/^{36}Ar isochron intercept. ka, kilo-annum; MSWD, mean square of weighted deviates; T, temperature; %, percent]

Sample	Phase analyzed	Method[b]	Plateau age		Isochron age			^{39}Ar, in % [T range, in °C]	^{40}Ar*, in %
			Age ±1σ (ka)	MSWD	Age ±1σ (ka)	MSWD	^{40}Ar/^{36}Ar$_i$ ±2σ		
Trachyte of Dabaa 1 (unit td1)									
R14AC017	Groundmass	IH	16.9±2.9[c]	2.0	26.4±5.5	1.24	292.6±3.3[e]	45.8 [825–1,150]	1.8
	Sanidine	IH	18.1±2.4[c]	0.45	23.7±4.5	0.12	288.5±10.8[e]	56.2 [625–1,050]	8.3
Weighted mean age			**17.6±1.8**[a]						
Trachyte of Mouteen (unit tmo)									
R14TS028	Groundmass	IH	**31.9±2.1**[a]	1.85	35.8±4.6	1.88	294.4±2.4[e]	91.4 [550–1,175]	2.9
Trachyte of Gura 2 (unit tg2)									
R14AC010	Sanidine	IH	94.9±4.2[c]	2.07	95.9±5.4	2.15	293.2±8.3[e]	70.2 [600–1,075]	27.1
	Sanidine	IH	86.7±1.4	0.73	92.9±4.1[e]	0.37	285.2±13.9[e]	73.3 [625–925]	31.7
R14AC086	Sanidine	IH	93.8±3.1[c]	1.63	98.3±7.2	1.63	289.7±17.4[e]	71.8 [650–1,025]	28.6
	Sanidine	IH	94.9±4.2[c]	2.07	95.9±5.4	2.15	293.2±8.3[e]	70.2 [600–1,075]	27.1
Weighted mean age			**93.8±2.1**[a]						
Mugearite of Dabaa 1 (unit md1)									
R14AC019	Groundmass	IH	115.7±3.5[c]	0.70	135.6±21.8	0.78	292.4±7.5[e]	65.8 [650–1,100]	5.8
R14AC021	Groundmass	IH	118.4±4.5[c]	1.41	106.2±6.9	0.92	296.7±2.6[e]	87.6 [625–1,200]	4.5
Weighted mean age			**116.7±2.8**[a]						
Basalt of Shai'ab Abu Sikhbir (unit bsas)									
R14AC068	Groundmass	IH	**115.3±7.5**[a]	1.78	115.5±14.6	2.04	295.4±4.1[e]	91 [550–1,150]	6.0
Trachyte of Matan (unit tma)									
R14TS068	Sanidine	IH	122.3±1.9[c]	1.41	118.5±5.3	1.41	300.0±13.2[e]	69.4 [625–1,050]	33.9
	Groundmass	IH	120.6±2.1[c]	1.81	123.1±6	2.04	294.4±5.1[e]	72.8 [550–925]	14.0
Weighted mean age			**121.5±1.4**[a]						
Benmoreite of Gura 2 (unit og2)									
R14AC090	Groundmass	IH	128.2±4.2	0.55	96±27.3	0.38	303±13.9[e]	36.6 [650–1,100]	9.1
Basalt of Abu Rimthah (unit bar)									
R14AC069	Groundmass	IH	**130.3±5**[a]	0.60	132.7±7.5	0.65	295.0±2.5[e]	90.8 [550–1,100]	7.9
Trachyte of Gura 3 (unit tg3)									
R15MS010	Sanidine	IH	**142.4±2.2**[a]	0.75	143.6±9.9	0.91	294.7±14.2[e]	69.7 [625–950]	23.5
Mugearite of Matan (unit mma)									
R14TS131	Groundmass	IH	154±8.3	1.96	173.4±23.7	1.99	293.8±4.3[e]	61.1 [550–1,125]	4.4

Table 1. Summary of ^{40}Ar/^{39}Ar ages for volcanic rocks of the Matan volcanic center.—Continued

Sample	Phase analyzed	Method[b]	Plateau age		Isochron age			^{39}Ar, in % [T range, in °C]	^{40}Ar*, in %
			Age ±1σ (ka)	MSWD	Age ±1σ (ka)	MSWD	^{40}Ar/^{36}Ar$_i$ ±2σ		
Basalt of Sha'ib Iskabah (unit bsi)									
R14TS033	Groundmass	IH	138.1±17.2[c]	2.15	67.5±110.3	2.5	302.5±25.4[e]	45.7 [550–1,050]	4.5
	Groundmass	IH	158.7±12.1[c]	1.51	217.3±35.3	1.12	287.4±10.4[e]	47.6 [550–1,075]	7.1
Weighted mean age			**151.9±9.9**[a]						
Mugearite of Al Mulaysa (unit mmu)									
R14AC096	Groundmass	IH	220.6±5.1[c]	0.82	258.7±29.3	0.69	287.8±13[e]	54.9 [675–1,150]	12.5
R14TS074	Groundmass	IH	226.8±3.4[c]	1.72	207.2±15.5	1.63	299.5±7.1[e]	100 [550–1,375]	14.6
R14TS081	Groundmass	IH	246.2±5.2	2.19	200.4±28.1[c]	1.71	304.7±12.9[e]	85 [825–1,275]	14.6
R14TS082	Groundmass	IH	211.9±3.5[c]	1.32	203.8±5.6	1.09	297.1±1.9[e]	77.5 [550–1,125]	12.4
Weighted mean age			**219.6±4**[a]						
Basalt of Ad Darah (unit bda)									
R14TS130	Groundmass	IH	**223±18.9**[a]	1.47	162.9±28.7	0.86	298.0±2.3[e]	99.3 [550–1,300]	3.2
Basalt of Al Malsaa 1 (unit bm1)									
R15MS042	Groundmass	IH	**230.7±4.4**[a]	1.07	226.1±9.1	1.22	296.9±6.4[e]	89.3 [550–1,125]	22.3
Basalt of Sha'ib Hayaya (unit bhy)									
R15TS202	Groundmass	IH	**235.1±7.5**[a]	1.43	233.5±20.6	1.63	295.6±5.8[e]	99.7 [550–1,250]	9.7
Hawaiite of Mouteen (unit hmo)									
R14TRO029	Groundmass	IH	**239±4.1**[a]	0.52	237±5.6	0.57	296.0±2.4[e]	81.2 [550–1,200]	19.6
Benmoreite of Al Bayadah (unit oba)									
R14TS083	Groundmass	IH	**242.8±2.4**[a]	1.73	255.5±6.8	1.37	291.7±4.2[e]	92.6 [600–1,250]	19.5
Basalt of Amlit 1 (unit bam1)									
R15MS003	Groundmass	IH	264±7.2	2.05	**252.2±6.8**[a]	1.15	300.6±1.7[f]	100 [550–1,300]	14.1
Basalt of Upper Abu Rimthah (unit burr)									
R14DS068	Groundmass	IH	362.8±12.2[c]	0.86	255.5±91.3	0.69	308.4±18.5[f]	60.5 [875–1,225]	10.0
R16MS070	Groundmass	IH	371.5±14.4[c]	1.94	350.7±85.9	2.21	300.4±18.1[f]	78.4 [700–1,150]	10.9
Weighted mean age			**366.4±9.3**[a]						
Benmoreite of Um Junb (unit oju, dome 2)									
R14AC013	Groundmass	IH	**424.2±1.8**[a]	1.45	422.6±5.6	1.59	296.2±6.2[e]	100 [550–1,300]	41.4
Benmoreite of Um Junb (unit oju, dome 1)									
R14TS069	Anorthoclase	LF	441.2±6.9[c,d]	2.06	441.7±10.9	2.1	293.5±7.5[e]		42.4
R14TS070	Anorthoclase	IH	435.3±5.6[c]	2.06	432.5±18.3	2.61	297.0±38.8[e]	54.7 [725–1,000]	60.2
Weighted mean age			**437.6±4.3**[a]						

Table 1. Summary of $^{40}Ar/^{39}Ar$ ages for volcanic rocks of the Matan volcanic center.—Continued

Sample	Phase analyzed	Method[b]	Plateau age		Isochron age			^{39}Ar, in % [T range, in °C]	$^{40}Ar^*$, in %
			Age ±1σ (ka)	MSWD	Age ±1σ (ka)	MSWD	$^{40}Ar/^{36}Ar_i$ ±2σ		
			Basalt of Sha'ib Si'ayd (unit bss)						
R16MS085	Groundmass	IH	**461.9±4.9**[a]	1.18	458.9±5.9	1.22	299.2±1.6[f]	94.5 [700–1,275]	23.7
			Benmoreite of As Sabah (unit osb)						
R15TS206	Groundmass	IH	620.3±8.0	7.67	**535.8±11.8**[a]	1.09	317.9±5.7[f]	76.75 [550–1,175]	32.8
			Benmoreite of Gura 3 (unit og3)						
R14AC003	Groundmass	IH	**558.7±4.8**[a]	1.67	565.4±66.8	1.98	293.3±45.7[e]	45.5 [600–950]	37.4
			Basalt of Al Bayadah (unit bba)						
R14TS084	Groundmass	IH	**674.7±7.2**[a]	0.94	668.4±22.8	1.05	295.9±3.5[e]	99.4 [550–1,275]	13.7
			Basalt of Dabaa 1 (unit bd1)						
R14AC018	Groundmass	IH	**717.7±12.2**[a]	0.64	724.3±20.3	0.68	295.3±1.2[e]	100 [550–1,250]	8.8
			Basalt of Gura 3 (unit bg3)						
R14DS001	Groundmass	IH	**1,112.1±17.6**[a]	1.01	1,118.8±49.2	1.17	295.0±6.2[e]	81.2 [550–1,175]	18.8

[a] Indicates a preferred age where only one age is available. Weighted mean ages are preferred, where available.

[b] Indicates the analytical technique used. IH, incremental heating; LF, laser total fusion.

[c] Indicates the age was used in the weighted mean preferred age for that sample.

[d] For sample R14TS069, analyzed by laser total fusion, the data in this column corresponds to the weighted mean age of the laser total fusion analyses.

[e] Indicates that the age was calculated assuming $^{40}Ar/^{36}Ar_{atmosphere}$ is 295.5±0.5 (Steiger and Jäger, 1977).

[f] Indicates that the age was calculated assuming $^{40}Ar/^{36}Ar_{atmosphere}$ is 298.56±0.31 (Lee and others, 2006).

Table 2. ^{36}Cl cosmogenic surface-exposure ages for the basalt of Musawda'ah (unit bms) of the Matan volcanic center.

[All ^{36}Cl cosmogenic surface-exposure ages were calculated using the CRONUScalc ^{36}Cl Exposure Age Calculator ver. 2.0 (Marrero and others, 2016) and the Lal and Stone time-independent scaling model (Lal, 1991; Stone, 2000). Bulk-rock Cl concentrations were measured by isotope Measurement dilution at Purdue Rare Isotope Measurement (PRIME) Laboratory at Purdue University. Sample R15MS004 was used as the bulk rock composition when calculating ^{36}Cl ages for sample R15TS189 (plagioclase separate). Chemical data reported for R15TS189 is the composition of the plagioclase separate and is used as the composition of the target mineral when calculating ^{36}Cl ages. Bulk density for sample R15MS004 was measured using Archimedes' principle. SF is the topographic shielding factor. mASL, meter above sea level; cm, centimeter; mm/k.y., millimeter per thousand years; g/cm^3, gram per cubic centimeter; ppm, part per million; g, gram; ka, kilo-annum]

Sample	Phase	Easting[a]	Northing[a]	Elevation (mASL)	Thickness (cm)	Erosion rate (mm/k.y.)	Bulk density (g/cm^3)	SF	Bulk Cl (ppm)	$^{36}Cl/Cl \times 10^{-15}$ ±1σ	^{36}Cl atoms/g $\times 10^5$ ±1σ	$^{35}Cl/^{37}Cl$ ±1σ	^{36}Cl age ±1σ (ka)
R15TS189	Plagioclase	578242	2677857	924	1	1±1	2.68[b]	1.0	0.6	525.2±20.9	3.55±0.14	31.45±0.71	56.5±6.7
R15MS004	Whole rock	580779	2680668	1,023	4	1±1	1.95	1.0	144.1	287.3±9.7	8.94±0.46	4.104±0.047	66.0±11.0

[a] Coordinates are in the World Geodetic System of 1984 Universal Transverse Mercator zone 37R (north) system.

[b] Bulk density for plagioclase sample R15TS189 was not measured, but assumed to be 2.68 g/cm^3 based on its major element composition. See appendix 1 for detailed methods on the ^{36}Cl cosmogenic surface-exposure dating method.

plagioclase has lower average anorthite contents than basalts. Mugearites are characterized by phenocryst assemblages of plagioclase, olivine, or plagioclase + olivine, in some samples accompanied by micropheocrysts of clinopyroxene, titanomagnetite, and sparse, blocky apatite. Olivine compositions range from Fo_{72} to Fo_{38}, and the majority of olivine has a composition between Fo_{55} and Fo_{43}. Plagioclase phenocrysts and groundmass crystals hosted in mugearite are dominantly andesine and labradorite, but some phenocrysts and groundmass crystals extend to oligoclase, anorthoclase, and sanidine. It is plausible that these more potassium-rich feldspar phenocrysts were inherited via interaction with a more evolved magma, but current observations cannot answer this question. Some mugearites contain traces of amphibole (<1 percent) identified via thin section petrography. The amphiboles are pleochroic from reddish brown to clear in plane light and are likely in the kaersutite series.

Benmoreites are typically characterized by a phenocryst assemblage of feldspar (oligoclase or anorthoclase) and olivine. Minor amounts of amphibole (kaersutite) phenocrysts are also found in some benmoreites. Minerals hosted in two benmoreites from the Matan volcanic center were analyzed in this study, the benmoreite of Um Junb (unit oju) that erupted at 437.6±4.3 ka and the benmoreite of Radio Tower (unit ort) that erupted before 150 ka based on stratigraphy (Downs and others, 2019), but has not been directly dated. We use an age of about 200 ka for unit ort in this study because of its similarity to benmoreites erupted around that time. Unit ort is characterized by phenocrysts of oligoclase and olivine that has $Fo_{44–36}$ (figs. 5 and 6). Unit oju is more chemically evolved than unit ort, and is characterized by phenocrysts of anorthoclase and olivine that has $Fo_{16–6}$ (figs. 5 and 6). Unit oju is unique among benmoreites in the Matan volcanic center in that it contains ~2 percent iron-rich augite phenocrysts (typically ≤0.5 mm), whereas pyroxene phenocrysts are not observed in other benmoreites. Trachytes in the Matan volcanic center are dominated by anorthoclase and sanidine phenocrysts (fig. 6) and have minor amounts of small, acicular pyroxene phenocrysts. Fayalitic (iron-rich) olivine has been reported as a phenocryst phase in other trachytes from Harrat Rahat, but is not observed as a phenocryst in trachytes from the Matan volcanic center. Pyroxene phenocrysts in Matan volcanic center trachytes range from hedenbergite to aegirine (fig. 7). Aegirine is only present in the youngest (17.6±1.9 ka) trachyte erupted within the Matan volcanic center, whereas most older trachytes contain hedenbergite to aegirine-augite.

Pyroxene is absent as a phenocryst in all Harrat Rahat rocks other than some trachytes. It is ubiquitous as an anhedral groundmass mineral, but it can be distinguished as microphenocrysts in mugearites and more evolved rock samples that have finely crystallized groundmasses. Pyroxene composition varies with whole-rock composition (fig. 7). Diopside is present as a groundmass phase in basalt, hawaiite, and mugearite (fig. 7*B*). Benmoreites contain groundmass hedenbergite and augite, and pyroxene becomes progressively more iron-rich as the whole-rock composition evolves (fig. 7*B*). For all compositions except trachyte, pyroxene crystals are sodium poor and contain ~20 weight percent CaO. Only in trachytes do the pyroxenes attain sodium-rich compositions (aegirine-augite or aegirine; fig. 7*A*). Fe-Ti-Cr-Al oxides of the spinel series are present in the groundmass, as inclusions in other mineral phases, and as sparse microphenocrysts in low-MgO basalts and more evolved rocks. They are composed almost entirely of titanomagnetite (fig. 8*A*). In general, titanomagnetite crystals in basalt, hawaiite, mugearite, and benmoreite have compositions closer to the ulvöspinel end-member composition, whereas titanomagnetite in trachyte plots close to the magnetite end member. Titanomagnetite from basalt, hawaiite, and mugearite display slightly elevated MgO and Al_2O_3 concentrations relative to titanomagnetite from benmoreite and trachyte (fig. 8). Titanomagnetite in mugearite and benmoreite eruptive products show bimodal compositions, and a subset of samples have compositions closer to the magnetite end member. Two oxides in a sample of the basalt of Ad Duwaykhilah (unit bdw) have significantly elevated concentrations of Al_2O_3, MgO, and Cr_2O_3 (fig. 8*B*–*G*). These oxides plot off the ulvöspinel-magnetite tie line and may be better classified as Cr-spinel (fig. 8*A*). These Cr-spinels are hosted in the groundmass of unit bdw, but more typically Cr-spinels in Harrat Rahat are hosted within olivine phenocrysts (Camp and others, 1987; Downs and others, 2018). The observation of Cr-spinel in Harrat Rahat lavas provides direct evidence for Cr-spinel crystallization early in the history of Harrat Rahat basalts. Sparse blades of ilmenite are present in the goundmass of basalts and hawaiites, but their compositions have not been investigated.

Table 3. Chemical composition of ^{36}Cl cosmogenic surface-exposure age samples.

[Major-oxide abundances, in weight percent, and trace-element abundances, in parts per million (ppm), measured for ^{36}Cl cosmogenic surface-exposure age samples. B and Li concentrations were below the detection limit for both samples. Given the detection limit for B and Li is 10 ppm, we assume the concentration of B and Li in each sample is 5±5 ppm. LOI, loss on ignition; plag, plagioclase; WR, whole rock]

Sample	Phase	SiO_2	TiO_2	Al_2O_3	Fe_2O_3	MnO	MgO	CaO	Na_2O	K_2O	P_2O_5	LOI	Cl	Sm	Gd	U	Th
R15TS189	Plag	53.0	0.10	29.6	0.43	<0.01	0.08	11.50	4.69	0.24	0.02	0.39	0.60	0.30	0.23	0.05	0.30
R15MS004	WR	46.5	3.56	17.9	13.90	0.20	4.83	8.17	3.96	0.84	0.49	0.29	144.10	3.60	3.80	0.33	1.00

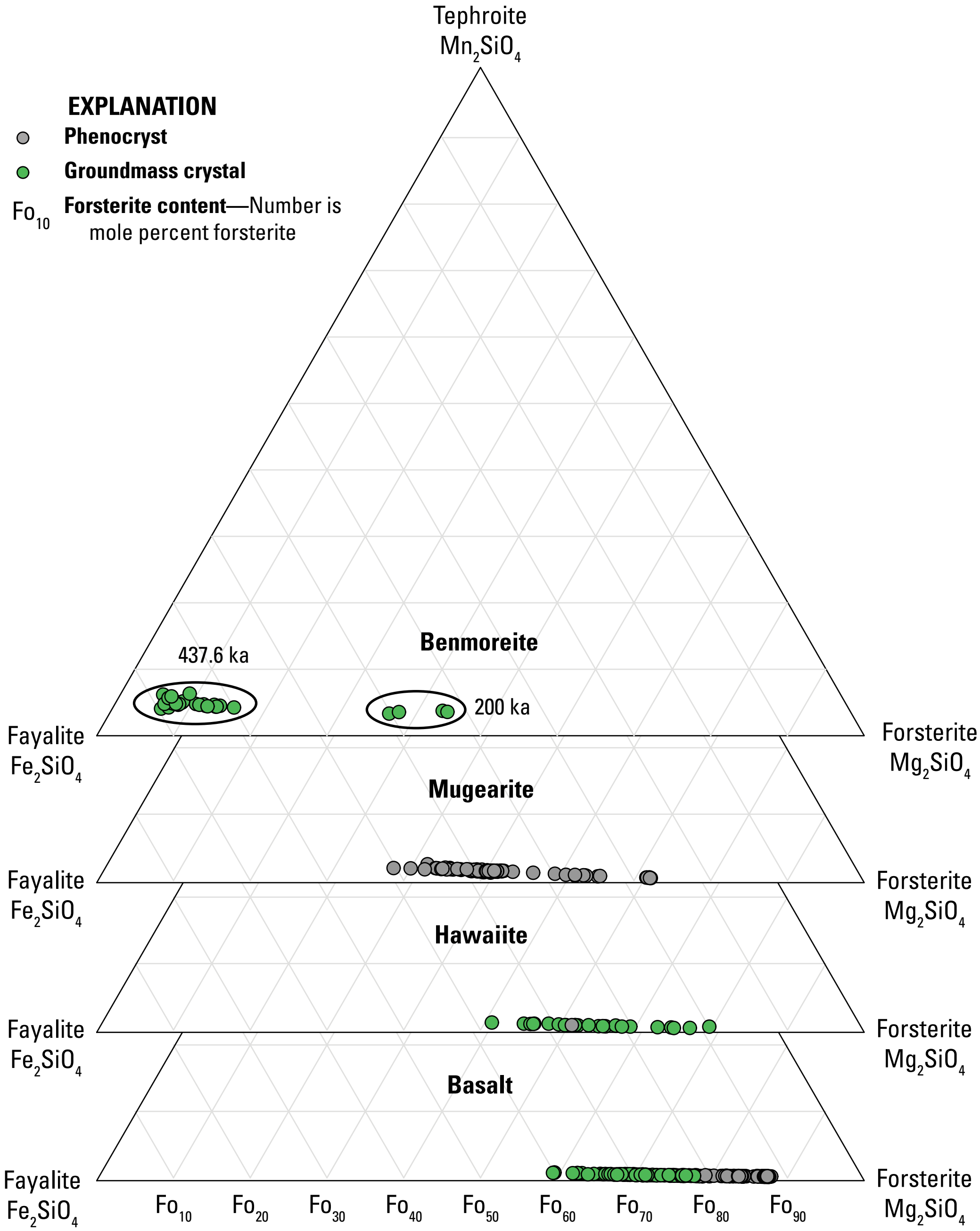

Figure 5. Ternary diagram of olivine compositions (in mol units) from eruptive products within or near the Matan volcanic center. Hawaiite, mugearite, and benmoreite analyses are from the Matan volcanic center. Hawaiite and mugearite analyses are from eruptive products that are <155 thousand years old (ka). Basalt analyses are from four basalts north of the Matan volcanic center that erupted after 155 ka, coeval with Matan volcanic center. Both benmoreite samples are older than 155 ka, including the benmoreite of Um Junb (unit oju) that erupted at 437.6±4.3 ka and the benmoreite of Radio Tower (unit ort) that erupted around 200 ka.

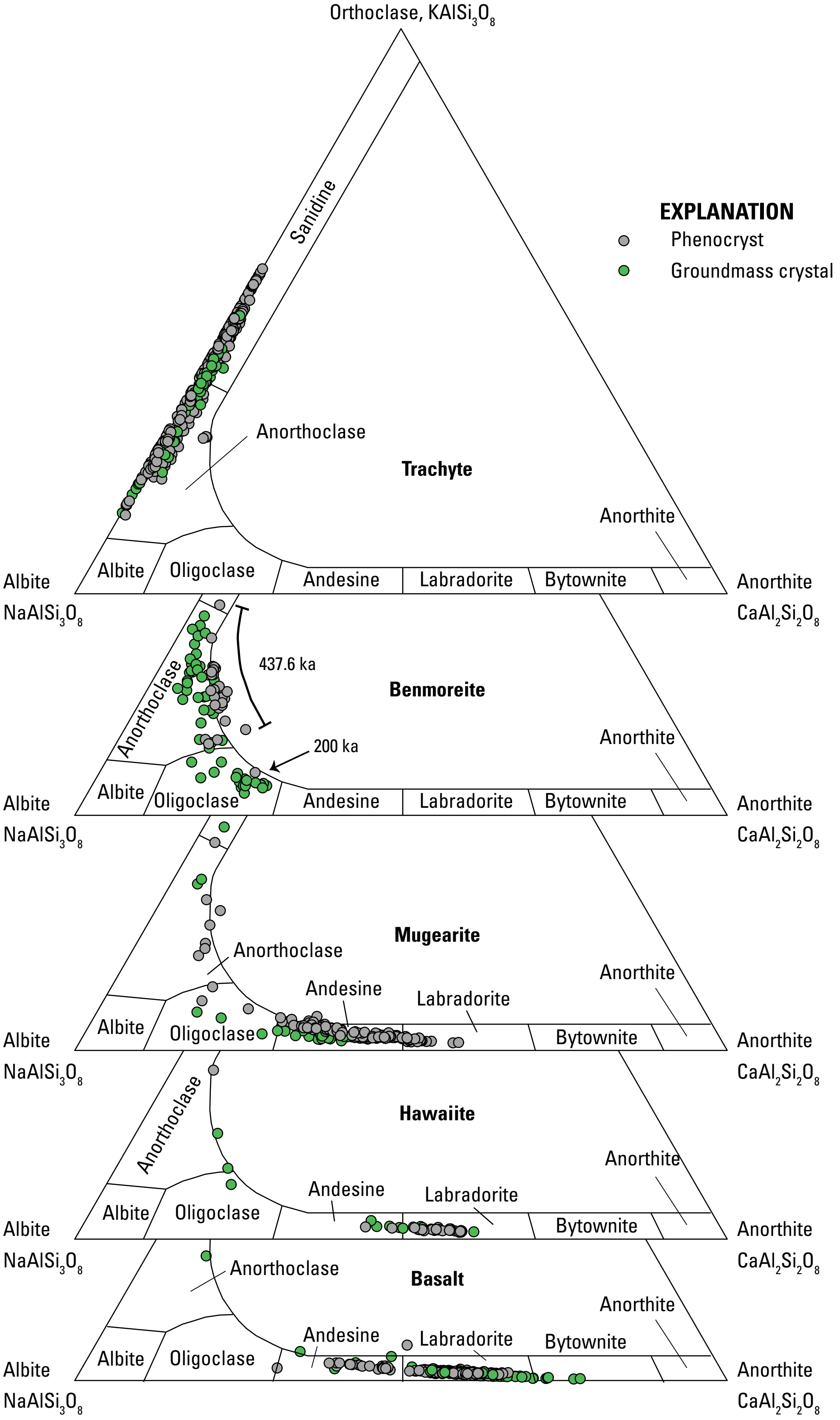

Figure 6. Ternary diagram of feldspar compositions (in mol units) from eruptive products within or near the Matan volcanic center. Hawaiite, mugearite, benmoreite, and trachyte analyses are from the Matan volcanic center. Hawaiite, mugearite, and trachyte analyses are from eruptive products that are <155 thousand years old (ka). Basalt analyses are from four basalts north of the Matan volcanic center that erupted after 155 ka, coeval with Matan volcanic center eruptive products. Both benmoreite samples are older than 155 ka, including the benmoreite of Um Junb (unit oju) that erupted at 437.6±4.3 ka and the benmoreite of Radio Tower (unit ort) that erupted around 200 ka.

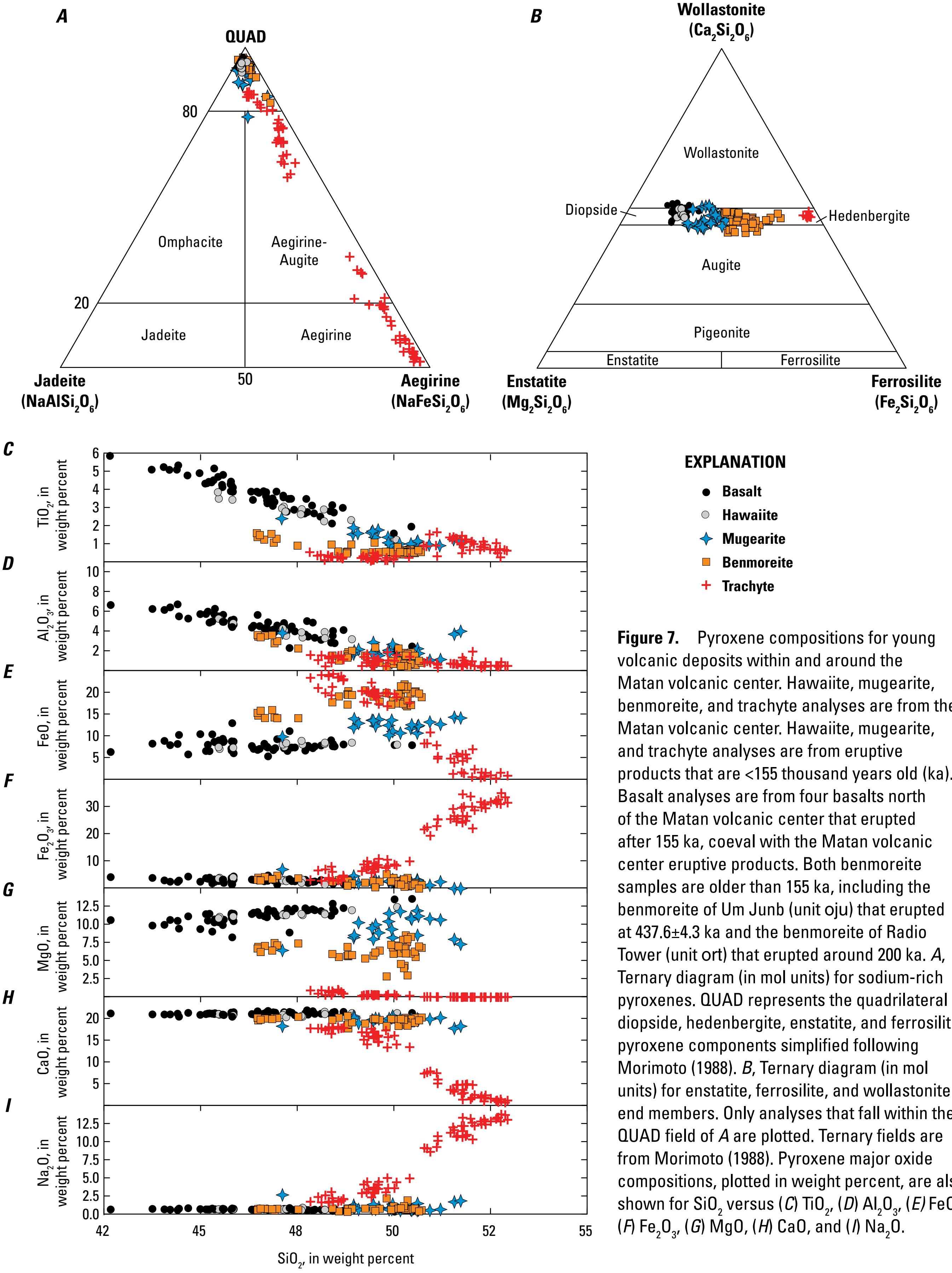

Figure 7. Pyroxene compositions for young volcanic deposits within and around the Matan volcanic center. Hawaiite, mugearite, benmoreite, and trachyte analyses are from the Matan volcanic center. Hawaiite, mugearite, and trachyte analyses are from eruptive products that are <155 thousand years old (ka). Basalt analyses are from four basalts north of the Matan volcanic center that erupted after 155 ka, coeval with the Matan volcanic center eruptive products. Both benmoreite samples are older than 155 ka, including the benmoreite of Um Junb (unit oju) that erupted at 437.6±4.3 ka and the benmoreite of Radio Tower (unit ort) that erupted around 200 ka. *A*, Ternary diagram (in mol units) for sodium-rich pyroxenes. QUAD represents the quadrilateral diopside, hedenbergite, enstatite, and ferrosilite pyroxene components simplified following Morimoto (1988). *B*, Ternary diagram (in mol units) for enstatite, ferrosilite, and wollastonite end members. Only analyses that fall within the QUAD field of *A* are plotted. Ternary fields are from Morimoto (1988). Pyroxene major oxide compositions, plotted in weight percent, are also shown for SiO$_2$ versus (*C*) TiO$_2$, (*D*) Al$_2$O$_3$, (*E*) FeO, (*F*) Fe$_2$O$_3$, (*G*) MgO, (*H*) CaO, and (*I*) Na$_2$O.

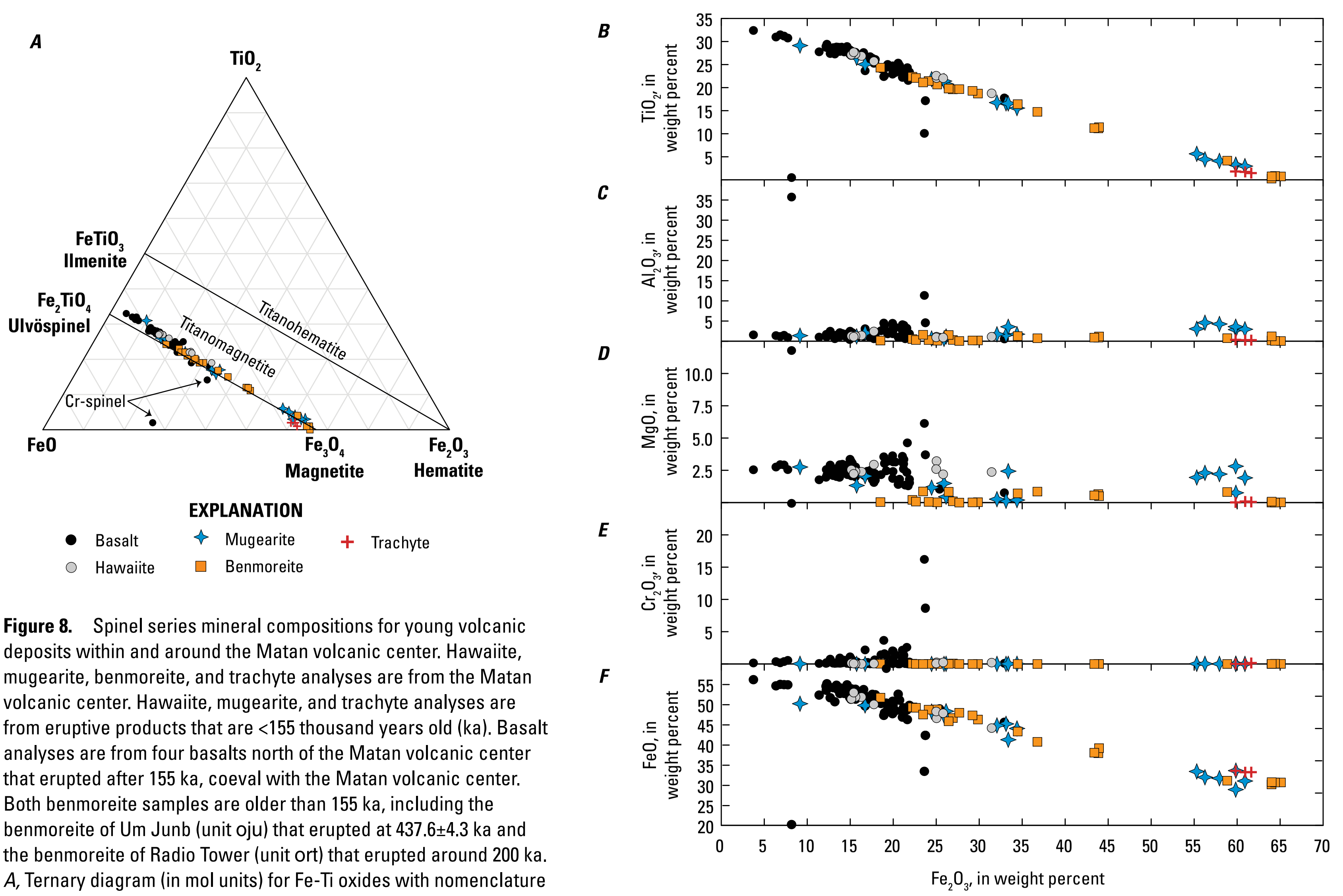

Figure 8. Spinel series mineral compositions for young volcanic deposits within and around the Matan volcanic center. Hawaiite, mugearite, benmoreite, and trachyte analyses are from the Matan volcanic center. Hawaiite, mugearite, and trachyte analyses are from eruptive products that are <155 thousand years old (ka). Basalt analyses are from four basalts north of the Matan volcanic center that erupted after 155 ka, coeval with the Matan volcanic center. Both benmoreite samples are older than 155 ka, including the benmoreite of Um Junb (unit oju) that erupted at 437.6±4.3 ka and the benmoreite of Radio Tower (unit ort) that erupted around 200 ka. *A,* Ternary diagram (in mol units) for Fe-Ti oxides with nomenclature from Rumble (1976) and Lindsley (1991). Major oxide concentrations, in weight percent, are also shown for oxide minerals for Fe$_2$O$_3$ versus (*B*) TiO$_2$, (*C*) Al$_2$O$_3$, (*D*) MgO, (*E*) Cr$_2$O$_3$, and (*F*) FeO.

Chemical Variations in Matan Volcanic Center Eruptive Products

Volcanic rocks of the Matan volcanic center define coherent chemical trends with decreasing MgO that provide additional information about the crystallizing assemblages in Harrat Rahat magmas (fig. 10). Interpretations based on bulk geochemical trends correspond well with the observed phenocryst assemblages of Harrat Rahat eruptive products in general, however, some important differences are apparent. Ni, Cr, Sc, and CaO/Al_2O_3 decrease with decreasing MgO whereas Sr increases with decreasing MgO in basalt and hawaiite magmas (fig. 10). This observation suggests that fractionation of olivine and pyroxene were dominant in mafic magmas, and fractionation of plagioclase occured in subordinate amounts. However, ratios of Sr to incompatible components (Sr/K, Sr/Nd) decline continuously with decreasing MgO, indicating that plagioclase fractionated in appreciable proportions across most or all of the differentiation series (Sisson and others, 2023). The decrease in Cr with decreasing MgO suggests Cr-rich oxide (that is, Cr-spinel) fractionated early in Harrat Rahat basalts. These geochemical inferences are consistent with the observation of olivine (some containing Cr-spinel inclusions) ± plagioclase phenocrysts, but inconsistent with the lack of pyroxene as a phenocryst phase in the basalts and hawaiites.

Sisson and others (2023) interpreted a three-stage history of differentiation producing northern Harrat Rahat hawaiites from basalts. The first stage was dominated by separation of olivine, giving way at between 9 and 10 weight percent MgO in the melt to growth and separation of a gabbroic assemblage. Gabbroic differentiaton is separable into an early stage lacking Ti-magnetite that drove melt SiO_2 to lower concentrations and a later stage including Ti-magnetite that increased melt SiO_2 concentrations, with the onset of Ti-magnetite growth at about 6 to 7 weight percent MgO in the melt, as marked by peaks in the concentrations of TiO_2, total Fe, and V. Rock compositions of the Matan volcanic center extend our understanding of differentiation to more evolved compositions with another change taking place near 4 weight percent MgO, which corresponds to the transition from hawaiite to mugearite. Beginning at ~4 weight percent MgO, Sr begins to behave compatibly, and Sr concentrations decrease with decreasing MgO (fig. 10). This observation is consistent with an increased proportion of plagioclase in the fractionating assemblage, perhaps accompanied by an increase is the partitioning of Sr into increasingly sodic plagioclase (Blundy and Wood, 1991). Similarly, P_2O_5 increases with decreasing MgO until ~4 weight percent MgO, at which point P_2O_5 begins to decrease because of apatite saturation in the melt; the onset of apatite saturation is marked in the mugearites by the appearance of sparse, blocky apatite microphenocrysts. At ~2 percent MgO, which corresponds to the transition from mugearite to benmoreite, Sr begins to deplete strongly in the melt, but otherwise the geochemical trends are similar to those of mugearites. The sharp depletion of Sr in the melt may reflect an increase in the proportion of feldspar crystallizing from the melt or a change in the bulk partition coefficient for Sr because of changing feldspar compositions (Blundy and Wood, 1991). CaO/Al_2O_3 and Sc concentrations continue to decrease with decreasing MgO in mugearite and benmoreite magmas, suggesting that clinopyroxene continued to fractionate. Though plagioclase and olivine are present as phenocryst phases in mugearite and benmoreite eruptive products, pyroxene phenocrysts are present soley as microphenocrysts and groundmass grains, consistent with observations in basalt and hawaiite eruptive products.

Only one benmoreite (unit oju) in northern Harrat Rahat is known to contain pyroxene phenocrysts. This benmoreite erupted at 437.6±4.3 ka within the Matan volcanic center and is characterized by a whole-rock composition that has elevated Ba and Sc concentrations relative to the main geochemical trend (fig. 10), which is consistent with accumulated feldspar and pyroxene crystals. In support of these geochemical inferences, petrographic examination of unit oju demonstrates that it contains large (as long as 6 mm) anorthoclase phenocrysts and ~2 percent euhedral to subhedral pyroxene phenocrysts (as long as 0.5 mm). Importantly, many of the pyroxene grains are found in plagioclase + olivine + pyroxene glomerocrysts. It is plausible that these anorthoclase phenocrysts, pyroxene phenocrysts, and plagioclase + olivine + pyroxene glomerocrysts represent crystals that would normally have remained as a cumulate phase within the crust, and in turn provide evidence for the concept of pyroxene-rich cumulates stored in the crust (for example, Ellis and others, 2014; Erdman and others, 2016).

Barium behaves incompatibly and increases in concentration with decreasing MgO until ~0.5 weight percent MgO, which marks the transition between benmoreite and trachyte (fig. 10). At ~0.5 weight percent MgO, Ba concentrations begin to decrease abruptly with decreasing MgO, marking the point at which anorthoclase and (or) sanidine begins to dominate the mineral assemblage. Scandium concentrations continue to decrease with decreasing MgO in trachytes, suggesting that pyroxene crystallization continued. These observations are consistent with the observed phenocrysts in Harrat Rahat trachyte eruptive products (anorthoclase and [or] sanidine + pyroxene).

Previous researchers interpreted that the chemical variations in Harrat Rahat eruptive products are largely due to fractional crystallization of their mafic progenitors with only minor crustal assimilation (Camp and Roobol, 1989; Moufti and others, 2012; Salters and others, 2023; Sisson and others, 2023). For example, Moufti and others (2012) suggested that constant Ba/Nb with decreasing MgO displayed by the Harrat Rahat eruptive suite indicates that crustal contamination is minimal, as fractional crystallization would not affect Ba/Nb, but crustal contamination would increase Ba/Nb in magmas because of the high Ba/Nb of crustal rocks in the region (for example, McGuire and Stern, 1993). A minimal role for crustal assimilation is also supported by the isotopic composition of Harrat Rahat eruptive products, which demonstrate that hawaiite, mugearite, benmoreite, and trachyte magmas have similar isotopic compositions to basaltic magmas (Moufti and others, 2012; Salters and others, 2023). This interpretation is consistent with geochemical studies at other harrats, which also suggest a limited role for crustal contamination (for example, Duncan and others, 2016).

Assuming that crystallization differentiation is the dominant control on major- and trace-element variations observed in Matan volcanic center eruptive products, there is a discrepancy between the apparent role of clinopyroxene crystallization in driving the observed geochemical trends and the lack of pyroxene as an observed phenocryst phase in mafic and intermediate magmas from Harrat Rahat. This discrepancy suggests that crystallization of Harrat Rahat magmas within the middle to lower crust and the formation of cumulates is an important step in magma genesis, as has been suggested at Harrat Rahat and other western Arabia Plate volcanic fields (for example, Shaw and others, 2003; Smith and others, 2008; McGee and others, 2012; Murcia and others, 2017; Downs and others, 2018; Sisson and others, 2023). In this scenario, the phenocryst assemblage observed in mafic and intermediate magmas likely reflects reequilibration at lower pressure (for example, Thompson, 1975), perhaps during magma ascent or storage within shallower parts of the crust.

Early Volcanism in the Matan Volcanic Center

New ^{40}Ar/^{39}Ar and ^{36}Cl ages demonstrate that volcanism in the area of the Matan volcanic center spanned from at least 1,112.1±17.6 to 17.6±1.9 ka. The older units (>155 ka) are mostly covered by younger units, so we focus on the younger eruptive history; a brief discussion of the eruptive history prior to ~155 ka is provided for geologic context. Volcanism before 155 ka was dominated by basaltic eruptions and minor amounts of hawaiite, mugearite, and benmoreite, but lacked trachyte. Insights into the early stages of volcanism can be gained by studying strata exposed in the floor and (or) walls of craters formed during explosive trachyte eruptions, or by studying older deposits uplifted during the emplacement of young trachyte domes. The oldest dated unit, the 1,112.1±17.6 ka basalt of Gura 3 (unit bg3), is a conical remnant of basalt exposed on the floor of the southernmost crater, which was apparently uplifted during eruption of the trachyte of Gura 3 (unit tg3) at 142.4±2.2 ka (fig. 9*B*). Exposed in the north wall of the crater is the 558.7±4.8 ka benmoreite of Gura 3 (unit og3), which is overlain by a basaltic lava flow chemically correlated with the 223.0±18.9 ka basalt of Ad Darah (unit bda), which in turn is overlain by trachyte deposits from unit tg3 and the trachyte of Gura 2 (unit tg2). The 717.7±12.2 ka basalt of Dabaa 1 (unit bd1) was exposed by uplift and tilting during emplacement of the 17.6±1.9 ka trachyte of Dabaa 1 (unit td1) and is exposed overlying unit td1 along the margins of the steep-sided dome (note that outcrops of unit bd1 are too small to display on fig. 9). A small outcrop of the 674.7±7.2 ka basalt of Al Bayadah (unit bba) is present in the west part of the Matan volcanic center. Considered together, these data suggest that volcanism proximal to the Matan volcanic center before 600 ka was dominated by basaltic eruptions.

The time interval between ~560 and 420 ka was characterized by eruption of benmoreites: unit og3 at 558.7±4.8 ka, the benmoreite of As Sabah (unit osb) at 535.8±11.8 ka, the first phase of unit oju at 437.6±4.3 ka, and the second phase of unit oju at 424.2±1.8 ka. These benmoreites appear to have been emplaced when basalts were not erupting in the Matan volcanic center. After eruption of benmoreite, there was an apparent lull in volcanism in the Matan volcanic center from ~420 to 250 ka, after which volcanism resumed with eruption of the basalt of Amlit 1 (unit bam1) at 252.2±6.8 ka. Volcanism continued from ~250 to 200 ka, dominantly producing basalt, hawaiite, and mugearite, as well as benmoreite at 242.8±2.4 ka (fig. 9; benmoreite of Al Bayadah [unit oba]) and ~200 ka (fig. 9; benmoreite of Radio Tower [unit ort]). No volcanism is known in the Matan volcanic center from ~200 to 155 ka, after which volcanism returned in the form of basalt, mugearite, benmoreite, and trachyte eruptions.

Figure 9 (page 19). Geologic map of the Matan volcanic center and eruption sequence for volcanic deposits that are ≤155 thousand years old (ka). Age uncertainties are reported at the 1σ level. Unit symbols and ages for units that are older than 200 ka (that is, erupted prior to the formation of the Matan volcanic center) are shown in black; those of units that are part of the Matan volcanic center (that is, younger than 155 ka) are shown in white. All unit names and symbols are modified from Downs and others (2019) and Robinson and Downs (2023). *A*, Geologic map of the Matan volcanic center. Location within northern Harrat Rahat is shown in figure 4. *B*, Close-up view of the crater formed during eruption of the trachyte of Gura 3 (unit tg3), showing the ages of units exposed in the crater floor and north crater wall. *C*, Eruption sequence for the Matan volcanic center. ^{40}Ar/^{39}Ar eruption ages and minimum erupted volumes are provided. Note that outcrops of the basalt of Dabaa 1 (unit bd1; 717.7±12.2 ka), which are exposed along the margins of the trachyte of Dabaa 1 (unit td1), are too small to resolve at the scale of this map, but the sample locations are reported in appendix 2. Sequences 1 through 4 are interpreted to represent the injection of mantle-derived basalts into the crust, and subsequent differentiation and eruption of those magmas. An asterisk next to a unit symbol indicates that electron microprobe data are available for that unit. km^3, cubic kilometer.

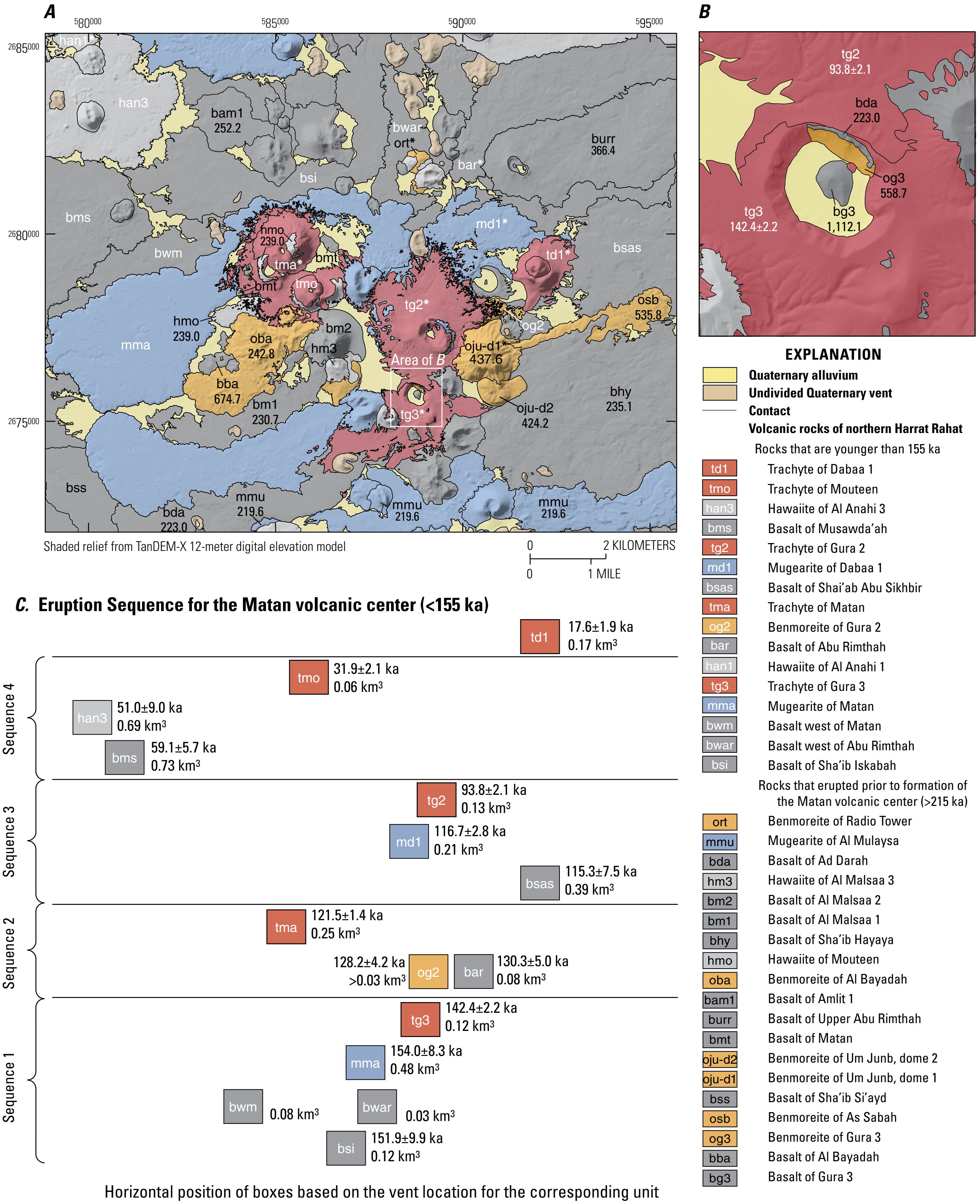
A
580000
585000
590000
595000
2685000
2680000
2675000
han1
han3
bam1
252.2
bwar
ort*
bar*
burr
366.4
bsi
bms
bwm
hmo
239.0
tma*
bmt
bmt
tmo
md1*
td1*
bsas
tg2*
og2
osb
535.8
hmo
239.0
mma
oba
242.8
bm2
hm3
oju-d1*
437.6
Area of B
bba
674.7
bm1
230.7
tg3*
oju-d2
424.2
bhy
235.1
bss
mmu
219.6
bda
223.0
mmu
219.6
mmu
219.6
Shaded relief from TanDEM-X 12-meter digital elevation model
0
2 KILOMETERS
0
1 MILE
B
tg2
93.8±2.1
bda
223.0
og3
558.7
tg3
142.4±2.2
bg3
1,112.1
EXPLANATION
Quaternary alluvium
Undivided Quaternary vent
Contact
Volcanic rocks of northern Harrat Rahat
Rocks that are younger than 155 ka
td1 Trachyte of Dabaa 1
tmo Trachyte of Mouteen
han3 Hawaiite of Al Anahi 3
bms Basalt of Musawda'ah
tg2 Trachyte of Gura 2
md1 Mugearite of Dabaa 1
bsas Basalt of Shai'ab Abu Sikhbir
tma Trachyte of Matan
og2 Benmoreite of Gura 2
bar Basalt of Abu Rimthah
han1 Hawaiite of Al Anahi 1
tg3 Trachyte of Gura 3
mma Mugearite of Matan
bwm Basalt west of Matan
bwar Basalt west of Abu Rimthah
bsi Basalt of Sha'ib Iskabah
Rocks that erupted prior to formation of the Matan volcanic center (>215 ka)
ort Benmoreite of Radio Tower
mmu Mugearite of Al Mulaysa
bda Basalt of Ad Darah
hm3 Hawaiite of Al Malsaa 3
bm2 Basalt of Al Malsaa 2
bm1 Basalt of Al Malsaa 1
bhy Basalt of Sha'ib Hayaya
hmo Hawaiite of Mouteen
oba Benmoreite of Al Bayadah
bam1 Basalt of Amlit 1
burr Basalt of Upper Abu Rimthah
bmt Basalt of Matan
oju-d2 Benmoreite of Um Junb, dome 2
oju-d1 Benmoreite of Um Junb, dome 1
bss Basalt of Sha'ib Si'ayd
osb Benmoreite of As Sabah
og3 Benmoreite of Gura 3
bba Basalt of Al Bayadah
bg3 Basalt of Gura 3
C. Eruption Sequence for the Matan volcanic center (<155 ka)
td1 17.6±1.9 ka 0.17 km³
Sequence 4
tmo 31.9±2.1 ka 0.06 km³
han3 51.0±9.0 ka 0.69 km³
bms 59.1±5.7 ka 0.73 km³
Sequence 3
tg2 93.8±2.1 ka 0.13 km³
md1 116.7±2.8 ka 0.21 km³
bsas 115.3±7.5 ka 0.39 km³
Sequence 2
tma 121.5±1.4 ka 0.25 km³
128.2±4.2 ka >0.03 km³ og2
bar 130.3±5.0 ka 0.08 km³
Sequence 1
tg3 142.4±2.2 ka 0.12 km³
mma 154.0±8.3 ka 0.48 km³
bwm 0.08 km³
bwar 0.03 km³
bsi 151.9±9.9 ka 0.12 km³
Horizontal position of boxes based on the vent location for the corresponding unit

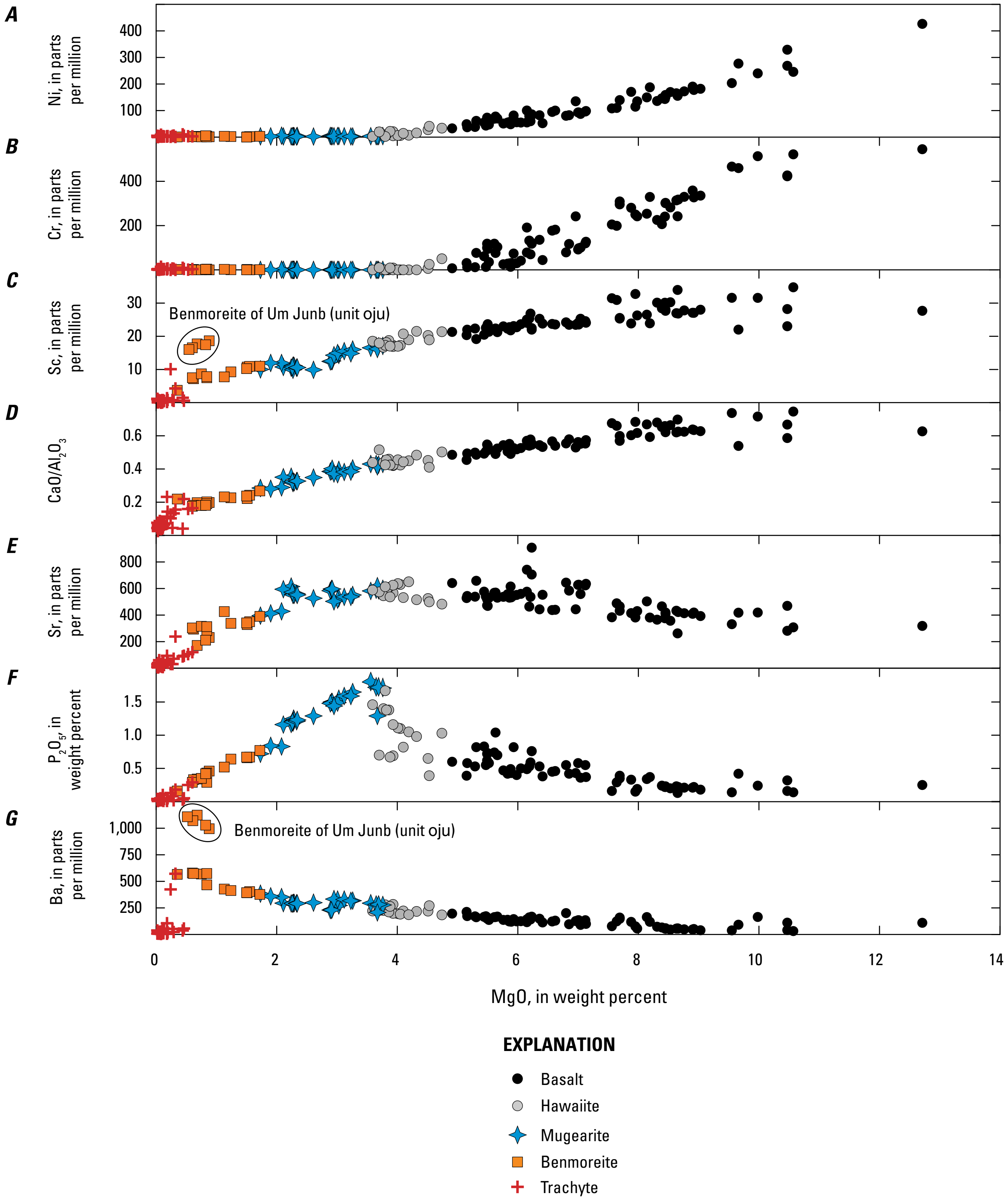

Figure 10. Chemical trends of eruptive products from the Matan volcanic center. Concentration of MgO is used as a proxy for differentiation, where decreasing MgO corresponds to increasing differentiation. Plots show MgO versus (*A*) Ni, (*B*) Cr, (*C*) Sc, (*D*) CaO/Al$_2$O$_3$, (*E*) Sr, (*F*) P$_2$O$_5$, and (*G*) Ba. Samples from the benmoreite of Um Junb (unit oju) are circled in *C* and *G* to show their high Ba and Sc concentrations caused by the presence of accumulated feldspar and pyroxene phenocrysts, verified by thin section analysis.

Post-155 ka Volcanism in the Matan Volcanic Center

Here we focus on the ages and field relations of eruptive products from the Matan volcanic center that are ≤155 ka (summarized in fig. 9). In general, volcanism after 155 ka was characterized by four eruption sequences of alkali basalt followed by hawaiite, mugearite, or benmoreite, which in turn is followed by trachyte.

After an eruptive hiatus from ~200 to 155 ka, volcanism resumed with eruption of three basaltic units (basalt of Sha'ib Iskabah [unit bsi], overlain by the basalt west of Abu Rimthah [unit bwar], and by the basalt west of Matan [unit bwm]). The ages of these basaltic eruptions are all bracketed by a date of 151.9±9.9 ka on unit bsi and 154.0±8.3 ka on the overlying mugearite of Matan (unit mma). Therefore, the undated units bwm and bwar, which overlie unit bsi and underlie unit mma, are assigned an age of ~152 ka (fig. 9). Unit mma is a flat-topped lava flow that traveled mainly to the west-southwest from a well-preserved vent in the center of the Matan volcanic center. The surface of unit mma is decorated with hornitos, as is common of mugearite lava flows in Harrat Rahat. The trachyte of Gura 3 (unit tg3) erupted explosively at 142.4±2.2 ka, producing pyroclastic-flow and -surge deposits that extend >3 km away from its source, and excavating a >500-meter (m)-diameter by >50-m-deep steep-sided crater. No air-fall-tephra deposits have been identified for unit tg3, possibly because of erosion.

Subsequent to the 142.4±2.2 ka unit tg3 eruption, the basalt of Abu Rimthah (unit bar) erupted at 130.3±5.0 ka and the benmoreite of Gura 2 (unit og2) erupted at 128.2±4.2 ka. Lavas from unit og2 are exposed to the north of unit oju, underlying pyroclastic-flow deposits from unit tg2. The vent for unit og2 is obscured by young trachyte pyroclastic flows but is inferred to be buried or partly destroyed by the >500-m-diameter, >80-m-deep crater generated during eruption of unit tg2 at 93.8±2.1 ka (fig. 9). No direct stratigraphic relations exist between units bar and og2, but the new ^{40}Ar/^{39}Ar eruption ages suggest that unit og2 erupted after, or is contemporaneous with, unit bar. The next Matan volcanic center eruption produced the trachyte of Matan (unit tma) at 121.5±1.4 ka, which created a ~320-m-high, steep-sided dome. Juvenile trachyte lava is exposed around the margin of a small crater (~100–150 m in diameter) along the southwest part of the dome, whereas the rest of the dome consists of the uplifted 239.0±4.1 ka hawaiite of Mouteen (unit hmo), the ~154 ka unit mma, and the undated basalt of Matan (unit bmt). These uplifted lavas are mantled by block-and-ash flows and other pyroclastic-flow deposits that were generated during an early explosive phase of unit tma emplacement, and by subsequent small Peléan dome-collapse deposits.

Following eruption of unit tma, the basalt of Shai'ab Abu Sikhbir (unit bsas) erupted at 115.3±7.5 ka from a vent that is inferred to have been destroyed during emplacement of the 17.6±1.9 ka unit td1 dome. Lavas from unit bsas flowed to the east and consist of two lobes that reach ~12 and ~18 km from the vent. Eruption of the mugearite of Dabaa 1 (unit md1) followed shortly thereafter at 116.7±2.8 ka, but within uncertainty of the age for unit bsas. The vent for unit md1 is present as a partly exposed high-standing area to the northwest of the crater that formed during the 93.8±2.1 ka eruption of unit tg2 (fig. 9). The geomorphic expression of unit tg2 indicates that a trachyte dome formed during the early stages of the eruption, and subsequent explosive activity destroyed much of the dome while producing at least two nested craters. These explosive eruptions produced pyroclastic-flow and -surge deposits that extend >2 km from the crater.

After an apparent eruptive hiatus of >30 thousand years (k.y.), volcanism resumed with eruption of units bms and han3 at 59.1±5.7 and 51.0±9.0 ka, respectively (Downs and others, 2018). Both units originated from vents located to the northwest of the main vent axis associated with Matan volcanic center volcanism (fig. 9). Unit bms flowed ~24 km to the west and unit han3 flowed ~19 km to the northwest. These eruptions were followed by eruption of the trachyte of Mouteen (unit tmo) at 31.9±2.1 ka, ultimately producing a ~220-m-high, steep-sided dome. The overall eruptive style and products of unit tmo are almost identical to those that produced unit tma just to the north. The most recent Matan volcanic center eruption created unit td1 at 17.6±1.9 ka, which consists of a small-volume, vent-proximal air-fall-tephra deposit, and a ~200-m-high, steep-sided dome mantled and surrounded by pyroclastic material shed off the dome during uplift (fig. 9). Dense juvenile trachyte lava is exposed in the center of the dome, whereas the margins contain a mix of juvenile trachyte clasts within the pyroclastic material, as well as uplifted lavas from the 717.7±12.2 ka unit bd1 and 116.7±2.8 ka unit md1 (note that the outcrops of unit bd1 are too small to display on fig. 9).

Timescales of Magmatic Differentiation from Alkali Basalt to Trachyte

The eruptive quiescence between ~200 and 155 ka in the Matan volcanic center suggests that the flux of basalt into the crust waned during this time. In turn, resumption of volcanism in this area at ~155 ka can be interpreted as marking an increased influx of basaltic magma into the crust. ^{40}Ar/^{39}Ar dates and field relations for volcanic strata within the Matan volcanic center demonstrate that between ~155 and 17 ka, the following eruptive sequence occurred four times: (1) alkali basalt (45.5–47.7 weight percent SiO_2), (2) hawaiite, mugearite, or benmoreite (47.8–56.1 weight percent SiO_2), and (3) trachyte (62.6–63.6 weight percent SiO_2) (figs. 9 and 11). In each of these sequences, the eruption of basalt and intermediate magma (hawaiite, mugearite, or benmoreite) were closely spaced in time (within 3 k.y.), but eruption of trachyte occurred ~7–23 k.y. after eruption of the intermediate magma.

Because of their striking temporal and compositional similarities, we interpret each of these eruptive sequences to reflect the injection of mantle-derived basalts into the crust and subsequent differentiation and eruption of those derivative magmas. In turn, we assume that there is a genetic relation between eruptive products from a given eruptive sequence. It is not required that the erupted basalt (that is, within an eruption sequence) represents the parent magma from which the more evolved eruptive products were directly derived. Rather, it is only assumed that the erupted basalt is related to the same episode of basaltic injection into the crust.

If instead, the more evolved eruptive products were derived from a longer lived magma reservoir that was not related to the erupted basalts, then the timescales presented here would not necessarily represent differentiation timescales. We consider this scenario unlikely for the three reasons.

1. Trachyte eruptives are rare in northern Harrat Rahat prior to ~155 ka, and intermediate composition magmas (that is, mugearite and benmoreite) had only erupted sporadically prior to ~155 ka. These observations suggest that Harrat Rahat lacks an integrated, long-lived crustal magma reservoir capable of producing evolved magmas, but instead only produces evolved magmas in discrete pulses.

2. Isotopic data from Moufti and others (2012) and Salters and others (2023) demonstrate that evolved magmas have radiogenic isotopic compositions that differ only slightly from the alkali basalts, which is consistent with the evolved magmas being derived from parental alkali basalt ($^{87}Sr/^{86}Sr$ increases markedly among trachytes with low Sr concentrations).

3. Recent magnetotelluric data for northern Harrat Rahat find no evidence of magma stored in the crust (Bedrosian and others, 2019; Peacock and others, 2023).

The small volumes of the erupted trachytes (individually 0.06–0.25 km^3) also suggest that they were not derived from a large, integrated magmatic system. Treating Rb as perfectly incompatible during crystallization or melting, and assuming that the erupted magmas represent liquids derived from a parental basaltic source with 2.4 parts per million (ppm) Rb (median Rb concentration for northern Harrat Rahat alkali basalts with Mg#[4] >0.64 [Sisson and others, 2023]), the trachyte eruptive products would represent ~97 weight percent fractionation (or 3 weight percent partial melt) of the parental basalt. If instead the parental basalt was more fractionated (6.8 ppm Rb; average for Matan volcanic center basalts), then trachytes would represent ~92 weight percent fractionation (or 8 weight percent melting) of the parental basalt. Thus, to generate ~0.25 km^3 of trachyte would require the fractionation of ~8 km^3 of primitive basalt, or ~3 km^3 of average basalt. These source volumes, though only approximate, do not require a large magma reservoir on the scale of those that feed many rhyolitic eruptions in other tectonic settings. If the erupted trachytes were formed as enriched boundary layers caused by sidewall crystallization of a basaltic magma chamber, then it is plausible that the basaltic intrusion(s) from which they were sourced had a larger volume than calculated above. However, given the lack of evidence for a well-developed, large-volume crustal magma reservoir, we consider this scenario unlikely (Bedrosian and others, 2019; Peacock and others, 2023).

Assuming that each eruptive sequence reflects the injection of mantle-derived basalts into the crust and subsequent differentiation and eruption of those magmas, then the difference in age between subsequent eruptions (that is, interval time) reflects the duration of magmatic differentiation (fig. 11). Uncertainties on the interval times (and therefore differentiation timescales) are calculated as 95-percent confidence intervals using Welch's t-interval method (Welch, 1947; Pitcher and others, 2017). For example, if the age of unit bar (130.3±5.0 ka) represents the timing of basaltic influx into the crust at the start of sequence 2, then the eruption of unit og2 at 128.2±4.2 ka implies a duration of $2.1^{+4.8}_{-2.1}$ k.y. for crystallization from basalt to benmoreite, where the asymmetric uncertainties reflect the fact that differentiation timescales cannot be less than zero. It is not possible, based on our results, to estimate how long each basaltic magma resided in the crust before being erupted. In turn, the differentiation timescale estimates from basalt to intermediate compositions (that is, hawaiite, mugearite, and benmoreite) may be underestimated if, for example, a long-lived basaltic intrusive complex exists in the lower crust where elevated temperatures could lead to longer differentiation timescales. However, the near-contemporaneous eruption of basalt and intermediate magma are consistent with the interpretation that eruptions of basalt signaled the transport of deeply sourced magmas to shallower levels of the crust, some of which erupted and some of which further differentiated. Differentiation timescales from intermediate compositions to trachyte are insensitive to these considerations because they are not based on the age of the basaltic magmas. Instead, differentiation timescales from intermediate compositions to trachyte are maxima because it is possible that differentiation occurred quickly (relative to the calculated timescales), followed by residence of the differentiated magma in the crust before eruption.

Following the reasoning described above, differentiation timescales can be calculated for each of the eruptive sequences observed in the Matan volcanic center (fig. 11). Interval times for the four basalt-to-trachyte eruptive sequences in the Matan volcanic center suggest that differentiation from basalt to intermediate compositions took $0.0^{+4.1}_{-0.0}$ to $2.1^{+4.8}_{-2.1}$ k.y. Differentiation from intermediate compositions to trachyte took a maximum of 6.7±3.6 to 22.9±1.7 k.y. Thus, the total time of differentiation from alkali basalt to trachyte was ~10–25 k.y. Isotopic data presented by Moufti and others (2012) and Salters and others (2023) suggest that evolved magmas at Harrat Rahat are likely derived from alkali basalt with minor assimilation of country rock (<5 weight percent assimilation based on high-precision Pb isotopes [Salters and others, 2023]). We consider it most likely that the evolved magmas formed via crystallization differentiation of an alkali basalt parent magma. However, it is also possible that the evolved

---

[4] Mg# = Mg/(Mg+Fe), molar.

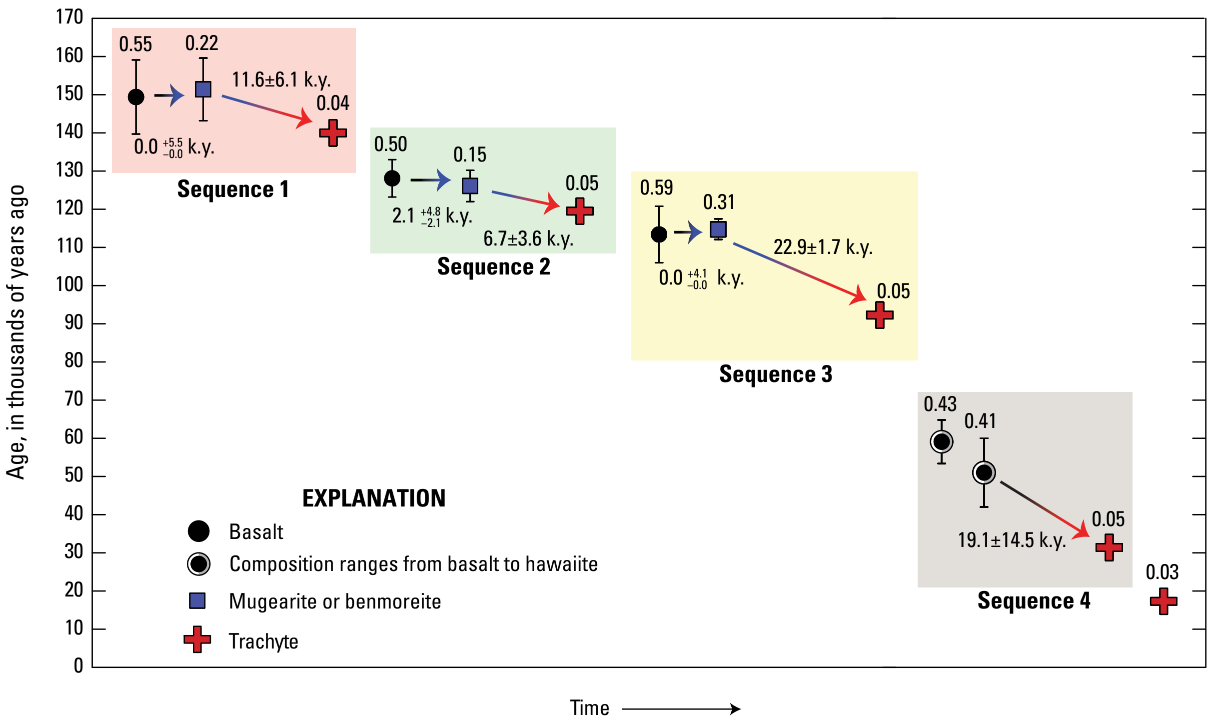

Figure 11. Diagram summarizing the eruption history of the Matan volcanic center. Four eruptive sequences are observed, each characterized by (1) eruption of basalt, (2) eruption of hawaiite, mugearite, or benmoreite, and (3) eruption of trachyte. These sequences are interpreted to reflect the injection of mantle-derived basalts into the crust and subsequent differentiation and eruption of those magmas. Different eruptive sequences are highlighted by different background colors. On the x-axis, samples are plotted in order of eruption age and arrow lengths between successive eruptions are scaled to the associated differentiation timescales. Decimals above eruption symbols give the estimated melt fraction from rubidium (Rb) concentrations, F_{Rb}, which is calculated by treating Rb as perfectly incompatible during crystallization or melting, and assuming that the erupted magmas represent liquids derived from a parental alkali basalt with 3.8 parts per million Rb. Age uncertainties are 1σ. Uncertainties on the differentiation timescales, in thousand years (k.y.), are calculated as 95-percent confidence intervals using Welch's t-interval method (Welch, 1947; Pitcher and others, 2017). Interval times (and their negative uncertainties) have been adjusted such that the interval time is not less than zero.

magmas formed by partial remelting of mafic intrusive bodies (chemically similar to the erupted alkali basalts) that stalled in the crust during earlier episodes of magmatism at Harrat Rahat. Regardless, the differentiation timescales provided here are independent of the process(es) invoked to drive magmatic differentiation because they are based solely on the measured eruption ages of volcanic products.

Broader Implications

The durations of differentiation from alkali basalt to trachyte presented here are novel in that they are based solely on the age and composition of eruptive products from a system in which field relations demonstrate a simple, repeated differentiation sequence. In most other cases, the duration of magmatic differentiation from basalt to trachyte or rhyolite have been estimated from time-correlative trends in the whole-rock ^{238}U-^{230}Th-^{226}Ra isotopic composition of lavas interpreted to be consanguineous (for example, Hawkesworth and others, 2000). However, this method can be limited in determining differentiation timescales because of complex field relations that make it difficult to assess how evolved magmas are temporally related to the input of primitive basaltic magmas in the crust. In turn, assumptions must be made regarding the initial isotopic composition of the parental mafic magma that may skew the resulting differentiation timescales.

Although comparisons are sparse, the differentiation timescales of ~10–25 k.y. to produce trachyte from alkali basalt within the Matan volcanic center are shorter than differentiation timescales derived from uranium-series studies from other volcanic systems. For example, Lowenstern and others (2006) used ^{238}U-^{230}Th isotope data to suggest that extraction of basalt from its mantle source region, subsequent crystallization and melt extraction to form silicic magmas, and final crystallization of a shallow silicic intrusion took ~30–50 k.y. at the Alid volcanic center in Eritrea. Widom and others (1992) suggested, on the basis of ^{238}U-^{230}Th isotope data, that evolution of alkali basalt to trachyte on São Miguel in the Azores took ~90 k.y. Likewise, Thomas (1999) suggested that differentiation from basanite to phonolite at Tenerife on the Canary Islands took ~200 k.y. based on ^{238}U-^{230}Th isotopic data.

It is interesting to note that durations of differentiation inferred from eruption ages do not scale proportionally with the estimated mass fractions of differentiation. Differentiation timescales from basalt to intermediate compositions (hawaiite, mugearite, or benmoreite) at Harrat Rahat (≤3.0 k.y.) are significantly shorter than differentiation from intermediate compositions to trachyte (~7–23 k.y.), despite representing a mass fraction of differentiation that is as much as three times larger (fig. 11). The short durations of differentiation from alkali basalt to intermediate compositions are consistent with ^{238}U-^{230}Th-^{226}Ra data presented by Condomines and others (1995) for lavas erupted from Etna, which suggest that differentiation from parental hawaiite to mugearite occurred in ≤200 years. The different rates of differentiation recorded for the different stages of magmatic evolution at Harrat Rahat could be explained by several different processes.

- The short durations of differentiation from basalt to intermediate compositions could reflect differentiation via crystal settling in a liquid-dominated system (>60 percent melt). In contrast, to produce a trachyte magma body requires further crystallization followed by extraction of the evolved melt from a crystal-rich magma body (<40 percent melt) via hindered settling or compaction, which are slow processes relative to crystal settling (for example, Bachmann and Bergantz, 2004).
- As differentiation proceeds, the declining temperature contrast between the magmatic intrusive source and its local environment may result in slowing rates of crystallization.
- The formation of trachyte magma bodies may also have occurred quickly (≤3 k.y.), but the trachytic magmas experienced extended residence in the crust prior to eruption.

Future work could integrate our newly constrained differentiation timescales with thermal modeling to constrain cooling rates at different ambient crustal temperatures, and with geochemical modeling of major- and trace-element variations displayed by each eruptive sequence. In this manner, it may be possible to discern whether magmatic differentiation at Harrat Rahat takes place in the upper or lower crust, and therefore better understand controls on the durations of magmatic differentiation. Furthermore, quantifying the crystallization age of minerals hosted within the trachytes at Harrat Rahat via ^{238}U-^{230}Th dating, and comparing these ages to our new ^{40}Ar/^{39}Ar eruption ages may provide a means to further refine our differentiation timescales by quantifying the residence time of trachytic magmas in the crust.

Conclusions

Integrating field relations from geologic mapping with new ^{40}Ar/^{39}Ar ages, ^{36}Cl surface-exposure ages, and geochemical data provides new constraints on the eruptive history of the Matan volcanic center and the larger northern Harrat Rahat region and puts limits on the differentiation timescales required to produce trachyte from parental alkali basalt. Key observations and conclusions are as follows.

1. Trachytic magmas within the Matan volcanic center have dominantly erupted after 155 ka and have small individual volumes (0.06–0.25 km^3), suggesting that the trachytes were not sourced from a large, integrated, and (or) long-lived silicic magmatic system.
2. From ~155–17 ka, the following eruptive sequence occurred four times: (1) alkali basalt (45.5–47.7 weight percent SiO_2), (2) hawaiite, mugearite, or benmoreite (47.8–56.1 weight percent SiO_2), and (3) trachyte (62.6–63.6 weight percent SiO_2).
3. We interpret each of these basalt-to-trachyte eruptive sequences to reflect the injection of mantle-derived basalts into the crust and subsequent differentiation and eruption of those magmas. Magmatic evolution within the Matan volcanic center was most likely driven by crystallization differentiation. We use the interval time between successive eruptions within a given eruption sequence to calculate the duration of magmatic differentiation required to produce trachyte from parental alkali basalt. Interval times for the four pulses of magmatism suggest that differentiation from basalt to intermediate compositions (hawaiite, mugearite, or benmoreite) takes $0.0^{+4.1}_{-0.0}$ to $2.1^{+4.8}_{-2.1}$ k.y. Differentiation from intermediate compositions to trachyte takes a maximum of 6.7±3.6 to 22.9±1.7 k.y. (uncertainties reported at the 95-percent confidence level). Thus, the duration of differentiation from alkali basalt to trachyte is ~10–25 k.y.
4. The durations of differentiation inferred from eruption ages do not scale proportionally with the estimated mass fractions of differentiation. The duration of differentiation (≤3 k.y.) from basalt to intermediate compositions (hawaiite, mugearite, or benmoreite) is significantly shorter than differentiation from intermediate compositions to trachyte (~7–23 k.y.), despite representing a larger mass fraction of differentiation.
5. Differentiation timescales presented here are novel because they are based solely on ages and compositions of eruptive products from a system in which field relations demonstrate a simple, repeated differentiation sequence. As such, these timescales are insensitive to the process invoked to drive magmatic differentiation.

Acknowledgments

This work was supported by funding from the Saudi Geological Survey and the U.S. Geological Survey. Field and logistical support were provided by the Saudi Geological Survey under the leadership of Dr. Zohair A. Nawab, President (retired). We are grateful to Katie Sullivan, Brandon Swanson, Dean Miller, and James Saburomaru for their invaluable assistance in preparing and analyzing samples for this study, to Jessica Ball, Seth Burgess, and Michael Clynne for their constructive comments and suggestions that helped strengthen this manuscript, and to Monica Erdman for her skilled edit.

References Cited

Almond, D.C., 1986a, The relation of Mesozoic-Cainozoic volcanism to tectonics in the Afro-Arabian dome: Journal of Volcanology and Geothermal Research, v. 28, p. 225–246, https://doi.org/10.1016/0377-0273(86)90024-7.

Almond, D.C., 1986b, Geological evolution of the Afro-Arabian dome: Tectonophysics, v. 131, p. 301–332, https://doi.org/10.1016/0040-1951(86)90180-0.

Armstrong, J.T., 1995, CITZAF—A package of correction programs for the quantitative electron microbeam X-ray analysis of thick polished materials, thin films, and particles: Microbeam Analysis, v. 4, p. 177–200.

Bachmann, O., and Bergantz, G.W., 2004, On the origin of crystal-poor rhyolites—Extracted from batholithic crystal mushes: Journal of Petrology, v. 45, p. 1565–1582, https://doi.org/10.1093/petrology/egh019.

Bedrosian, P.A., Peacock, J.R., Dhary, M., Sharif, A., Feucht, D.W., and Zahran, H., 2019, Crustal magmatism and anisotropy beneath the Arabian Shield—A cautionary tale: Journal of Geophysical Research Solid Earth, v. 124, no. 10, https://doi.org/10.1029/2019JB017903.

Bertrand, H., Chazot, G., Blichert-Toft, J., and Thoral, S., 2003, Implications of widespread high-µ volcanism on the Arabian Plate for Afar mantle plume and lithosphere composition: Chemical Geology, v. 198, p. 47–61, https://doi.org/10.1016/S0009-2541(02)00418-7.

Blundy, J.D., and Wood, B.J., 1991, Crystal-chemical controls on the partitioning of Sr and Ba between plagioclase feldspar, silicate melts, and hydrothermal solutions: Geochimica et Cosmochimica Acta, v. 55, p. 193–209, https://doi.org/10.1016/0016-7037(91)90411-W.

Bosworth, W., Huchon, P., and McClay, K., 2005, The Red Sea and Gulf of Aden Basins: Journal of African Earth Sciences, v. 43, no. 1–2, p. 334–378, https://doi.org/10.1016/j.jafrearsci.2005.07.020.

Calvert, A.T., Fierstein, J., and Hildreth, W., 2018, Eruptive history of Middle Sister, Oregon Cascades, USA—Product of a late Pleistocene eruptive episode: Geosphere, v. 14, p. 2118–2139, https://doi.org/10.1130/GES01638.1.

Calvert, A.T., and Lanphere, M.A., 2006, Argon geochronology of Kilauea's early submarine history: Journal of Volcanology and Geothermal Research, v. 151, p. 1–18, https://doi.org/10.1016/j.jvolgeores.2005.07.023.

Camp, V.E., Hooper, P.R., Roobol, M.J., and White, D.L., 1987, The Madinah eruption, Saudi Arabia—Magma mixing and simultaneous extrusion of three basaltic chemical types: Bulletin of Volcanology, v. 49, p. 489–508, https://doi.org/10.1007/BF01245475.

Camp, V.E., and Roobol, M.J., 1989, The Arabian continental alkali basalt province; Part I—Evolution of Harrat Rahat, Kingdom of Saudi Arabia: Geological Society of America Bulletin, v. 101, p. 71–95.

Camp, V.E., and Roobol, M.J., 1991, Geologic map of the Cenozoic lava field of Harrat Rahat, Kingdom of Saudi Arabia: Saudi Arabian Deputy Ministry for Mineral Resources Geoscience Map GM–123, scale 1:250,000, 37 p.

Camp, V.E., and Roobol, M.J., 1992, Upwelling asthenosphere beneath western Arabia and its regional implications: Journal of Geophysical Research, v. 97, no. B11, p. 15255–15271, https://doi.org/10.1029/92JB00943.

Coleman, R.G., Gregory, R.T., and Brown, G.F., 1983, Cenozoic volcanic rocks of Saudi Arabia: U.S. Geological Survey Open-File Report 83-788, 86 p., https://doi.org/10.3133/ofr83788.

Coleman, R.G., and McGuire, A.V., 1988, Magma systems related to the Red Sea opening: Tectonophysics, v. 150, p. 77–100, https://doi.org/10.1016/0040-1951(88)90296-X.

Condomines, M., Tanguy, J.-C., and Michaud, V., 1995, Magma dynamics at Mt Etna—Constraints from U-Th-Ra-Pb radioactive disequilibria and Sr isotopes in historical lavas: Earth and Planetary Science Letters, v. 132, p. 25–41, https://doi.org/10.1016/0012-821X(95)00052-E.

Cox, K.G., Bell, J.D., and Pankhurst, R.J., 1979, The Interpretation of Igneous Rocks: Springer Netherlands, Dordrecht, p. 42–82.

Dalrymple, G.B., Alexander, E.C., Lanphere, M.A., and Kraker, G.P., 1981, Irradiation of samples for ^{40}Ar/^{39}Ar dating using the Geological Survey TRIGA reactor: U.S. Geological Survey Professional Paper 1176, 55 p.

Desilets, D., Zreda, M., Almasi, P.F., and Elmore, D., 2006, Determination of cosmogenic ^{36}Cl in rocks by isotope dilution—Innovations, validation and error propagation: Chemical Geology, v. 233, p. 185–195, https://doi.org/10.1016/j.chemgeo.2006.03.001.

Downs, D.T., 2019, Major- and trace-element chemical analyses of rocks from the northern Harrat Rahat volcanic field and surrounding area, Kingdom of Saudi Arabia: U.S. Geological Survey data release, https://doi.org/10.5066/P91HL91C.

Downs, D.T., Robinson, J.E., Stelten, M.E., Champion, D.E., Dietterich, H.R., Sisson, T.W., Zahran, H., Hassan, K., and Shawai, J., 2019, Geologic map of the northern Harrat Rahat volcanic field, Kingdom of Saudi Arabia: U.S. Geological Survey Scientific Investigations Map 3428 [also released as Saudi Geological Survey Special Report SGS–SP–2019–2], 65 p., 4 sheets, scales 1:75,000, 1:25,000, https://doi.org/10.3133/sim3428.

Downs, D.T., Stelten, M.E., Champion, D.E., Dietterich, H.R., Nawab, Z., Zahran, H., Hassan, K., and Shawali, J., 2018, Volcanic history of the northernmost part of the Harrat Rahat volcanic field, Saudi Arabia: Geosphere, v. 14, p. 1253–1282, https://doi.org/10.1130/GES01625.1.

Duncan, R.A., Kent, A.J.R., Thornber, C.R., Schlieder, T.D., and Al-Amri, A.M., 2016, Timing and composition of continental volcanism at Harrat Hutaymah, western Saudi Arabia: Journal of Volcanology and Geothermal Research, v. 313, p. 1–14, https://doi.org/10.1016/j.jvolgeores.2016.01.010.

Ellis, B.S., Bachmann, O., and Wolff, J.A., 2014, Cumulate fragments in silicic ignimbrites—The case of the Snake River Plain: Geology, v. 42, p. 431–434, https://doi.org/10.1130/g35399.1.

Eppich, G.R., Cooper, K.M., Kent, A.J.R., and Koleszar, A., 2012, Constraints on crystal storage timescales in mixed magmas—Uranium-series disequilibria in plagioclase from Holocene magmas at Mount Hood, Oregon: Earth and Planetary Science Letters, v. 317–318, p. 319–330, https://doi.org/10.1016/j.epsl.2011.11.019.

Erdman, M.E., Lee, C-T.A., Levander, A., and Jiang, H., 2016, Role of arc magmatism and lower crustal foundering in controlling elevation history of the Nevadaplano and Colorado Plateau—A case study of pyroxenitic lower crust from central Arizona, USA: Earth and Planetary Science Letters, v. 439, p. 48–57, https://doi.org/10.1016/j.epsl.2016.01.032.

Fierstein, J., Hildreth, W., and Calvert, A.T., 2011, Eruptive history of South Sister, Oregon Cascades: Journal of Volcanology and Geothermal Research, v. 207, p. 145–179, https://doi.org/10.1016/j.jvolgeores.2011.06.003.

Fleck, R.J., Calvert, A.T., Coble, M.A., Wooden, J.L., Hodges, K., Hayden, L.A., van Soest, M.C., du Bray, E.A., and John, D.A., 2019, Characterization of the rhyolite of Bodie Hills and ^{40}Ar/^{39}Ar intercalibration with Ar mineral standards: Chemical Geology, v. 525, p. 282–302. no. 7, https://doi.org/10.1130/abs/2016AM-286011.

Fleck, R.J., Hagstrum, J.T., Calvert, A.T., Evarts, R.C., and Conrey, R.M., 2014, ^{40}Ar/^{39}Ar geochronology, paleomagnetism, and evolution of the Boring volcanic field, Oregon and Washington, USA: Geosphere, v. 10, p. 1283–1314, https://doi.org/10.1130/GES00985.1.

Hamilton, D.L., and MacKenzie, W.S., 1965, Phase-equilibrium studies in the system $NaAlSiO_4$ (Nepheline)-$KAlSiO_4$ (Kalsilite)-SiO_2-H_2O: Mineralogical Magazine, v. 34, p. 214–231, https://doi.org/10.1180/minmag.1965.034.268.17.

Hawkesworth, C.J., Blake, S., Evans, P., Hughes, R., MacDonald, R., Thomas, L.E., Turner, S.P., and Zellmer, G., 2000, Time scales of crystal fractionation in magma chambers—Integrating physical, isotopic and geochemical perspectives: Journal of Petrology, v. 41, p. 991–1006, https://doi.org/10.1093/petrology/41.7.991.

Hildreth, W., Halliday, A.N., and Christiansen, R.L., 1991, Isotopic and chemical evidence concerning the genesis and contamination of basaltic and rhyolitic magma beneath the Yellowstone Plateau volcanic field: Journal of Petrology, v. 32, p. 63–138.

Hildreth, W., and Moorbath, S., 1988, Crustal contributions to arc magmatism in the Andes of Central Chile: Contributions to Mineralogy and Petrology, v. 98, p. 455–489, https://doi.org/10.1007/BF00372365.

Johnson, D.M., Hooper, P.R., and Conrey, R.M., 1999, XRF analysis of rocks and minerals for major and trace elements on a single low dilution Li-tetraborate fused bead: Advances in X-ray Analysis, v. 41, p. 843–867.

Knaack, C., Hooper, P.R., and Cornelius, S., 1994, Trace element analyses of rocks and minerals by ICP-MS: Pullman, Washington State University, Department of Geology Technical Notes, accessed on July 31, 2020, at https://environment.wsu.edu/facilities/geoanalytical-lab/technical-notes/icp-ms-method.

Lal, D., 1991, Cosmic ray labeling of erosion surfaces—In situ nuclide production rates and erosion models: Earth and Planetary Science Letters, v. 104, p. 424–439, https://doi.org/10.1016/0012-821X(91)90220-C.

Lee, J.Y., Marti, K., Severinghaus, J.P., Kawamura, K., Yoo, H-S., Lee, J.B., and Kim, J.S., 2006, A redetermination of the isotopic abundances of atmospheric Ar: Geochimica et Cosmochimica Acta, v. 70, p. 4507–4512, https://doi.org/10.1016/j.gca.2006.06.1563.

Lindsley, D.H., ed., 1991, Oxide minerals—Petrologic and magnetic significance: Reviews in Mineralogy, v. 25, 509 p.

Lowenstern, J.B., Charlier, B.L.A., Clynne, M.A., and Wooden, J.L., 2006, Extreme U-Th disequilibrium in rift-related basalts, rhyolites and granophyric granite and the timescale of rhyolite generation, intrusion and crystallization at Alid volcanic center, Eritrea: Journal of Petrology, v. 47, p. 2105–2122, https://doi.org/10.1093/petrology/egl038.

Macdonald, G.A., and Katsura, T., 1964, Chemical composition of Hawaiian lavas: Journal of Petrology, v. 5, p. 82–133.

Marrero, S.M., Phillips, F.M., Borchers, B., Lifton, N., Aumer, R., and Balco, G., 2016, Cosmogenic nuclide systematics and the CRONUScalc program: Quaternary Geochronology, v. 31, p. 160–187, https://doi.org/10.1016/j.quageo.2015.09.005.

McElhinny, M.W., and McFadden, P.L., eds., 2000, Rock Magnetism, *in* Paleomagnetism: Academic Press, p. 31–77.

McGee, L.E., Millet, M.-A., Smith, I.E.M., Németh, K., and Lindsay, J.M., 2012, The inception and progression of melting in a monogenetic eruption—Motukorea Volcano, the Auckland Volcanic Field, New Zealand: Lithos, v. 155, p. 360–374, https://doi.org/10.1016/j.lithos.2012.09.012.

McGuire, A.V., and Stern, R.J., 1993, Granulite xenoliths from western Saudi Arabia—The lower crust of the late Precambrian Arbian-Nubian Shield: Contributions to Mineralogy and Petrology, v. 114, p. 395–408, https://doi.org/10.1007/BF01046541.

Morimoto, N., 1988, Nomenclature of pyroxenes: Mineralogy and Petrology, v. 39, p. 55–76, https://doi.org/10.1007/BF01226262.

Morimoto, N., Fabries, J., Ferguson, A.K., Ginzburg, I.V., Ross, M., Seifert, F.A., Zussman, J., Aoki, K., and Gottardi, G., 1998, Nomenclature of pyroxenes: American Mineralogist, v. 73, p. 1123–1133.

Moufti, M.R.H., 1985, The geology of Harrat Al Madinah volcanic field, Harrat Rahat, Saudi Arabia: Lancaster, U.K., University of Lancaster, Ph.D. thesis, 407 p.

Moufti, M.R.H., Moghazi, A.M., and Ali, K.A., 2012, Geochemistry and Sr-Nd-Pb isotopic composition of the Harrat Al-Madinah Volcanic Field, Saudi Arabia: Gondwana Research, v. 21, p. 670–689, https://doi.org/10.1016/j.gr.2011.06.003.

Moufti, M.R.H., Moghazi, A.M., and Ali, K.A., 2013, ^{40}Ar/^{39}Ar geochronology of the Neogene-Quaternary Harrat Al-Madinah intercontinental volcanic field, Saudi Arabia—Implications for duration and migration of volcanic activity: Journal of Asian Earth Sciences, v. 62, p. 253–268, https://doi.org/10.1016/j.jseaes.2012.09.027.

Murcia, H., Lindsay, J.M., Németh K., Smith, I.E.M., Cronin, S.J., Moufti, M.R.H., El-Masry, N.N., and Niedermann, S., 2017, Geology and geochemistry of Late Quaternary volcanism in northern Harrat Rahat, Kingdom of Saudi Arabia—Implications for eruption dynamics, regional stratigraphy and magma evolution: Geological Society of London, Special Publications, v. 446, p. 173–204.

Murcia, H., Németh, K., El-Masry, N.N., Lindsay, J.M., Moufti, M.R.H., Wameyo, P., Cronin, S.J., Smith, I.E.M., and Kereszturi, G., 2015, The Al-Du'aythah volcanic cones, Al-Madinah City—Implications for volcanic hazards in northern Harrat Rahat, Kingdom of Saudi Arabia: Bulletin of Volcanology, v. 77, no. 54, 19 p., https://doi.org/10.1007/s00445-015-0936-9.

Peacock, J.R., Bedrosian, P.A., Al-Dhahry, M.K., Shareef, A., Feucht, D.W., Taylor, C.D., Bloss, B., and Zahran, H.M., 2023, Magnetotelluric investigation of northern Harrat Rahat, Kingdom of Saudi Arabia, chap. L *of* Sisson, T.W., Calvert, A.T., and Mooney, W.D., eds., Active volcanism on the Arabian Shield—Geology, volcanology, and geophysics of northern Harrat Rahat and vicinity, Kingdom of Saudi Arabia: U.S. Geological Survey Professional Paper 1862 [also released as Saudi Geological Survey Special Report SGS–SP–2021–1], 111 p., https://doi.org/10.3133/pp1862L.

Pellaton, C., 1981, Geologic map of the Al Madinah quadrangle, sheet 24D, Kingdom of Saudi Arabia: Saudi Arabian Deputy Ministry for Mineral Resources Geologic Map GM-52, scale 1:250,000, 19 p.

Pitcher, B.W., Kent, A.J.R., Grunder, A.L., and Duncan, R.A., 2017, Frequency and volumes of ignimbrite eruptions following the Late Neogene initiation of the Central Oregon High Cascades: Journal of Volcanology and Geothermal Research, v. 339, p. 1–22, https://doi.org/10.1016/j.jvolgeores.2017.04.019.

Robinson, J.E., and Downs, D.T., 2023, Overview of the Cenozoic geology of the northern Harrat Rahat volcanic field, Kingdom of Saudi Arabia, chap. R *of* Sisson, T.W., Calvert, A.T., and Mooney, W.D., eds., Active volcanism on the Arabian Shield—Geology, volcanology, and geophysics of northern Harrat Rahat and vicinity, Kingdom of Saudi Arabia: U.S. Geological Survey Professional Paper 1862 [also released as Saudi Geological Survey Special Report SGS–SP–2021–1], 20 p., scale 1:100,000, https://doi.org/10.3133/pp1862R.

Rumble, D., ed., 1976, Oxide minerals: Reviews in Mineralogy, v. 3, 706 p.

Salters, V.J.M., Sachi-Kocher, A., Downs, D.T., Stelten, M.E., and Sisson, T.W., 2023, Isotopic and geochemical evidence for the source of volcanism at Harrat Rahat, Kingdom of Saudi Arabia, chap. J *of* Sisson, T.W., Calvert, A.T., and Mooney, W.D., eds., Active volcanism on the Arabian Shield—Geology, volcanology, and geophysics of northern Harrat Rahat and vicinity, Kingdom of Saudi Arabia: U.S. Geological Survey Professional Paper 1862 [also released as Saudi Geological Survey Special Report SGS–SP–2021–1], 30 p., https://doi.org/10.3133/pp1862J.

Shaw, J.E., Baker, J.A., Menzies, M.A., Thirlwall, M.F., and Ibrahim, K.M., 2003, Petrogenesis of the largest intraplate volcanic field on the Arabian Plate (Jordan)—A mixed lithosphere–asthenosphere source activated by lithospheric extension: Journal of Petrology, v. 44, p. 1657–1679, https://doi.org/10.1093/petrology/egg052.

Sisson, T.W., Downs, D.T., Calvert, A.T., Dietterich, H.R., Mahood, G.A., Salters, V.J.M., Stelten, M.E., and Shawali, J., 2023, Mantle origin and crustal differentiation of basalts and hawaiites of northern Harrat Rahat, Kingdom of Saudi Arabia, chap. I *of* Sisson, T.W., Calvert, A.T., and Mooney, W.D., eds., Active volcanism on the Arabian Shield—Geology, volcanology, and geophysics of northern Harrat Rahat and vicinity, Kingdom of Saudi Arabia: U.S. Geological Survey Professional Paper 1862 [also released as Saudi Geological Survey Special Report SGS–SP–2021–1], 42 p., https://doi.org/10.3133/pp1862I.

Smith, I.E.M., Blake, S., Wilson, C.J.N., and Houghton, B.F., 2008, Deep-seated fractionation during the rise of a small-volume basalt magma batch—Crater Hill, Auckland, New Zealand: Contributions to Mineralogy and Petrology, v. 155, p. 511–527, https://doi.org/10.1007/s00410-007-0255-z.

Steiger, R.H., and Jäger, E., 1977, Subcommission on geochronology—Convention on the use of decay constants in geo- and cosmochronology: Earth and Planetary Science Letters, v. 36, p. 359–362, https://doi.org/10.1016/0012-821X(77)90060-7.

Stein, M., and Hofmann, A.W., 1992, Fossil plume head beneath the Arabian lithosphere?: Earth and Planetary Science Letters, v. 114, p. 193–209, https://doi.org/10.1016/0012-821X(92)90161-N.

Stelten, M.E., 2021, Ar isotope data for volcanic rocks from the northern Harrat Rahat volcanic field and surrounding area, Kingdom of Saudi Arabia: U.S. Geological Survey data release, https://doi.org/10.5066/P92FB6AQ.

Stelten, M.E., Cooper, K.M., Vazquez, J.A., Calvert, A.T., and Glessner, J.J.G., 2015, Mechanisms and timescales of generating eruptible rhyolitic magmas at Yellowstone Caldera from zircon and sanidine geochronology and geochemistry: Journal of Petrology, v. 56, p. 1607–1642, https://doi.org/10.1093/petrology/egv047.

Stelten, M.E., and Downs, D.T., 2022, Electron microprobe data for plagioclase, olivine, pyroxene, and spinel in volcanic rocks from the Matan volcanic center located within the Harrat Rahat volcanic field, Kingdom of Saudi Arabia: U.S. Geological Survey data release, https://doi.org/10.5066/P9ENRS8U.

Stern, R.J., and Johnson, P., 2010, Continental lithosphere of the Arabian Plate—A geologic, petrologic, and geophysical synthesis: Earth-Science Reviews, v. 101, p. 29–67.

Stone, J.O., 2000, Air pressure and cosmogenic isotope production: Journal of Geophysical Research Solid Earth, v. 105, p. 23753–23759, https://doi.org/10.1029/2000JB900181.

Taggart, J.E., Jr., ed., 2002, Analytical methods for chemical analysis of geologic and other materials, U.S. Geological Survey: U.S. Geological Survey Open-File Report 02-223.

Thomas, L.E., 1999, Uranium series, major and trace element geochemistry of lavas from Tenerife and Lanzarote, Canary Islands: Milton Keynes, U.K., The Open University, Ph.D. thesis, 245 p.

Thompson, R.N., 1975, Primary basalts and magma genesis—II., Snake River Plain, Idaho, U.S.A.: Contributions to Mineralogy and Petrology, v. 52, p. 213–232, https://doi.org/10.1007/BF00457295.

Tuttle, O., and Bowen, N.L., 1958, Origin of granite in the light of experimental studies in the system $NaAlSi_3O_8$-$KAlSi_3O_8$-SiO_2-H_2O: Geological Society of America Memoirs, v. 74, p. 1–146, https://doi.org/10.1130/MEM74-p1.

Welch, B.L., 1947, The generalization of ‘Student’s’ problem when several different population variances are involved: Biometrika, v. 34, p. 28–35, https://doi.org/10.2307/2332510.

Widom, E., Schmincke, H.-U., and Gill, J.B., 1992, Processes and timescales in the evolution of a chemically zoned trachyte—Fogo A, Sao Miguel, Azores: Contributions to Mineralogy and Petrology, v. 111, p. 311–328, https://doi.org/10.1007/BF00311194.

Wolff, J.A., 2017, On the syenite-trachyte problem: Geology, v. 47, p. 1067–1070, https://doi.org/10.1130/G39415.1.

Appendix 1. Detailed Description of Analytical Methods

^{40}Ar/^{39}Ar Dating

Groundmass separates from basalt, mugearite, benmoreite, and trachyte were prepared for dating via the ^{40}Ar/^{39}Ar method. Dense samples with a crystalline groundmass were chosen for analysis. Samples were crushed, ultrasonicated, and sieved to 250–355 micrometers (µm). Groundmass was separated from phenocryst phases using a Frantz magnetic separator and careful handpicking under a binocular microscope. For trachyte and some benmoreite samples, feldspar separates (anorthoclase or sanidine) were prepared from the 250–355 µm size fraction of crushed whole rock samples by standard magnetic and density separation techniques. Approximately 150 milligrams (mg) of material was prepared for each groundmass separate, and ~50 mg of material was prepared for each feldspar separate. Prior to irradiation, the feldspar separates were leached using 8-percent hydrofluoric acid following the procedure outlined by Stelten and others (2015) to remove any glass adhering to the sanidine crystals. The sanidine crystals were then inspected under a binocular microscope after leaching to ensure that no fluoride compounds were deposited on the sanidine crystals.

Groundmass and feldspar separates were packaged in copper or aluminum foil along with Bodie Hills sanidine monitor minerals (9.7946±0.0033; Fleck and others, 2019) and encapsulated in quartz vials. The quartz vials were wrapped in 0.5-millimeter-thick cadmium foil to shield samples from thermal neutrons during irradiation. Samples were irradiated for 1 hour in the central thimble of the U.S. Geological Survey (USGS) TRIGA reactor in Denver, Colorado (Dalrymple and others, 1981), at a power level of 1 megawatt. For incremental heating analysis of groundmass and bulk feldspar separates, the argon was extracted in discrete temperature steps using a molybdenum crucible in a custom resistance furnace attached to a MAP 216 mass spectrometer at the USGS Menlo Park facility. Prior to measurement of argon isotopic composition, groundmass separates were degassed at 500 degrees Celsius (°C) and sanidine separates were degassed at 600 °C until undesirable gases (for example, water, nitrogen, and hydrocarbons as measured by a Granville-Phillips 835 VQM system) were reduced to acceptable levels. For laser total fusion analyses of fluence monitors and single feldspar grains from select trachyte and benmoreite samples, argon was extracted in a single heating step using a New Wave CO_2 laser coupled with a MAP 216 mass spectrometer. For all experiments, extracted argon was exposed to a 4-ampere tungsten filament, 125 kelvin cold finger, and two SAES ST-175 getters (one operated at 300 °C, and one at room temperature) to remove active gasses.

Uncertainties in reported sanidine ^{40}Ar/^{39}Ar ages include propagated uncertainties in counting statistics and J values. Instrumental mass discrimination was calculated by repeated measurement of atmospheric argon. Argon isotope measurements presented in this study were made over the time period from December 2014 to July 2017. Initially, ages and mass discrimination were calculated assuming $^{40}\text{Ar}/^{36}\text{Ar}_{\text{atmosphere}}$ = 295.5±0.5 (Steiger and Jäger, 1977), but starting in May 2016 the Menlo Park Argon Laboratory began calculating ages and mass discrimination assuming $^{40}\text{Ar}/^{36}\text{Ar}_{\text{atmosphere}}$ = 298.56±0.31 (Lee and others, 2006). The assumed isotope ratio of atmospheric argon used when calculating each age is noted in table 1 of the main text. The change in the assumed ^{40}Ar/^{36}Ar of atmospheric argon does not result in a bias in ages because both monitors and unknowns from each irradiation were calculated in the same manner. See Calvert and Lanphere (2006) and Fleck and others (2014) for additional details regarding analytical techniques, mass spectrometer design, and irradiation procedures.

^{36}Cl Cosmogenic Surface-Exposure Dating

Two samples for ^{36}Cl cosmogenic surface-exposure dating were collected from within the mapping area. Samples R15MS004 and R15TS189 were both collected from the basalt of Musawda'ah (fig. 9 of the main text). Sample R15MS004 is a whole-rock sample collected from a flat surface on the crater rim of the source vent for the basalt of Musawda'ah and is composed of vesicular basalt with 3 to 5 percent plagioclase phenocrysts as large as 5 centimeters (cm). Sample R15TS189 consists of 0.5- to 1.5-cm-long plagioclase phenocrysts collected from a flat part of the basalt of Musawda'ah, ~3.7 kilometers from the source vent. The plagioclase phenocrysts collected were loose on the surface of the flow, but are petrographically identical to plagioclase phenocrysts within the basalt of Musawda'ah and were likely eroded from the surface of the lava flow shortly after emplacement. These plagioclase phenocrysts are interpreted to be derived from the upper centimeter of the lava flow's surface.

Whole-rock sample R15MS004 was trimmed such that only the upper ~4 cm of material was analyzed. For both R15MS004 and R15TS189, the dip of the sample surface collected was negligible (<5°). At all sample locations, shielding was negligible, with the angle to the horizon ≤6° in all directions. Sample locations and elevations were measured by Global Positioning System using the World Geodetic System of 1984 datum and Universal Transverse Mercator zone 37R (north) coordinate system, and later confirmed using a 1-meter-resolution digital elevation model. Erosion rates are estimated to be low (≤1 mm per thousand years [mm/k.y.]) based on the preservation of small-scale (<1 cm), irregular surface features on each flow. Given the uncertainty in the erosion rate for each sample site, we conservatively assume an erosion rate of 1±1 mm/k.y.

Chemical separation and analysis of samples via accelerator mass spectrometry took place at the Purdue Rare Isotope Measurement (PRIME) Laboratory at Purdue University in West Lafayette, Indiana. Samples were chemically dissolved, spiked with a ^{35}Cl enriched tracer (for example, Desilets and others, 2006), and analyzed via accelerator mass spectrometry. Splits of each sample were analyzed for their major-element concentrations via wavelength dispersive X-ray fluorescence (XRF) and for their trace-element concentrations via inductively coupled plasma atomic emission spectrometry (ICP-AES) and inductively coupled plasma mass spectrometry (ICP-MS) at the U.S. Geological Survey in Denver, Colorado, following Taggart (2002). Trace-elements of particular importance for the calculation of ^{36}Cl cosmogenic surface-exposure ages are U and Th, which can indirectly produce thermal neutrons as a result of alpha decay, and B, Li, Sm, and Gd, which have large thermal neutron absorption cross sections, and therefore reduce the production of ^{36}Cl from ^{35}Cl. Of these elements, all were above detection limits except for B and Li. Given that the detection limit for B and Li is 10 parts per million (ppm), we assume the concentration of B and Li in each sample is 5±5 ppm.

Cosmogenic surface-exposure ages were calculated using the online CRONUScalc ^{36}Cl Exposure Age Calculator ver. 2.0 (visit the Cosmic-Ray Produced Nuclide Systematics on Earth Project webpage at http://www.physics.purdue.edu/primelab/CronusProject/cronus for more information) that utilizes a MATLAB-based code and is described by Marrero and others (2016). Ages were calculated using the Lal and Stone time-independent scaling model (Lal, 1991; Stone, 2000). Refer to Marrero and others (2016) for a detailed discussion of production rates for various production pathways, details of scaling models, and other parameters used in the calculation of ^{36}Cl cosmogenic surface-exposure ages.

References Cited

Calvert, A.T., and Lanphere, M.A., 2006, Argon geochronology of Kilauea's early submarine history: Journal of Volcanology and Geothermal Research, v. 151, p. 1–18, https://doi.org/10.1016/j.jvolgeores.2005.07.023.

Dalrymple, G.B., Alexander, E.C., Lanphere, M.A., and Kraker, G.P., 1981, Irradiation of samples for ^{40}Ar/^{39}Ar dating using the Geological Survey TRIGA reactor: U.S. Geological Survey Professional Paper 1176, 55 p.

Desilets, D., Zreda, M., Almasi, P.F., and Elmore, D., 2006, Determination of cosmogenic ^{36}Cl in rocks by isotope dilution—Innovations, validation and error propagation: Chemical Geology, v. 233, p. 185–195, https://doi.org/10.1016/j.chemgeo.2006.03.001.

Fleck, R.J., Hagstrum, J.T., Calvert, A.T., Evarts, R.C., and Conrey, R.M., 2014, ^{40}Ar/^{39}Ar geochronology, paleomagnetism, and evolution of the Boring volcanic field, Oregon and Washington, USA: Geosphere, v. 10, p. 1283–1314, https://doi.org/10.1130/GES00985.1.

Fleck, R.J., Calvert, A.T., Coble, M.A., Wooden, J.L., Hodges, K., Hayden, L.A., van Soest, M.C., du Bray, E.A., and John, D.A., 2019, Characterization of the rhyolite of Bodie Hills and ^{40}Ar/^{39}Ar intercalibration with Ar mineral standards: Chemical Geology, v. 525, p. 282–302.

Lal, D., 1991, Cosmic ray labeling of erosion surfaces—In situ nuclide production rates and erosion models: Earth and Planetary Science Letters, v. 104, p. 424–439, https://doi.org/10.1016/0012-821X(91)90220-C.

Lee, J.Y., Marti, K., Severinghaus, J.P., Kawamura, K., Yoo, H-S., Lee, J.B., and Kim, J.S., 2006, A redetermination of the isotopic abundances of atmospheric Ar: Geochimica et Cosmochimica Acta, v. 70, p. 4507–4512, https://doi.org/10.1016/j.gca.2006.06.1563.

Marrero, S.M., Phillips, F.M., Borchers, B., Lifton, N., Aumer, R., and Balco, G., 2016, Cosmogenic nuclide systematics and the CRONUScalc program: Quaternary Geochronology, v. 31, p. 160–187, https://doi.org/10.1016/j.quageo.2015.09.005.

Steiger, R.H., and Jäger, E., 1977, Subcommission on geochronology—Convention on the use of decay constants in geo- and cosmochronology: Earth and Planetary Science Letters, v. 36, p. 359–362, https://doi.org/10.1016/0012-821X(77)90060-7.

Stelten, M.E., Cooper, K.M., Vazquez, J.A., Calvert, A.T., and Glessner, J.J.G., 2015, Mechanisms and timescales of generating eruptible rhyolitic magmas at Yellowstone Caldera from zircon and sanidine geochronology and geochemistry: Journal of Petrology, v. 56, p. 1607–1642, https://doi.org/10.1093/petrology/egv047.

Stone, J.O., 2000, Air pressure and cosmogenic isotope production: Journal of Geophysical Research Solid Earth, v. 105, p. 23753–23759, https://doi.org/10.1029/2000JB900181.

Taggart, J.E., Jr., ed., 2002, Analytical methods for chemical analysis of geologic and other materials, U.S. Geological Survey: U.S. Geological Survey Open-File Report 02-223.

Appendix 2. Location of Samples from the Matan Volcanic Center

Table 2.1. Sample number and locations of eruptive products from the Matan volcanic center.

[Sample names with an asterisk are those that have been dated via the $^{40}Ar/^{39}Ar$ or ^{36}Cl method. Easting and northing are reported in World Geodetic System of 1984 datum using the Universal Transverse Mercator zone 37R (north) coordinate system]

Sample number	Easting	Northing
Trachyte of Dabaa 1 (unit td1)		
R14AC017*	592217	2679181
R14AC016	592186	2679424
R15DD095	592075	2678462
R15TS208	591675	2677928
Trachyte of Mouteen (unit tmo)		
R14TRO016	586015	2678169
R14TS027	586084	2678089
R14TS028*	586169	2678421
R15AC104	586809	2678668
R16DD229	586217	2677640
R14TS036	585147	2678697
R15MS007	586575	2678605
R16MS105	585046	2678279
Hawaiite of Al Anahi 3 (unit han3)		
R14TRO133	572287	2690493
R14DS007	582139	2684296
R14DS019	570244	2689670
R14DS071	579363	2683815
R15TS153	570324	2692263
R15TS158	571577	2693259
R15TS163	574462	2687945
R15TS164	574315	2687303
R15TS166	573446	2686639
R15TS168	573936	2684583
R15TS177	569640	2681190
R15TS179	573940	2682581
R15MS005	579196	2681997
Basalt of Musawda'ah (unit bms)		
R14AC059	580317	2680919
R14AC060	580317	2680919
R15AC103	579016	2681991
R14DC010	571817	2684421
R14DC039	567436	2682560
R15DC044	560661	2683949
R14TRO115	560664	2684108
R14TRO119	570151	2675554
R14DS022	567438	2682565
R15TS180	577645	2681178
Basalt of Musawda'ah (unit bms)—Continued		
R15TS186	577728	2675098
R15MS023	571262	2675889
R14AC058	580868	2680708
Trachyte of Gura 2 (unit tg2)		
R14AC010*	589155	2676995
R14AC086*	589321	2677183
R14AC087	589016	2677265
R14AC091	590235	2677650
R14AC092	590310	2677594
R16DD230	588611	2676166
R16DD231A	588654	2676209
R16DD231B	588654	2676209
R14TS003	588602	2676036
Basalt of Shai'ab Abu Sikhbir (unit bsas)		
R14AC023	592551	2679892
R14AC068*	596910	2677863
R15DD097	592837	2678276
R15DD098	592708	2678191
R15DS201	593677	2680909
R15DS203	596018	2682239
R15DS199	604129	2676235
R15TS205	593302	2677797
Mugearite of Dabaa 1 (unit md1)		
R14AC019*	592238	2679266
R14AC020	591515	2679159
R14AC021*	591693	2679691
R14AC024	592731	2680066
R14TS041	589829	2680957
R16MS092	588392	2678898
R14AC089	589307	2677501
R16MS094	588028	2677427
R16MS095	588034	2677502
Trachyte of Matan (unit tma)		
R14TS068*	585375	2679376
R14TRO028	584579	2679596
R16MS097	585484	2680324
R16MS104	585050	2678278

Table 2.1. Sample number and locations of eruptive products from the Matan volcanic center.—Continued.

Sample number	Easting	Northing
Benmoreite of Gura 2 (unit og2)		
R14AC090*	590214	2677944
R15TS214	590434	2677592
R16MS101	590360	2678023
Basalt of Abu Rimthah (unit bar)		
R14AC069*	590358	2681448
R15DS209	599205	2684804
Trachyte of Gura 3 (unit tg3)		
R15AC108	588430	2675067
R16DD233	589008	2675821
R16DD234	589033	2675691
R16DD235	589031	2675685
R16DD236B	589002	2675592
R16DD236C	588979	2675523
R16DD238	589011	2675292
R16DD241	588864	2674752
R16DD246	587901	2675497
R15MS010*	588560	2675414
R15MS012	588216	2675174
Basalt of Sha'ib Iskabah (unit bsi)		
R14AC001	587261	2683475
R15DD104	583420	2682169
R14TS033*	584610	2681045
R15MS002	587251	2683501
R14TS038	586946	2681122
Mugearite of Matan (unit mma)		
R14AC002	586035	2679566
R14TRO026	584785	2680831
R14TRO030	586219	2681189
R14TS034	584207	2679875
R14TS037	585894	2680960
R14TS039	587135	2681177
R14TS085	582900	2676780
R14TS131*	580449	2675225
R16MS096	585492	2680327
R15AC106	586905	2678612
Mugearite of Al Mulaysa (unit mmu)		
R14AC096*	588989	2672786
R15AC116	586373	2672650
R14DS062	593271	2673124
R14TS074*	584781	2672259
R14TS081*	595374	2673921
R14TS082*	595378	2673907
R14TS134	590567	2673741
Mugearite of Al Mulaysa (unit mmu)—Continued		
R14TS136	590179	2673530
R14TS138	589373	2672769
Basalt of Ad Darah (unit bda)		
R15AC109	588402	2675058
R14TS002	588654	2676005
R14TS075	584470	2672365
R14TS076	583698	2672213
R14TS077	583409	2672824
R14TS130*	580964	2672737
R15MS044	586402	2672664
R15AC110	588669	2674726
R15MS013	589021	2674895
Basalt of Al Malsaa 1 (unit bm1)		
R14TS031	585916	2676087
R14TS032	586177	2675955
R15MS042*	585621	2675281
Basalt of Sha'ib Hayaya (unit bhy)		
R14TS135	590545	2673751
R15TS201	594492	2676622
R15TS202*	593341	2676141
R15TS203	592767	2675731
Hawaiite of Mouteen (unit hmo)		
R14TRO006	584600	2679009
R14TRO007	584177	2678289
R14TRO029*	585148	2678873
R14TS067	585407	2679438
R16MS102	584617	2678302
R16MS099	585477	2678475
Benmoreite of Al Bayadah (unit oba)		
R14TRO012	584542	2675853
R14TRO018	585699	2677300
R14TRO019	585646	2676920
R14TS030	585080	2676620
R14TS083*	583976	2676263
Basalt of Amlit 1 (unit bam1)		
R14AC061	584690	2682961
R15MS003*	583569	2682186
R14AC062	584993	2682844
Basalt of Upper Abu Rimthah (unit burr)		
R14DS068*	594438	2683558
R15DS202	594019	2681251
R15TS200	598315	2676416
R16MS070*	598392	2681297

Table 2.1. Sample number and locations of eruptive products from the Matan volcanic center.—Continued.

Sample number	Easting	Northing
Basalt of Upper Abu Rimthah (unit burr)—Continued		
R17JRD006	594001	2683093
Benmoreite of Um Junb, dome 2 (unit oju)		
R14AC013*	590399	2675875
R15TS204	591597	2675854
Benmoreite of Um Junb, dome 1 (unit oju)		
R14TS069*	590688	2676356
R14TS070*	590357	2676968
R14AC012	589923	2676836
R15TS211	591297	2677115
R15TS210	591382	2677130
R15TS212	590966	2677824
R15TS213	590965	2677825
Basalt of Sha'ib Si'ayd (unit bss)		
R16MS085*	580873	2671355
Benmoreite of As Sabah (unit osb)		
R15TS206*	594307	2677881
Benmoreite of Gura 3 (unit og3)		
R14AC003*	588825	2675913
Basalt of Al Bayadah (unit bba)		
R14TS084*	583592	2676619
Basalt of Dabaa 1 (unit bd1)		
R14AC018	592242	2679233
R14AC022	592479	2679699
R14AC088	589261	2677501
R15DD087	592251	2678480
R15TS207	591885	2677947
R16MS100	590494	2678319
R15TS209	591408	2677296
Basalt of Gura 3 (unit bg3)		
R14DS001*	588701	2675770
Basalt of Al Malsaa 2 (unit bm2)		
R14TS078	586269	2677285
R14TS079	586264	2677112
Hawaiite of Al Malsaa 3 (unit hm3)		
R15AC107	586906	2676453
R15MS008	587182	2676149
R14TS080	586542	2676619
R15MS009	586858	2676442
Basalt west of Abu Rimthah (unit bwar)		
R15DS161	588971	2682190
R14TRO032	587506	2680903
Basalt west of Matan (unit bwm)		
R16MS103	583118	2679415

Appendix 3. ^{36}Cl Results

This appendix includes input parameters and full output for ^{36}Cl surface-exposure age calculations using the online CRONUScalc ^{36}Cl Exposure Age Calculator ver. 2.0 (Marrero and others, 2016). Ages were calculated using the Lal and Stone time-independent scaling model (Lal, 1991; Stone, 2000). See appendix 1 for details on analytical methods, sample characteristics, and data reduction methods.

Table 3.1. ^{36}Cl output parameters.

[Easting and northing are reported in the World Geodetic System of 1984 datum using the Universal Transverse Mercator zone 37R (north) coordinate system. Scaling values are unitless. *Q* is the ratio of the production rate, integrated over the thickness of the sample, to the surface production rate. ka, kilo-annum; mm/k.y., millimeter per thousand years; atoms/g/yr, atoms per gram per year; g, gram]

Parameter (units)	Sample R15MS004	Sample R15TS189
Easting	580779	578242
Northing	2680668	2677857
Geologic unit	Basalt of Musawda'ah (unit bms)	Basalt of Musawda'ah (unit bms)
Material	Groundmass	Plagioclase
Age (ka)	66	56.5
Uncertainty as ±1σ (ka)	11	6.7
Erosion rate (mm/k.y.)	0.195	0.268
Scaling Ca spallation	1.5771	1.4705
Scaling K spallation	1.5771	1.4705
Scaling Fe spallation	1.5771	1.4705
Scaling Ti spallation	1.5771	1.4705
Scaling Cl epithermal	1.5771	1.4705
Scaling Cl thermal	1.5771	1.4705
Scaling fast muons	1.1874	1.1374
Scaling slow muons	1.1874	1.1374
Production Ca spallation (atoms/g/yr)	4.6878	6.2482
Production K spallation (atoms/g/yr)	1.6082	0.4351
Production Fe spallation (atoms/g/yr)	0.27837	0.0081542
Production Ti spallation (atoms/g/yr)	0.16435	0.0043715
Production Ca muons (atoms/g/yr)	0.18778	0.25471
Production K muons (atoms/g/yr)	0.064388	0.017682
Production Cl low energy (atoms/g/yr)	6.5928	0.023203
Thermal neutron absorption cross section, σ_{th}	0.0081636	0.008152
Epithermal neutron absorption cross section, σ_{eth}	0.02126	0.019303
Neutron scattering cross section, σ_{sc}	0.10738	0.10556
Spallation production ratio, Q_s	0.98036	1.0291
Thermal neutron production ratio, Q_{th}	1.1956	1.0692
Epithermal neutron production ratio, Q_{eth}	1.1117	1.0477
Muon production ratio, Q_{mu}	0.99558	0.99869
Cosmogenic Cl (^{36}Cl/g)	889,152.1	355,136.4
Radiogenic Cl (^{36}Cl/g)	4,944.9	20.6
Analytical (internal) uncertainty (^{36}Cl/g)	4.9	3.8
Percentage of ^{36}Cl production from Ca	35.89	93.01
Percentage of ^{36}Cl production from K	12.31	6.476

Table 3.2. ^{36}Cl input parameters.

[mASL, meter above sea level; hPa, hectopascal; cm, centimeter; g/cm^3, gram per cubic centimeter; mm/k.y., millimeter per thousand years; g, gram; g/cm^2, gram per square centimeter; vol., volume; wt. %, weight percent; ppm, parts per million; m, meter; %, percent; NaN, null value]

Parameter (units)	Sample R15MS004	Sample R15TS189
Elevation (mASL)	1,022.8	923.7
Pressure (hPa)	899.7	909.9
Sample thickness (cm)	4	1
Bulk density (g/cm^3)	1.95	2.68
Shielding factor	1	1
Erosion rate (mm/k.y.)	1	1
^{36}Cl (atoms/g)	894,097	355,157
Attenuation length (g/cm^2)	165	165
Depth to top of sample (cm)	0	0
Year collected (C.E.)	2015	2015
Water content in pores (vol. fraction)	0.01	0.01
Mineral separation	No	Yes
Bulk-rock SiO_2 (wt. %)	46.5	46.5
Bulk-rock TiO_2 (wt. %)	3.56	3.56
Bulk-rock Al_2O_3 (wt. %)	17.9	17.9
Bulk-rock Fe_2O_3 (wt. %)	13.9	13.9
Bulk-rock MnO (wt. %)	0.2	0.2
Bulk-rock MgO (wt. %)	4.83	4.83
Bulk-rock CaO (wt. %)	8.17	8.17
Bulk-rock Na_2O (wt. %)	3.96	3.96
Bulk-rock K_2O (wt. %)	0.84	0.84
Bulk-rock P_2O_5 (wt. %)	0.49	0.49
Analytical water (wt. %)	0.29383	0.29383
Bulk-rock CO_2 (wt. %)	0.2	0.2
Bulk-rock Cl (ppm)	144.1	144.1
Bulk-rock B (ppm)	5	5
Bulk-rock Sm (ppm)	3.6	3.6
Bulk-rock Gd (ppm)	3.8	3.8
Bulk-rock U (ppm)	0.33	0.33
Bulk-rock Th (ppm)	1	1
Bulk-rock Cr (ppm)	11	11
Bulk-rock Li (ppm)	5	5
Target K_2O (wt. %)	NaN	0.24
Target CaO (wt. %)	NaN	11.5
Target TiO_2 (wt. %)	NaN	0.1
Target Fe_2O_3 (wt. %)	NaN	0.43
Target Cl (ppm)	NaN	0.6
Latitude uncertainty (decimal degrees)	0.00001	0.00001
Longitude uncertainty (decimal degrees)	0.00001	0.00001
Elevation uncertainty (m)	0.5	0.5
Pressure uncertainty (hPa)	NaN	NaN

Table 3.2.—Continued

Parameter (units)	Sample R15MS004	Sample R15TS189
Sample thickness uncertainty (cm)	0.5	0.5
Bulk density uncertainty (g/cm^3)	0.0005	0.001
Shielding factor uncertainty	0.01	0.01
Erosion-rate uncertainty (mm/k.y.)	1	1
^{36}Cl uncertainty (atoms/g)	46,292	14,383
Attenuation length uncertainty (g/cm^2)	10	10
Depth to top of sample uncertainty (cm)	0	0
Year collected uncertainty (C.E.)	0	0
Water content in pores uncertainty (vol. %)	0.01	0.01
Bulk-rock SiO_2 uncertainty (wt. %)	0.233	0.233
Bulk-rock TiO_2 uncertainty (wt. %)	0.018	0.018
Bulk-rock Al_2O_3 uncertainty (wt. %)	0.09	0.09
Bulk-rock Fe_2O_3 uncertainty (wt. %)	0.07	0.07
Bulk-rock MnO uncertainty (wt. %)	0.001	0.001
Bulk-rock MgO uncertainty (wt. %)	0.024	0.024
Bulk-rock CaO uncertainty (wt. %)	0.041	0.041
Bulk-rock Na_2O uncertainty (wt. %)	0.02	0.02
Bulk-rock K_2O uncertainty (wt. %)	0.004	0.004
Bulk-rock P_2O_5 uncertainty (wt. %)	0.002	0.002
Analytical water uncertainty (wt. %)	0.2	0.2
Bulk-rock CO_2 uncertainty (wt. %)	0.2	0.2
Bulk-rock Cl uncertainty (ppm)	7.16	7.16
Bulk-rock B uncertainty (ppm)	5	5
Bulk-rock Sm uncertainty (ppm)	0.18	0.18
Bulk-rock Gd uncertainty (ppm)	0.19	0.19
Bulk-rock U uncertainty (ppm)	0.017	0.017
Bulk-rock Th uncertainty (ppm)	0.05	0.05
Bulk-rock Cr uncertainty (ppm)	0.55	0.55
Bulk-rock Li uncertainty (ppm)	5	5
Target K_2O uncertainty (wt. %)	NaN	0.0012
Target CaO uncertainty (wt. %)	NaN	0.0575
Target TiO_2 uncertainty (wt. %)	NaN	0.0005
Target Fe_2O_3 uncertainty (wt. %)	NaN	0.00215
Target Cl uncertainty (ppm)	NaN	0.2
Covariance	0	0

References Cited

Lal, D., 1991, Cosmic ray labeling of erosion surfaces—In situ nuclide production rates and erosion models: Earth and Planetary Science Letters, v. 104, p. 424–439, https://doi.org/10.1016/0012-821X(91)90220-C.

Marrero, S.M., Phillips, F.M., Borchers, B., Lifton, N., Aumer, R., and Balco, G., 2016, Cosmogenic nuclide systematics and the CRONUScalc program: Quaternary Geochronology, v. 31, p. 160–187, https://doi.org/10.1016/j.quageo.2015.09.005.

Stone, J.O., 2000, Air pressure and cosmogenic isotope production: Journal of Geophysical Research Solid Earth, v. 105, p. 23753–23759, https://doi.org/10.1029/2000JB900181.

Appendix 4. Argon Age Spectra and Isochron Diagrams

Plots in this appendix show the original Ar results of samples dated from the Matan volcanic center. For samples analyzed prior to July 2016, Bodie Hills sanidine (BHs) was used as a fluence monitor with an assumed age of 9.635±0.003 million years old (Ma) that is equivalent to Fish Canyon sanidine (FCs) at 27.642±0.012, such that the FCs/BHs ratio is 2.88340±0.00089. For samples analyzed after July 2016, BHs was used as a fluence monitor with an assumed age of 9.7946±0.0033 Ma (Fleck and others, 2019) that is equivalent to FCs at 28.0985±0.0126 Ma, such that the FCs/BHs ratio is 2.88339±0.00088. Ages in this document have not been recalculated to a common monitor age, but all ages in the report and in table 1 (of the main text) have been recalculated to BHs at 9.7946±0.0033 Ma. Stelten (2021) identifies which monitor age was used in each of the original data files.

References Cited

Fleck, R.J., Calvert, A.T., Coble, M.A., Wooden, J.L., Hodges, K., Hayden, L.A., van Soest, M.C., du Bray, E.A., and John, D.A., 2019, Characterization of the rhyolite of Bodie Hills and $^{40}Ar/^{39}Ar$ intercalibration of Ar mineral standards: Chemical Geology, v. 525, p. 282–302.

Stelten, M.E., 2021, Ar isotope data for volcanic rocks from the northern Harrat Rahat volcanic field and surrounding area, Kingdom of Saudi Arabia: U.S. Geological Survey data release, https://doi.org/10.5066/P92FB6AQ.

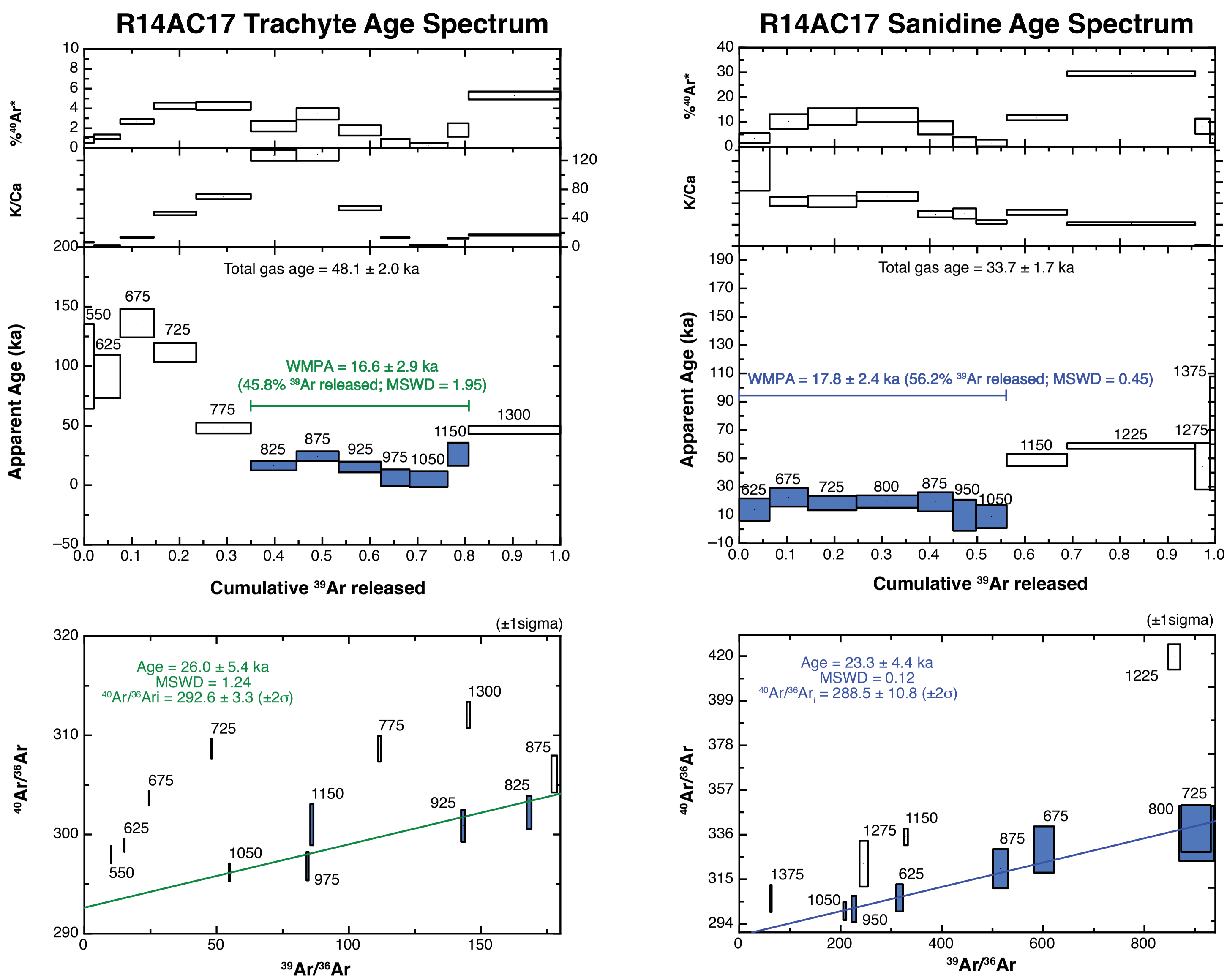

Figure 4.1. Argon age spectra (top plots) and isochron diagrams (bottom plots) for trachyte (left) and sanidine (right) from sample R14AC17 of the trachyte of Dabaa 1 (unit td1). Steps used in calculating the ^{40}Ar/^{39}Ar eruption age for each sample are shown in blue (in the age spectra and isochron diagram). Weighted mean plateau ages (WMPA) for the chosen steps are included in the argon age spectra diagram. Isochron ages for the chosen steps are included in the isochron diagram. See table 1 in the main text for a summary of all ^{40}Ar/^{39}Ar eruption ages and see Stelten (2021) for the full argon dataset. Uncertainties in plotted data points and reported ages are 1σ. Uncertainties for ^{40}Ar/^{36}Ar$_i$ (the isochron intercept) are reported at the 2σ level. Numbers next to the data points correspond to the temperature (in degrees Celsius [°C]) at which the gas was extracted. Preferred age shown in bold font. Colors of the isochron and text are arbitrary. %, percent; ka, kilo-annum; MSWD, mean square of weighted deviates.

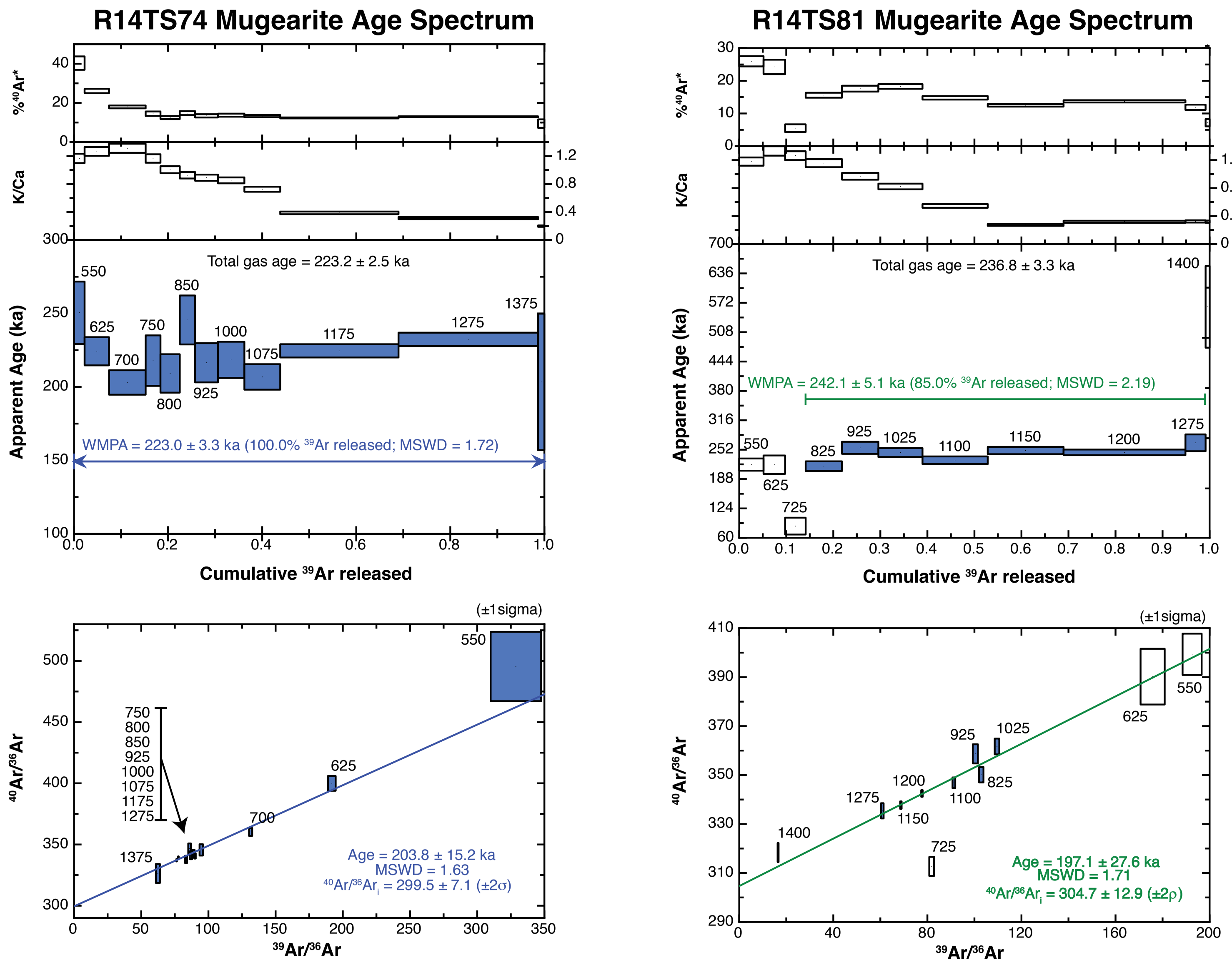

Figure 4.2. Argon age spectra (top plots) and isochron diagrams (bottom plots) for sample R14TS28 of the trachyte of Mouteen (unit tmo; left) and sample R14AC10 of the trachyte of Gura 2 (unit tg2; right). Steps used in calculating the $^{40}Ar/^{39}Ar$ eruption age for each sample are shown in blue (in the age spectra and isochron diagram). Weighted mean plateau ages (WMPA) for the chosen steps are included in the argon age spectra diagram. Isochron ages for the chosen steps are included in the isochron diagram. See table 1 in the main text for a summary of all $^{40}Ar/^{39}Ar$ eruption ages and see Stelten (2021) for the full argon dataset. Uncertainties in plotted data points and reported ages are 1σ. Uncertainties for $^{40}Ar/^{36}Ar_i$ (the isochron intercept) are reported at the 2σ level. Numbers next to the data points correspond to the temperature (in degrees Celsius [°C]) at which the gas was extracted. Preferred age shown in bold font. Colors of the isochron and text are arbitrary. %, percent; ka, kilo-annum; MSWD, mean square of weighted deviates.

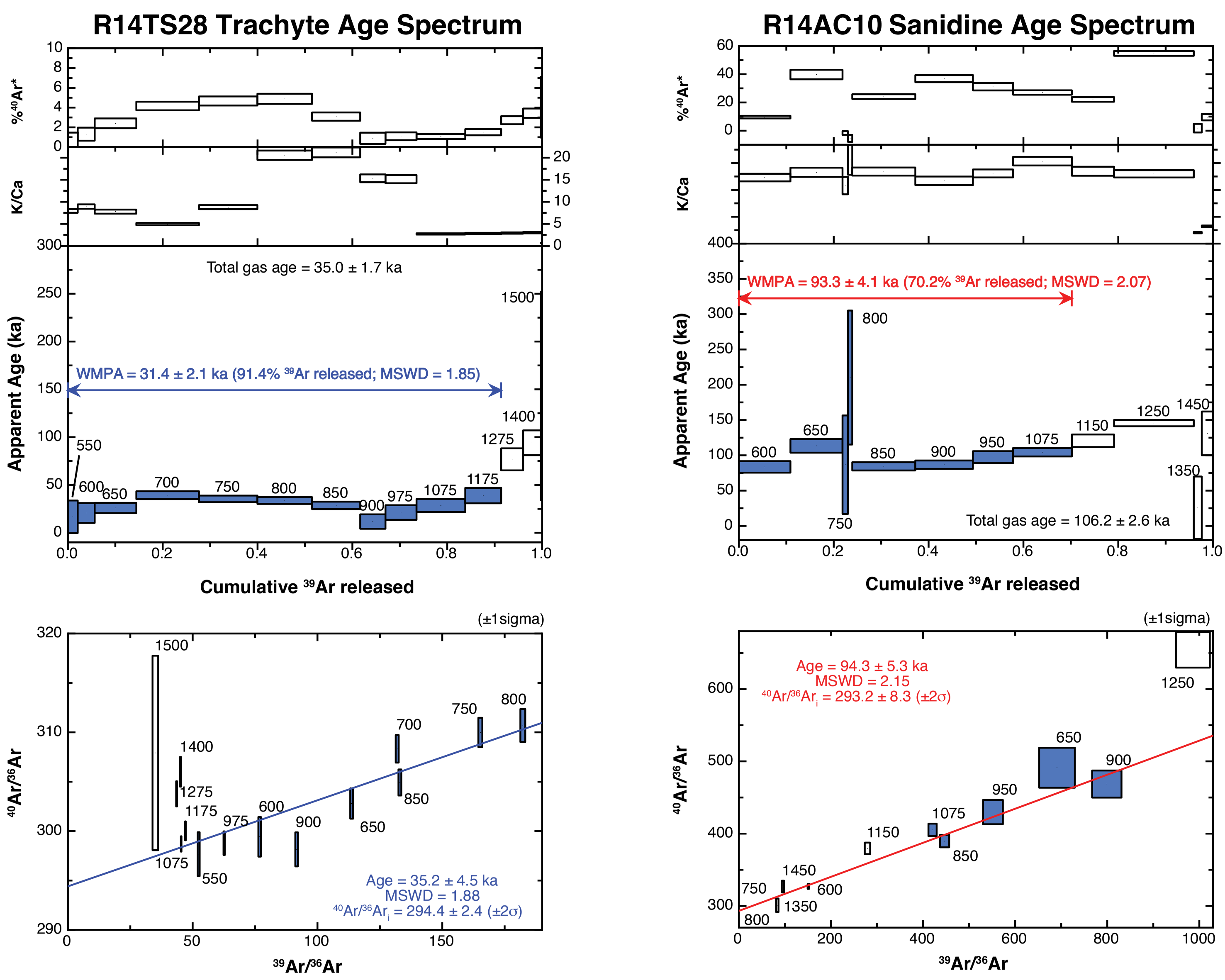

Figure 4.3. Argon age spectra (top plots) and isochron diagrams (bottom) for samples R14AC10 (left) and R14AC86 (right) of the trachyte of Gura 2 (unit tg2). Steps used in calculating the ^{40}Ar/^{39}Ar eruption age for each sample are shown in blue (in the age spectra and isochron diagram). Weighted mean plateau ages (WMPA) for the chosen steps are included in the argon age spectra diagram. Isochron ages for the chosen steps are included in the isochron diagram. See table 1 in the main text for a summary of all ^{40}Ar/^{39}Ar eruption ages and see Stelten (2021) for the full argon dataset. Uncertainties in plotted data points and reported ages are 1σ. Uncertainties for ^{40}Ar/^{36}Ar$_i$ (the isochron intercept) are reported at the 2σ level. Numbers next to the data points correspond to the temperature (in degrees Celsius [°C]) at which the gas was extracted. Preferred age shown in bold font. Colors of the isochron and text are arbitrary. %, percent; ka, kilo-annum; MSWD, mean square of weighted deviates.

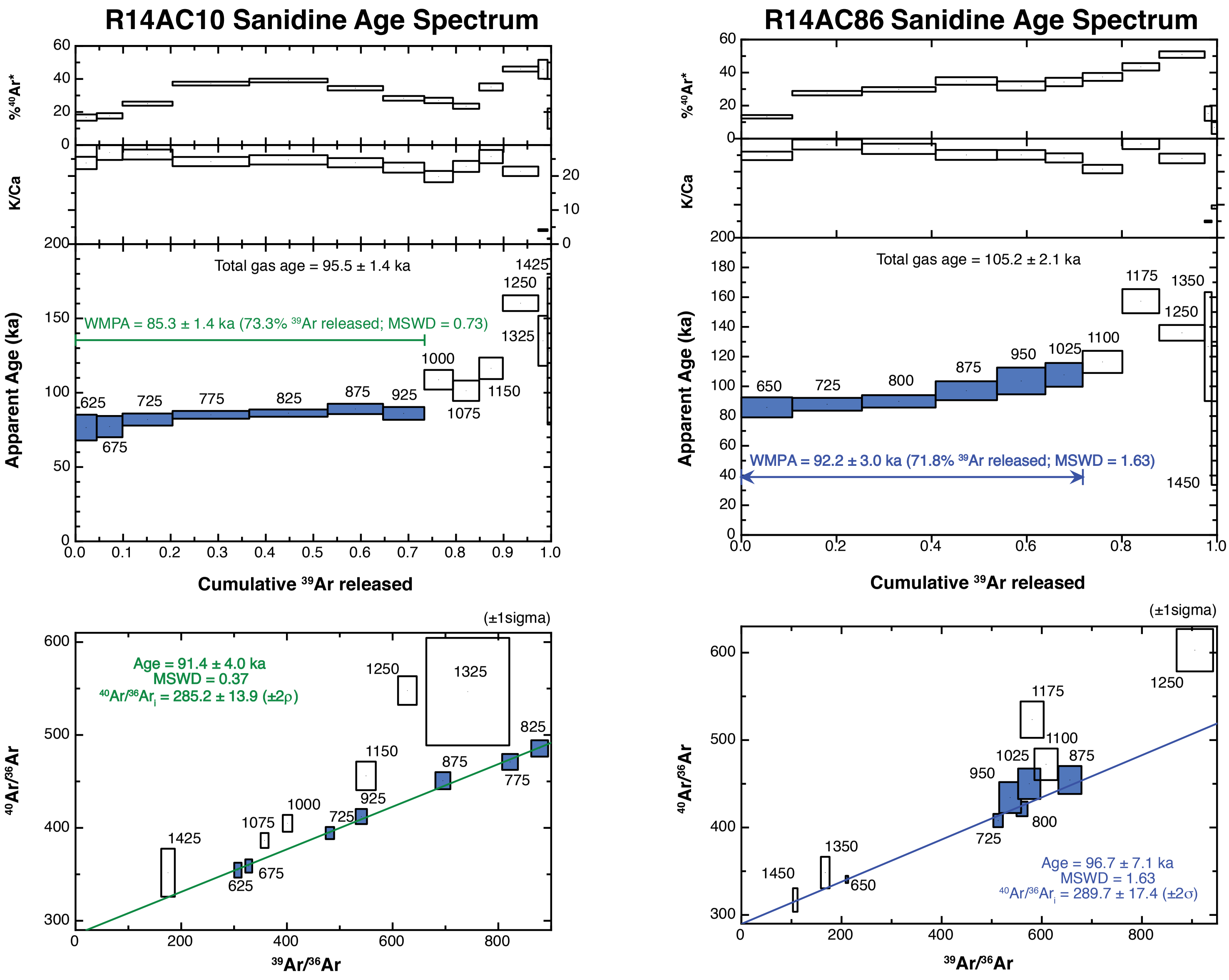

Figure 4.4. Argon age spectra (top plots) and isochron diagrams (bottom plots) for samples R14AC19 (left) and R14AC21 (right) of the mugearite of Dabaa 1 (unit md1). Steps used in calculating the $^{40}Ar/^{39}Ar$ eruption age for each sample are shown in blue (in the age spectra and isochron diagram). Weighted mean plateau ages (WMPA) for the chosen steps are included in the argon age spectra diagram. Isochron ages for the chosen steps are included in the isochron diagram. See table 1 in the main text for a summary of all $^{40}Ar/^{39}Ar$ eruption ages and see Stelten (2021) for the full argon dataset. Uncertainties in plotted data points and reported ages are 1σ. Uncertainties for $^{40}Ar/^{36}Ar_i$ (the isochron intercept) are reported at the 2σ level. Numbers next to the data points correspond to the temperature (in degrees Celsius [°C]) at which the gas was extracted. Preferred age shown in bold font. Colors of the isochron and text are arbitrary. %, percent; ka, kilo-annum; MSWD, mean square of weighted deviates.

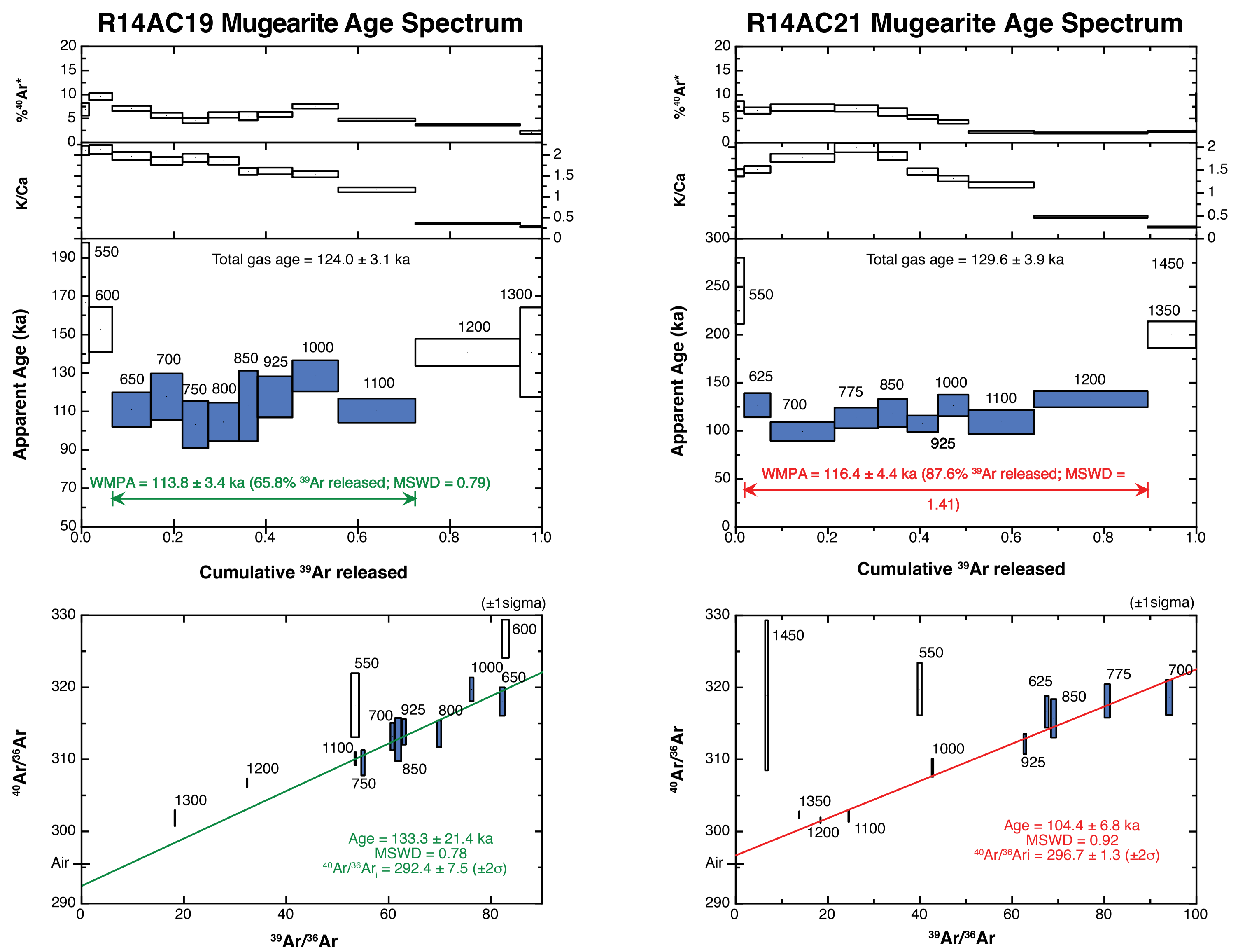

Figure 4.5. Argon age spectra (top plots) and isochron diagrams (bottom plots) for sample R14AC68 of the basalt of Shai'ab Abu Sikhbir (unit bsas; left) and sample R14TS68 of the trachyte of Matan (unit tma; right). Steps used in calculating the ^{40}Ar/^{39}Ar eruption age for each sample are shown in blue (in the age spectra and isochron diagram). Weighted mean plateau ages (WMPA) for the chosen steps are included in the argon age spectra diagram. Isochron ages for the chosen steps are included in the isochron diagram. See table 1 in the main text for a summary of all ^{40}Ar/^{39}Ar eruption ages and see Stelten (2021) for the full argon dataset. Uncertainties in plotted data points and reported ages are 1σ. Uncertainties for ^{40}Ar/^{36}Ar$_i$ (the isochron intercept) are reported at the 2σ level. Numbers next to the data points correspond to the temperature (in degrees Celsius [°C]) at which the gas was extracted. Preferred age shown in bold font. Colors of the isochron and text are arbitrary. %, percent; ka, kilo-annum; MSWD, mean square of weighted deviates.

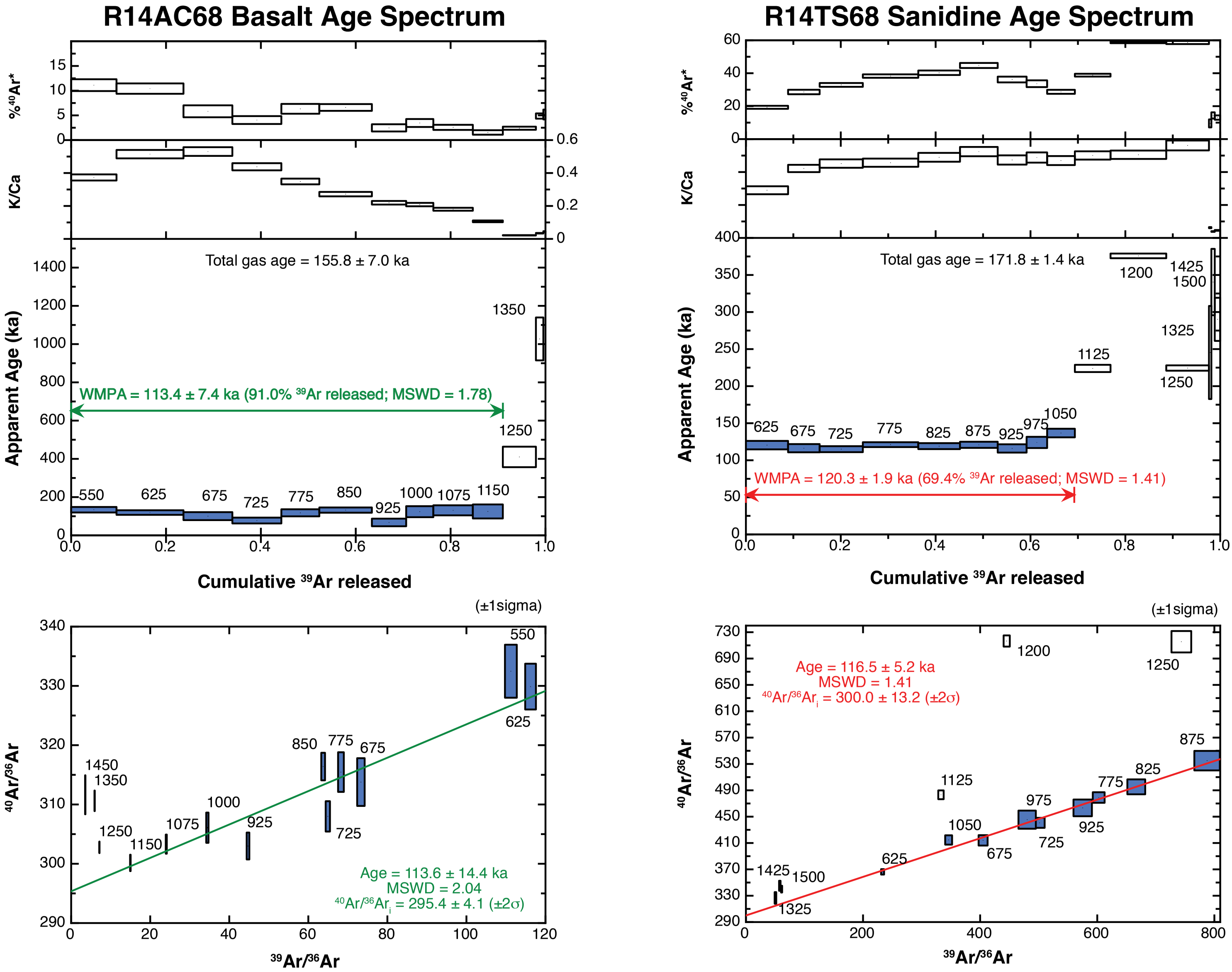

Figure 4.6. Argon age spectra (top plots) and isochron diagrams (bottom plots) for sample R14TS68 of the trachyte of Matan (unit tma; left) and sample R14AC90 of the benmoreite of Gura 2 (unit og2; right). Steps used in calculating the ^{40}Ar/^{39}Ar eruption age for each sample are shown in blue (in the age spectra and isochron diagram). Weighted mean plateau ages (WMPA) for the chosen steps are included in the argon age spectra diagram. Isochron ages for the chosen steps are included in the isochron diagram. See table 1 in the main text for a summary of all ^{40}Ar/^{39}Ar eruption ages and see Stelten (2021) for the full argon dataset. Uncertainties in plotted data points and reported ages are 1σ. Uncertainties for ^{40}Ar/^{36}Ar$_i$ (the isochron intercept) are reported at the 2σ level. Numbers next to the data points correspond to the temperature (in degrees Celsius [°C]) at which the gas was extracted. Preferred age shown in bold font. Colors of the isochron and text are arbitrary. %, percent; ka, kilo-annum; MSWD, mean square of weighted deviates.

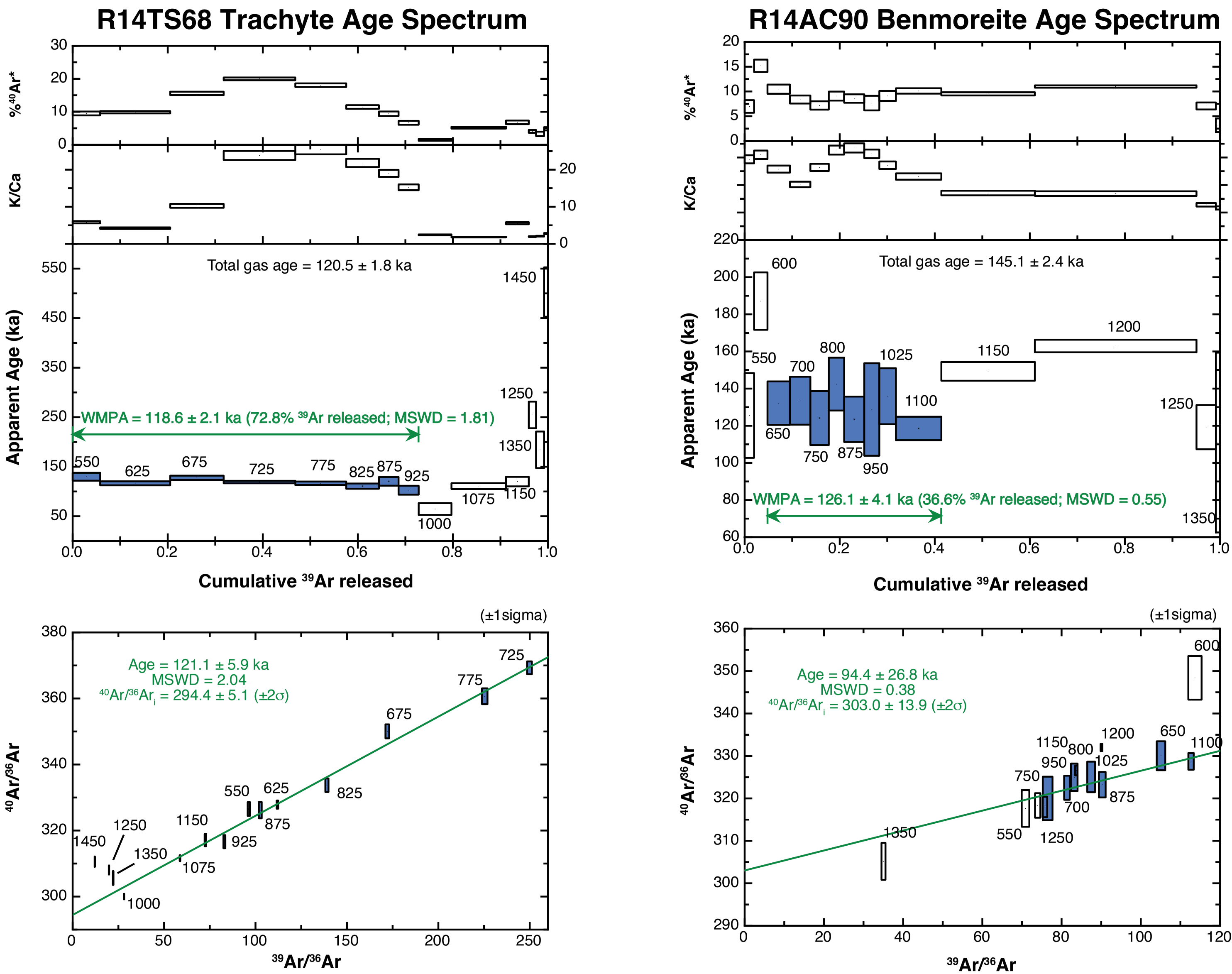

Figure 4.7. Argon age spectra (top plots) and isochron diagrams (bottom plots) for sample R14AC69 of the basalt of Abu Rimthah (unit bar; left) and sample R15MS010 of the trachyte of Gura 3 (unit tg3; right). Steps used in calculating the ^{40}Ar/^{39}Ar eruption age for each sample are shown in blue (in the age spectra and isochron diagram). Weighted mean plateau ages (WMPA) for the chosen steps are included in the argon age spectra diagram. Isochron ages for the chosen steps are included in the isochron diagram. See table 1 in the main text for a summary of all ^{40}Ar/^{39}Ar eruption ages and see Stelten (2021) for the full argon dataset. Uncertainties in plotted data points and reported ages are 1σ. Uncertainties for ^{40}Ar/^{36}Ar$_i$ (the isochron intercept) are reported at the 2σ level. Numbers next to the data points correspond to the temperature (in degrees Celsius [°C]) at which the gas was extracted. Preferred age shown in bold font. Colors of the isochron and text are arbitrary. %, percent; ka, kilo-annum; MSWD, mean square of weighted deviates.

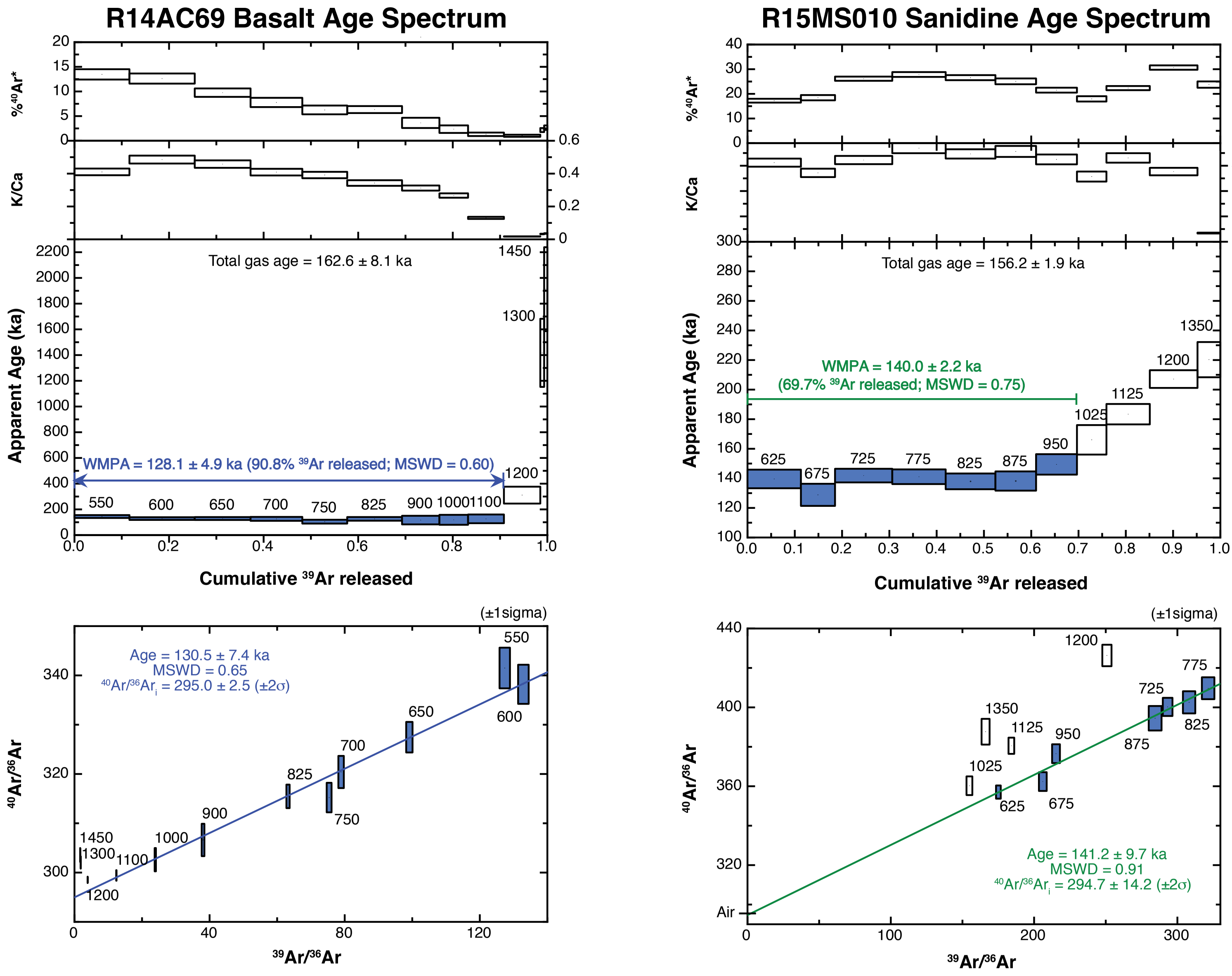

Figure 4.8. Argon age spectra (top plots) and isochron diagrams (bottom plots) for sample R14TS131 of the mugearite of Matan (unit mma; left) and sample R14TS33 of the basalt of Sha'ib Iskabah (unit bsi; right). Steps used in calculating the ^{40}Ar/^{39}Ar eruption age for each sample are shown in blue (in the age spectra and isochron diagram). Weighted mean plateau ages (WMPA) for the chosen steps are included in the argon age spectra diagram. Isochron ages for the chosen steps are included in the isochron diagram. See table 1 in the main text for a summary of all ^{40}Ar/^{39}Ar eruption ages and see Stelten (2021) for the full argon dataset. Uncertainties in plotted data points and reported ages are 1σ. Uncertainties for ^{40}Ar/^{36}Ar$_i$ (the isochron intercept) are reported at the 2σ level. Numbers next to the data points correspond to the temperature (in degrees Celsius [°C]) at which the gas was extracted. Preferred age shown in bold font. Colors of the isochron and text are arbitrary. %, percent; ka, kilo-annum; MSWD, mean square of weighted deviates.

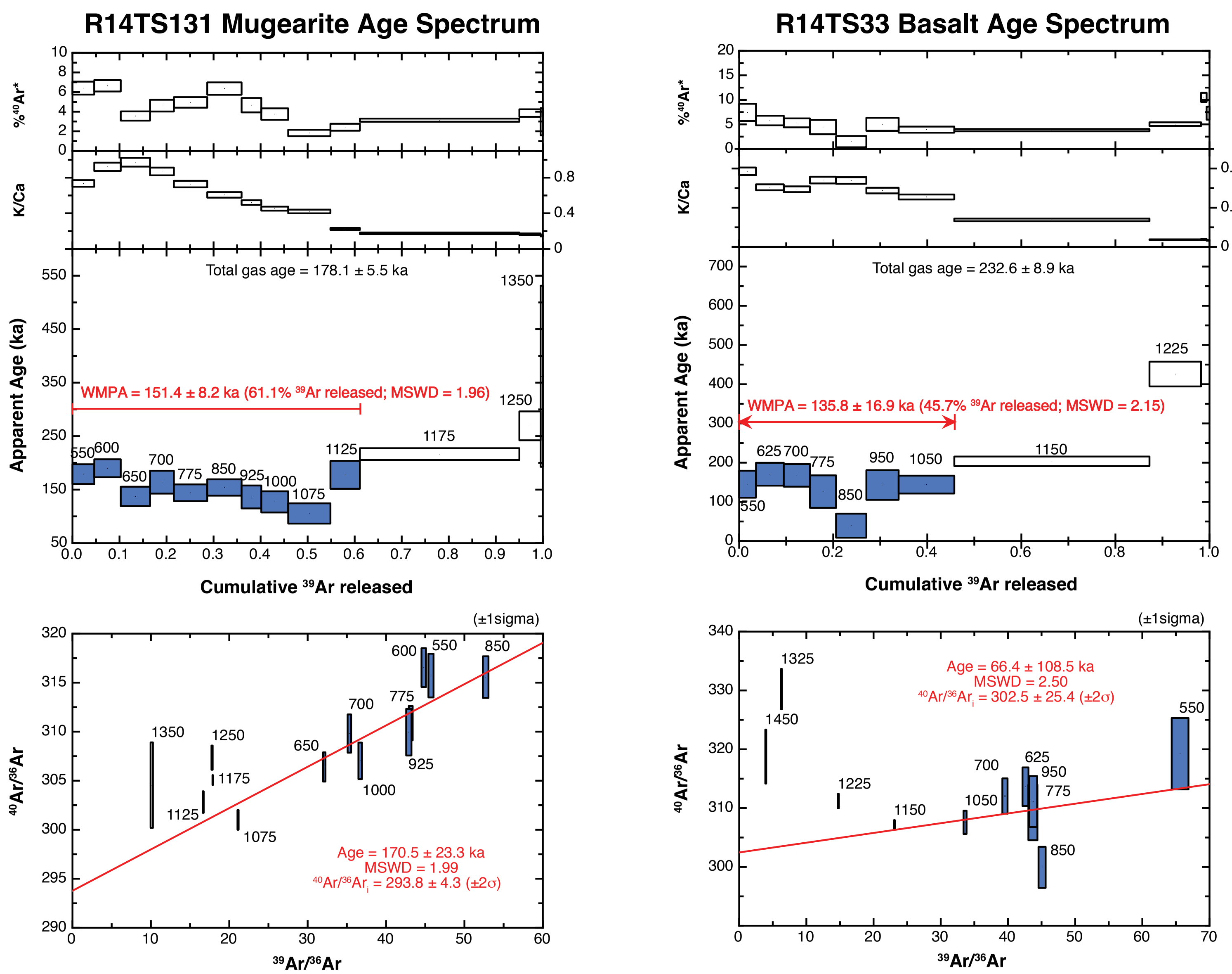

Figure 4.9. Argon age spectra (top plots) and isochron diagrams (bottom plots) for sample R14TS33 of the basalt of Sha'ib Iskabah (unit bsi; left) and sample R14AC96 of the mugearite of Al Mulaysa (unit mmu; right). Steps used in calculating the ^{40}Ar/^{39}Ar eruption age for each sample are shown in blue (in the age spectra and isochron diagram). Weighted mean plateau ages (WMPA) for the chosen steps are included in the argon age spectra diagram. Isochron ages for the chosen steps are included in the isochron diagram. See table 1 in the main text for a summary of all ^{40}Ar/^{39}Ar eruption ages and see Stelten (2021) for the full argon dataset. Uncertainties in plotted data points and reported ages are 1σ. Uncertainties for ^{40}Ar/^{36}Ar$_i$ (the isochron intercept) are reported at the 2σ level. Numbers next to the data points correspond to the temperature (in degrees Celsius [°C]) at which the gas was extracted. Preferred age shown in bold font. Colors of the isochron and text are arbitrary. %, percent; ka, kilo-annum; MSWD, mean square of weighted deviates.

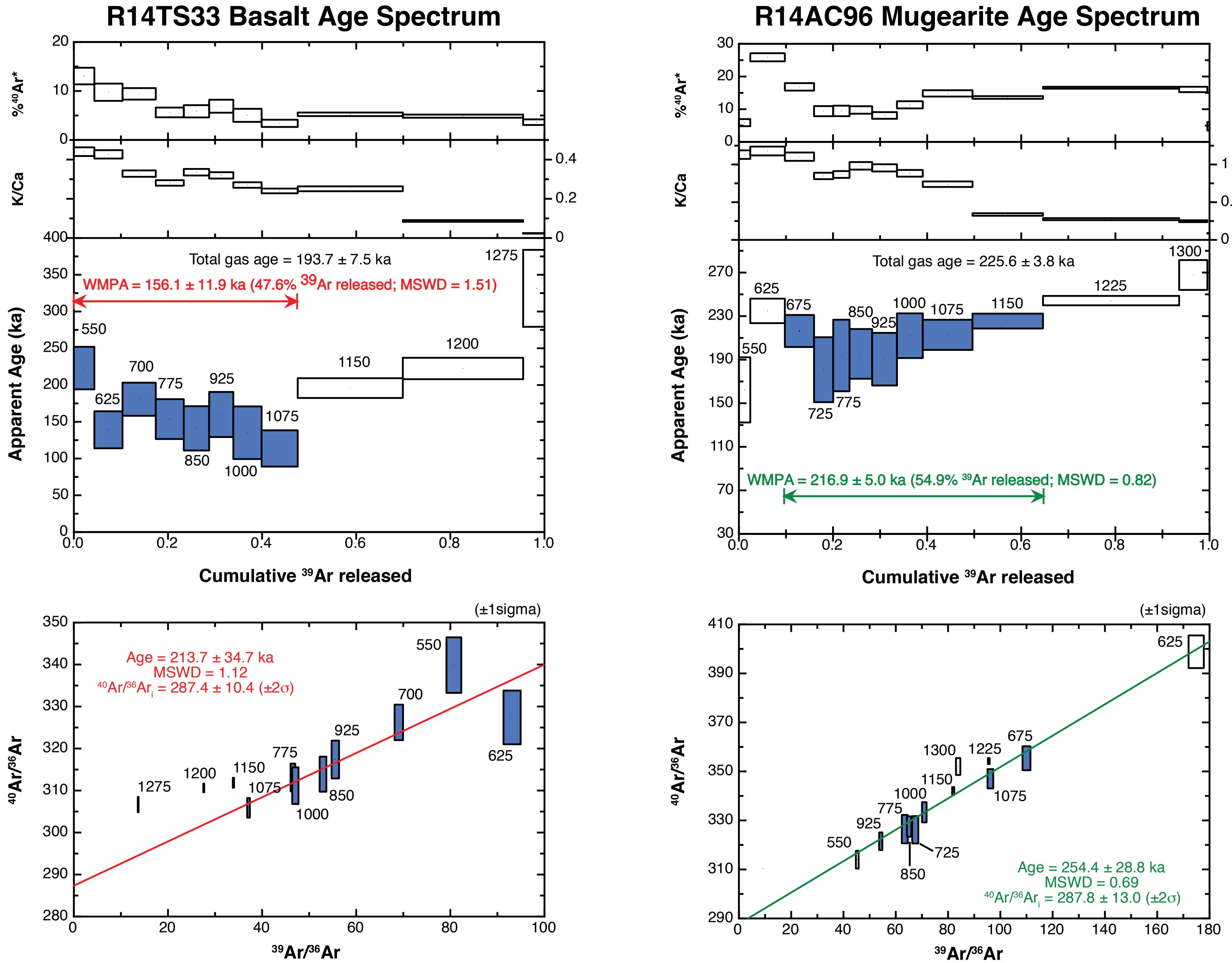

Figure 4.10. Argon age spectra (top plots) and isochron diagrams (bottom plots) for samples R14TS74 (left) and R14TS81 (right) of the mugearite of Al Mulaysa (unit mmu). Steps used in calculating the ^{40}Ar/^{39}Ar eruption age for each sample are shown in blue (in the age spectra and isochron diagram). Weighted mean plateau ages (WMPA) for the chosen steps are included in the argon age spectra diagram. Isochron ages for the chosen steps are included in the isochron diagram. See table 1 in the main text for a summary of all ^{40}Ar/^{39}Ar eruption ages and see Stelten (2021) for the full argon dataset. Uncertainties in plotted data points and reported ages are 1σ. Uncertainties for ^{40}Ar/^{36}Ar$_i$ (the isochron intercept) are reported at the 2σ level. Numbers next to the data points correspond to the temperature (in degrees Celsius [°C]) at which the gas was extracted. Preferred age shown in bold font. Colors of the isochron and text are arbitrary. %, percent; ka, kilo-annum; MSWD, mean square of weighted deviates.

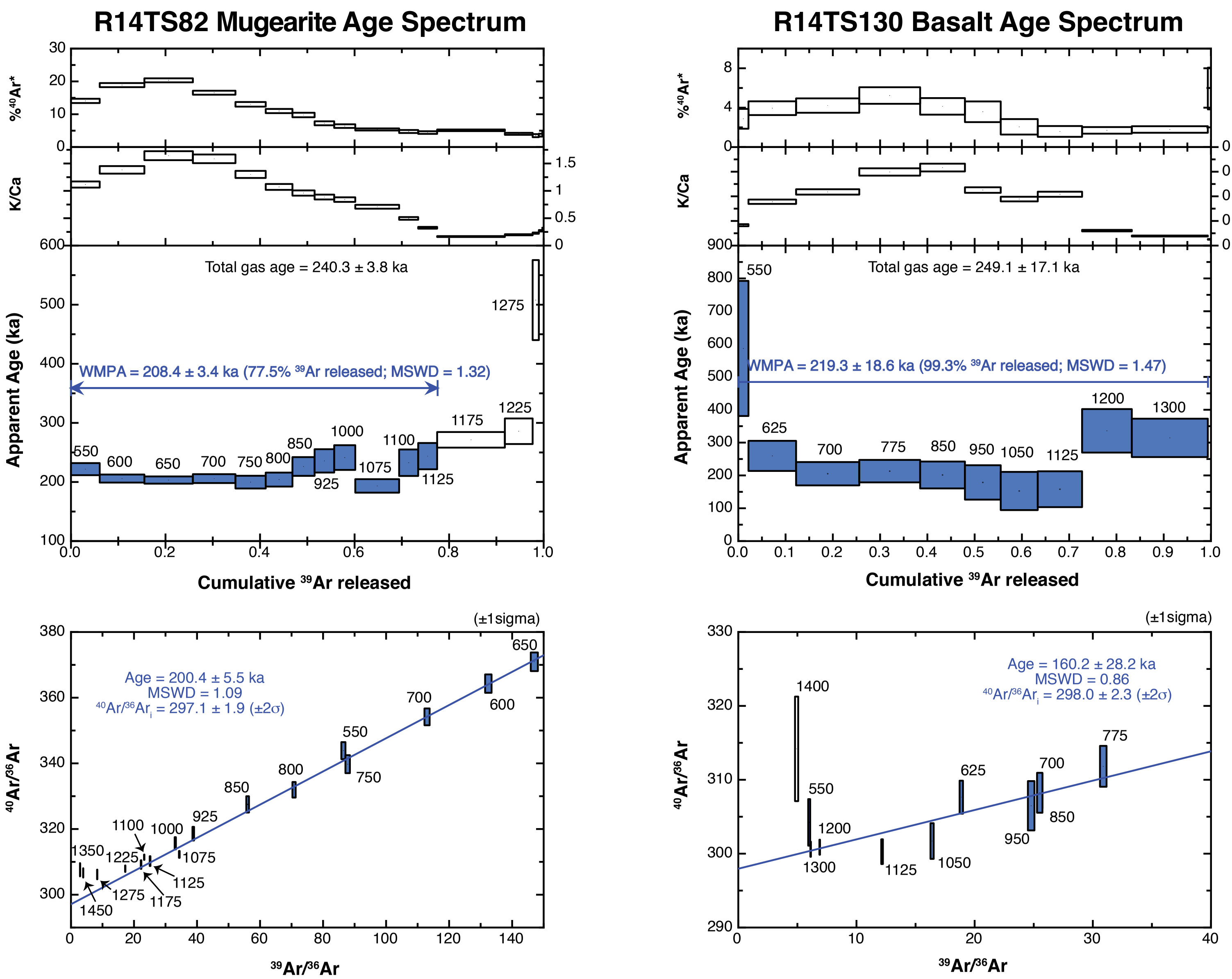

Figure 4.11. Argon age spectra (top plots) and isochron diagrams (bottom plots) for sample R14TS82 of the mugearite of Al Mulaysa (unit mmu; left) and sample R14TS130 of the basalt of Ad Darah (unit bda; right). Steps used in calculating the $^{40}Ar/^{39}Ar$ eruption age for each sample are shown in blue (in the age spectra and isochron diagram). Weighted mean plateau ages (WMPA) for the chosen steps are included in the argon age spectra diagram. Isochron ages for the chosen steps are included in the isochron diagram. See table 1 in the main text for a summary of all $^{40}Ar/^{39}Ar$ eruption ages and see Stelten (2021) for the full argon dataset. Uncertainties in plotted data points and reported ages are 1σ. Uncertainties for $^{40}Ar/^{36}Ar_i$ (the isochron intercept) are reported at the 2σ level. Numbers next to the data points correspond to the temperature (in degrees Celsius [°C]) at which the gas was extracted. Preferred age shown in bold font. Colors of the isochron and text are arbitrary. %, percent; ka, kilo-annum; MSWD, mean square of weighted deviates.

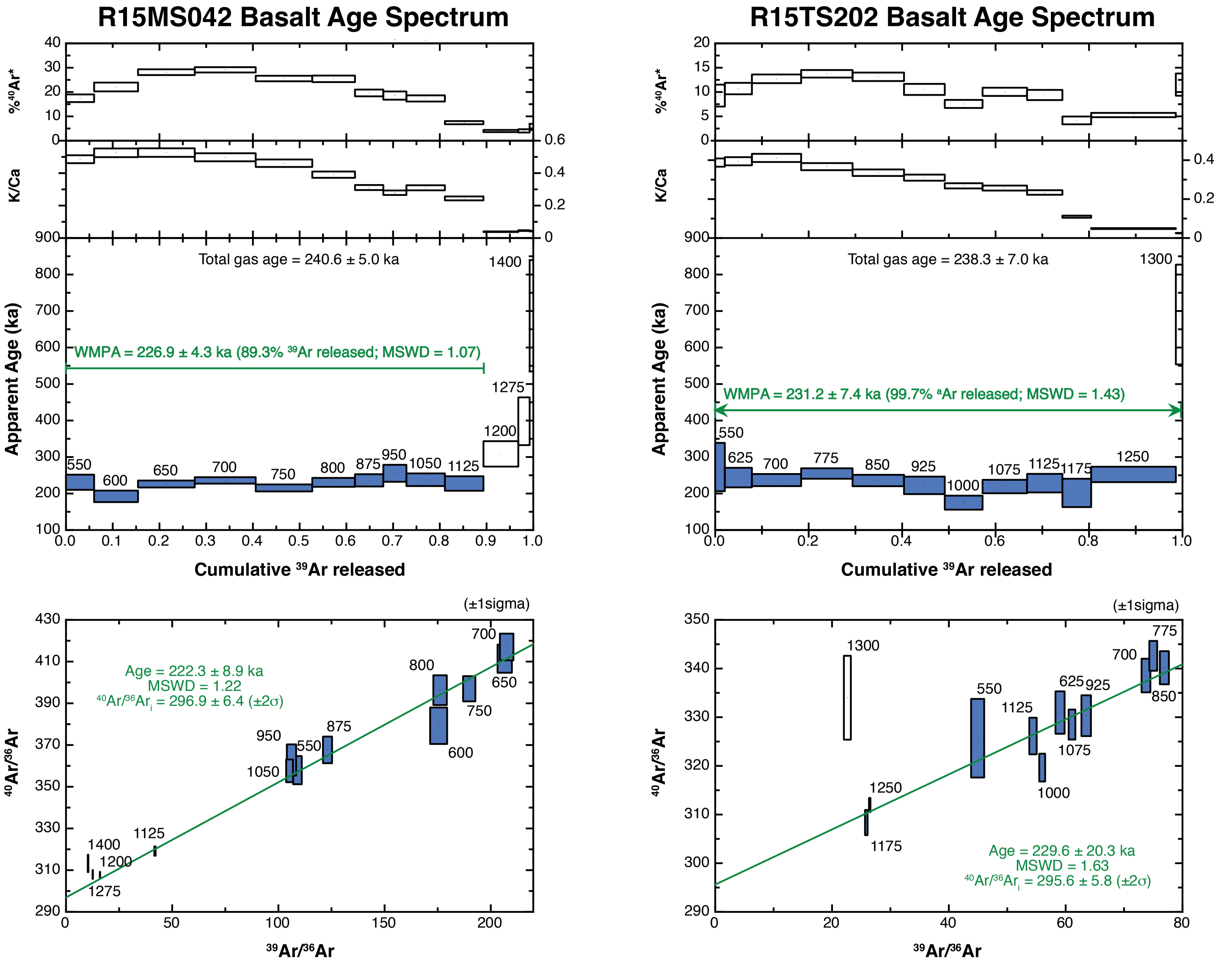

Figure 4.12. Argon age spectra (top plots) and isochron diagrams (bottom plots) for sample R15MS042 of the basalt of Al Malsaa 1 (unit bm1; left) and sample R15TS202 of the basalt of Sha'ib Hayaya (unit bhy; right). Steps used in calculating the $^{40}Ar/^{39}Ar$ eruption age for each sample are shown in blue (in the age spectra and isochron diagram). Weighted mean plateau ages (WMPA) for the chosen steps are included in the argon age spectra diagram. Isochron ages for the chosen steps are included in the isochron diagram. See table 1 in the main text for a summary of all $^{40}Ar/^{39}Ar$ eruption ages and see Stelten (2021) for the full argon dataset. Uncertainties in plotted data points and reported ages are 1σ. Uncertainties for $^{40}Ar/^{36}Ar_i$ (the isochron intercept) are reported at the 2σ level. Numbers next to the data points correspond to the temperature (in degrees Celsius [°C]) at which the gas was extracted. Preferred age shown in bold font. Colors of the isochron and text are arbitrary. %, percent; ka, kilo-annum; MSWD, mean square of weighted deviates.

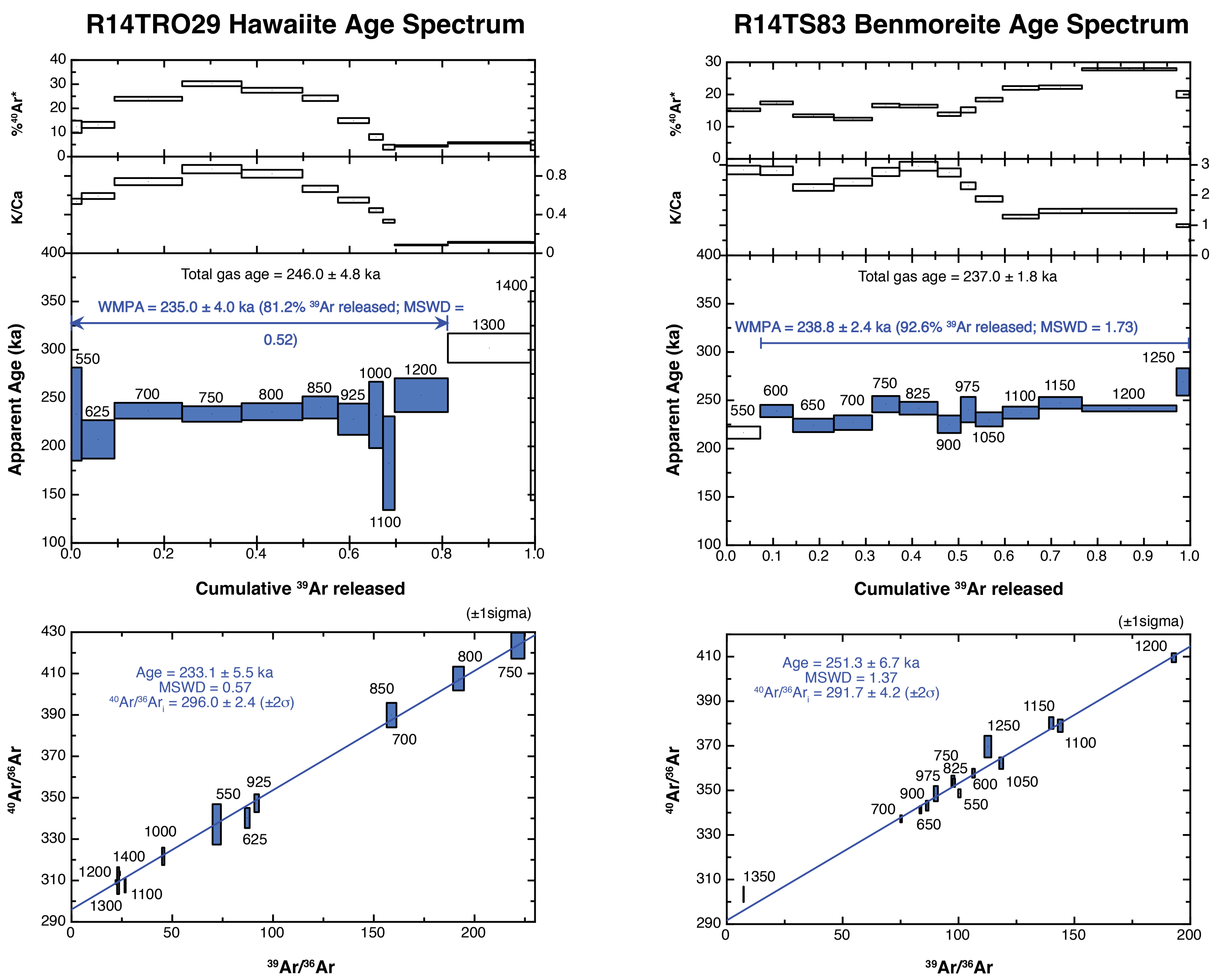
R14TRO29 Hawaiite Age Spectrum

R14TS83 Benmoreite Age Spectrum

Figure 4.13. Argon age spectra (top plots) and isochron diagrams (bottom plots) for sample R14TRO29 of the hawaiite of Mouteen (unit hmo; left) and sample R14TS83 of the benmoreite of Al Bayadah (unit oba; right). Steps used in calculating the ^{40}Ar/^{39}Ar eruption age for each sample are shown in blue (in the age spectra and isochron diagram). Weighted mean plateau ages (WMPA) for the chosen steps are included in the argon age spectra diagram. Isochron ages for the chosen steps are included in the isochron diagram. See table 1 in the main text for a summary of all ^{40}Ar/^{39}Ar eruption ages and see Stelten (2021) for the full argon dataset. Uncertainties in plotted data points and reported ages are 1σ. Uncertainties for ^{40}Ar/^{36}Ar$_i$ (the isochron intercept) are reported at the 2σ level. Numbers next to the data points correspond to the temperature (in degrees Celsius [°C]) at which the gas was extracted. Preferred age shown in bold font. Colors of the isochron and text are arbitrary. %, percent; ka, kilo-annum; MSWD, mean square of weighted deviates.

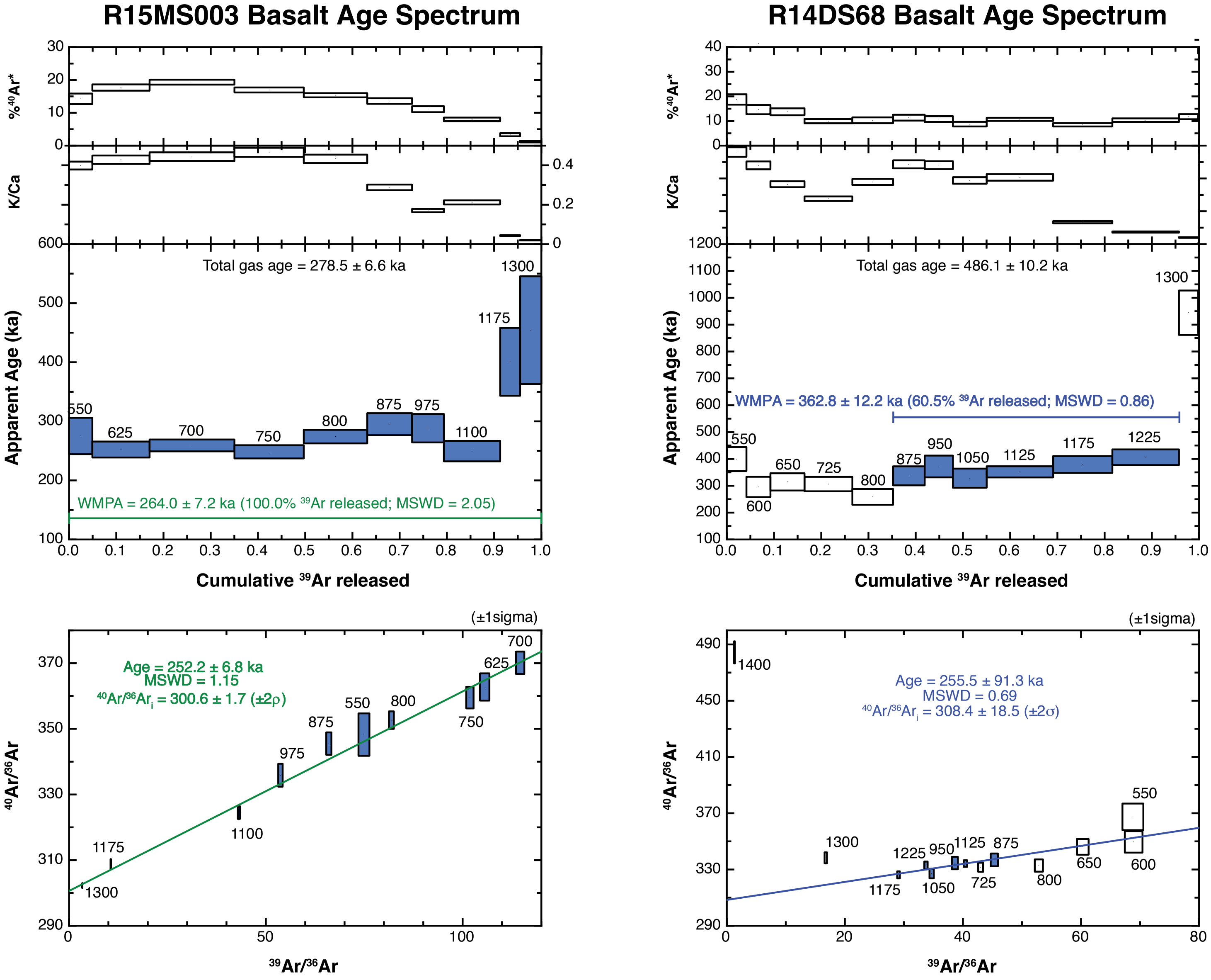

Figure 4.14. Argon age spectra (top plots) and isochron diagrams (bottom plots) for sample R15MS003 of the basalt of Amlit 1 (unit bam1; left) and sample R14DS68 of the basalt of Upper Abu Rimthah (unit burr; right). Steps used in calculating the $^{40}Ar/^{39}Ar$ eruption age for each sample are shown in blue (in the age spectra and isochron diagram). Weighted mean plateau ages (WMPA) for the chosen steps are included in the argon age spectra diagram. Isochron ages for the chosen steps are included in the isochron diagram. See table 1 in the main text for a summary of all $^{40}Ar/^{39}Ar$ eruption ages and see Stelten (2021) for the full argon dataset. Uncertainties in plotted data points and reported ages are 1σ. Uncertainties for $^{40}Ar/^{36}Ar_i$ (the isochron intercept) are reported at the 2σ level. Numbers next to the data points correspond to the temperature (in degrees Celsius [°C]) at which the gas was extracted. Preferred age shown in bold font. Colors of the isochron and text are arbitrary. %, percent; ka, kilo-annum; MSWD, mean square of weighted deviates.

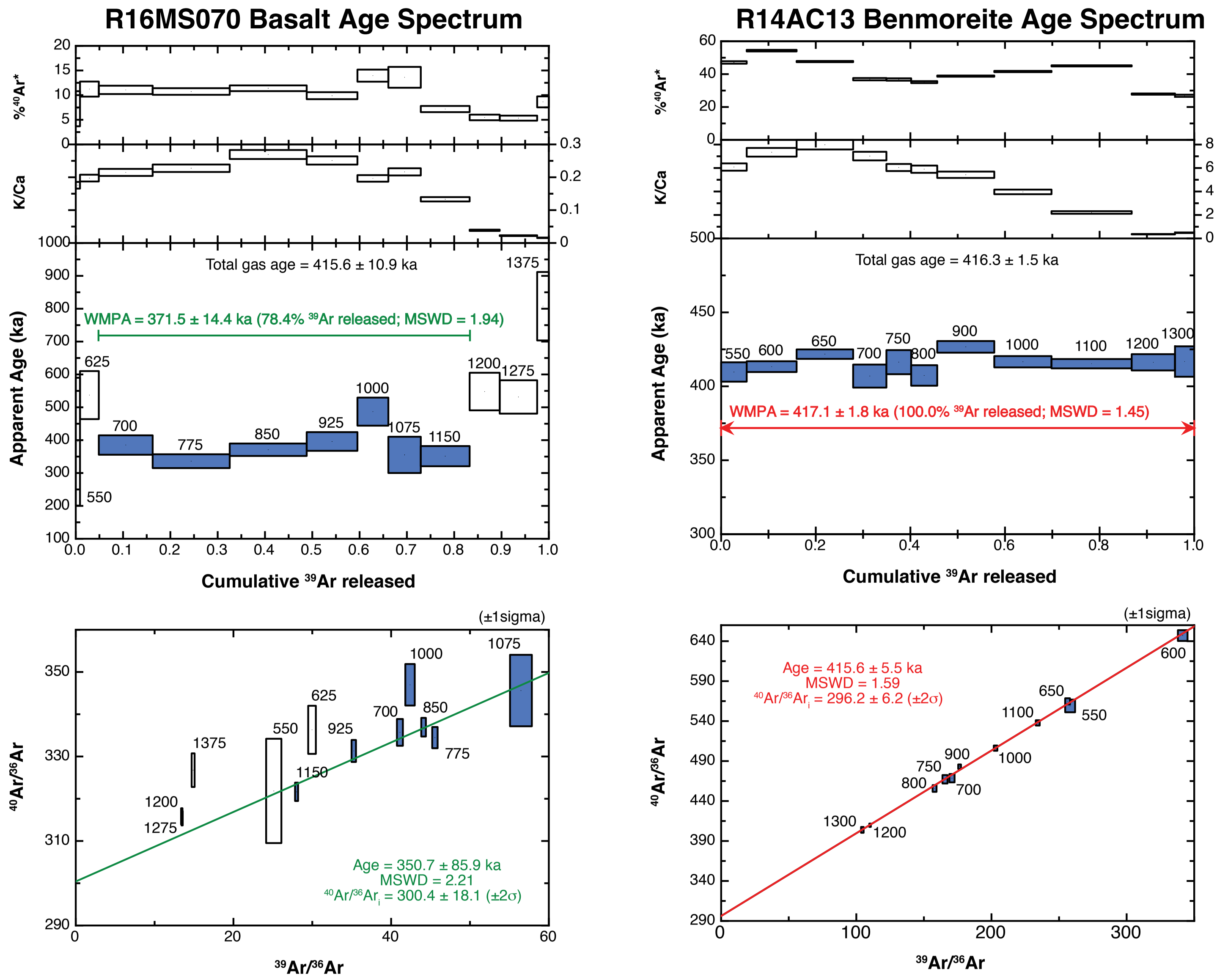

Figure 4.15. Argon age spectra (top plots) and isochron diagrams (bottom plots) for sample R16MS070 of the basalt of Upper Abu Rimthah (unit burr; left) and sample R14AC13 of the benmoreite of Um Junb (unit oju; right). Steps used in calculating the $^{40}Ar/^{39}Ar$ eruption age for each sample are shown in blue (in the age spectra and isochron diagram). Weighted mean plateau ages (WMPA) for the chosen steps are included in the argon age spectra diagram. Isochron ages for the chosen steps are included in the isochron diagram. See table 1 in the main text for a summary of all $^{40}Ar/^{39}Ar$ eruption ages and see Stelten (2021) for the full argon dataset. Uncertainties in plotted data points and reported ages are 1σ. Uncertainties for $^{40}Ar/^{36}Ar_i$ (the isochron intercept) are reported at the 2σ level. Numbers next to the data points correspond to the temperature (in degrees Celsius [°C]) at which the gas was extracted. Preferred age shown in bold font. Colors of the isochron and text are arbitrary. %, percent; ka, kilo-annum; MSWD, mean square of weighted deviates.

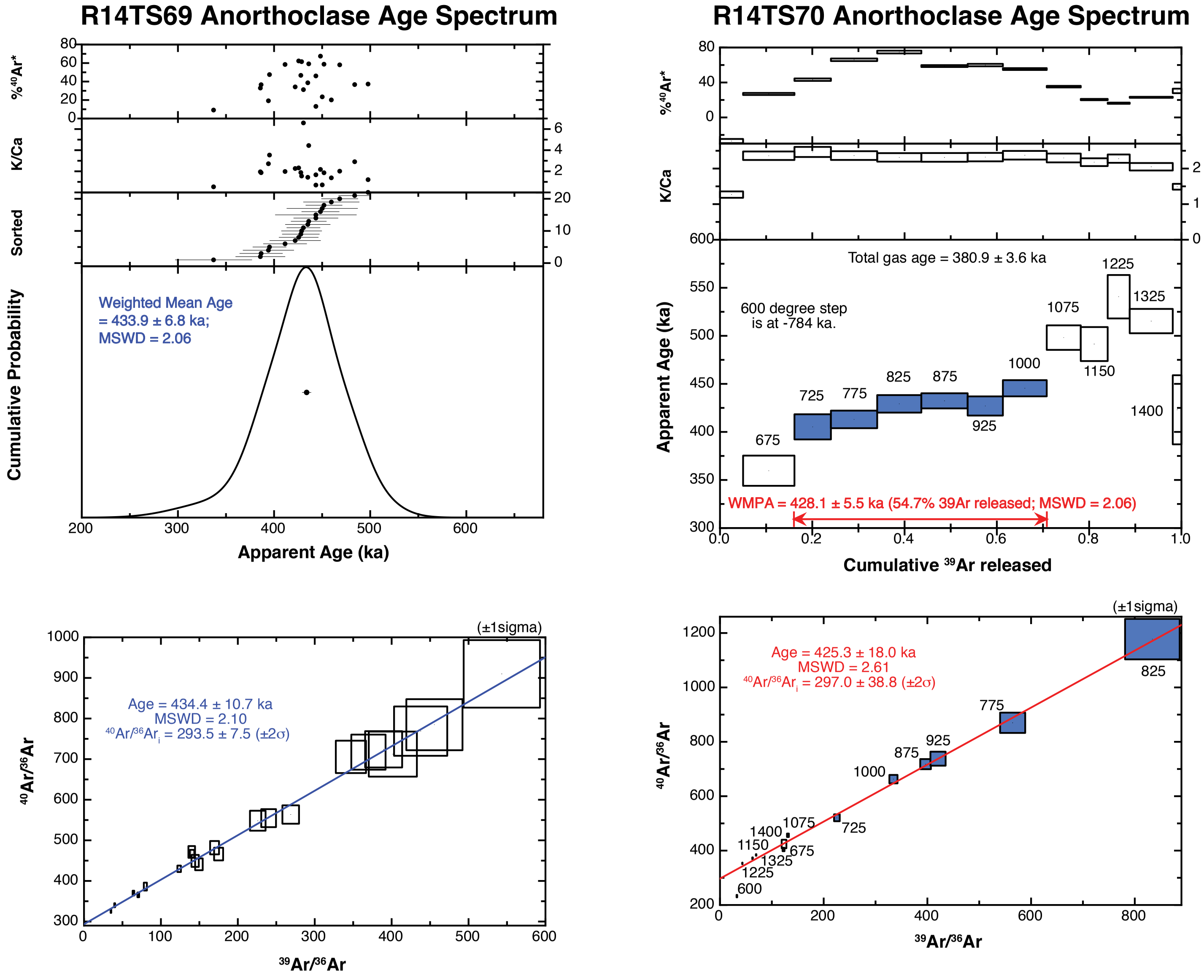

Figure 4.16. Left, single crystal total fusion data for sample R14TS69 of the benmoreite of Um Junb (unit oju). The weighted mean age and isochron age for sample R14TS69 using all single crystal total fusion analyses are provided below. Right, argon age spectra (top) and isochron diagram (bottom) for sample R14TS70 of unit oju. Steps used in calculating the ^{40}Ar/^{39}Ar eruption age for sample R14TS70 are shown in blue (in the age spectra and isochron diagram). The weighted mean plateau age (WMPA) for the chosen steps from sample R14TS70 is included in the argon age spectra diagram. The isochron age for the chosen steps from sample R14TS70 is included in the isochron diagram. See table 1 in the main text for a summary of all ^{40}Ar/^{39}Ar eruption ages and see Stelten (2021) for the full argon dataset. Uncertainties in plotted data points and reported ages are 1σ. Uncertainties for ^{40}Ar/^{36}Ar$_i$ (the isochron intercept) are reported at the 2σ level. Numbers next to the data points correspond to the temperature (in degrees Celsius [°C]) at which the gas was extracted. Preferred age in bold font. Colors of the isochron and text are arbitrary. %, percent; ka, kilo-annum; MSWD, mean square of weighted deviates.

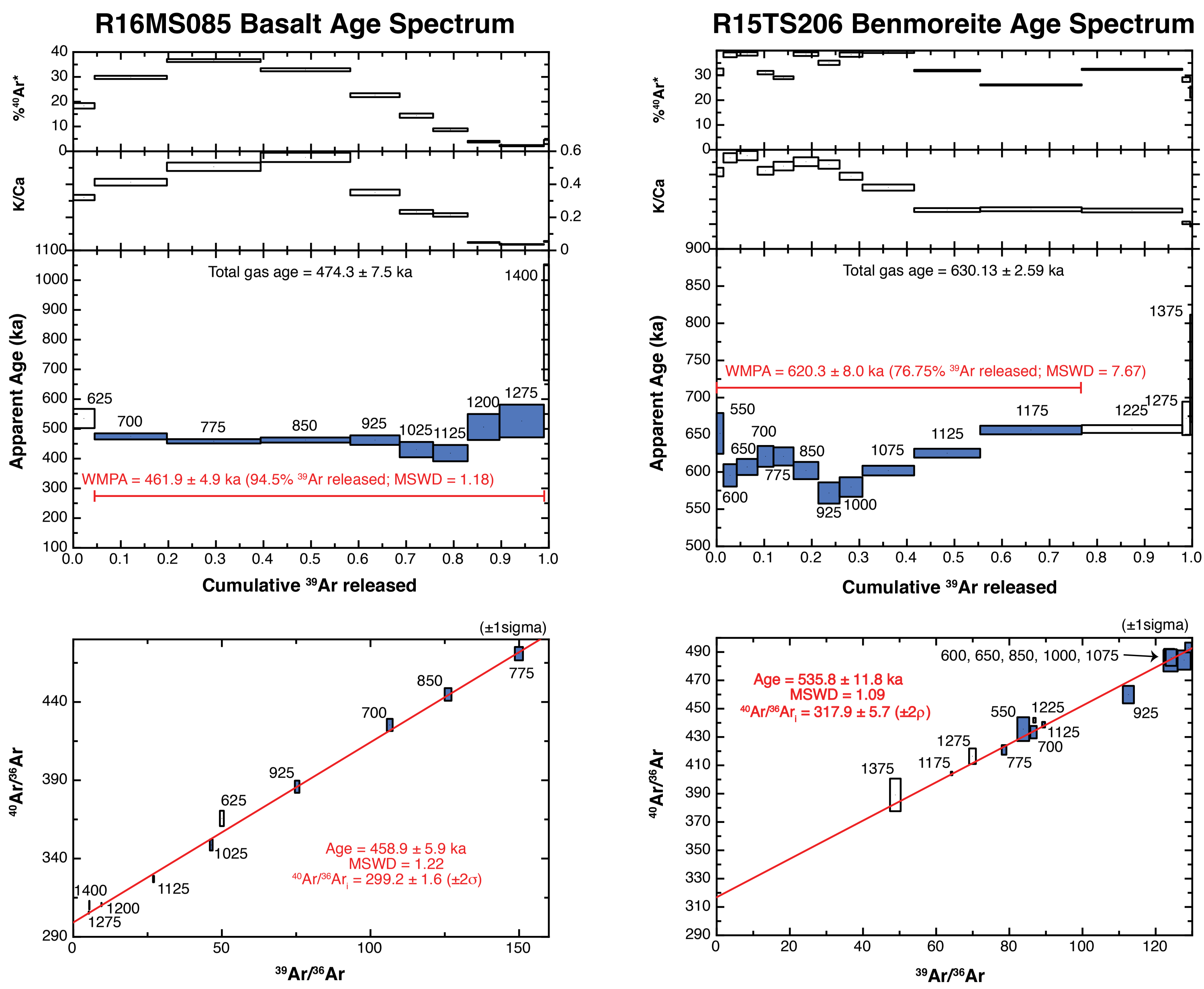

Figure 4.17. Argon age spectra (top plots) and isochron diagrams (bottom plots) for sample R16MS085 of the basalt of Sha'ib Si'ayd (unit bss; left) and sample R15TS206 of the benmoreite of As Sabah (unit osb; right). Steps used in calculating the $^{40}Ar/^{39}Ar$ eruption age for each sample are shown in blue (in the age spectra and isochron diagram). Weighted mean plateau ages (WMPA) for the chosen steps are included in the argon age spectra diagram. Isochron ages for the chosen steps are included in the isochron diagram. See table 1 in the main text for a summary of all $^{40}Ar/^{39}Ar$ eruption ages and see Stelten (2021) for the full argon dataset. Uncertainties in plotted data points and reported ages are 1σ. Uncertainties for $^{40}Ar/^{36}Ar_i$ (the isochron intercept) are reported at the 2σ level. Numbers next to the data points correspond to the temperature (in degrees Celsius [°C]) at which the gas was extracted. Preferred age shown in bold font. Colors of the isochron and text are arbitrary. %, percent; ka, kilo-annum; MSWD, mean square of weighted deviates.

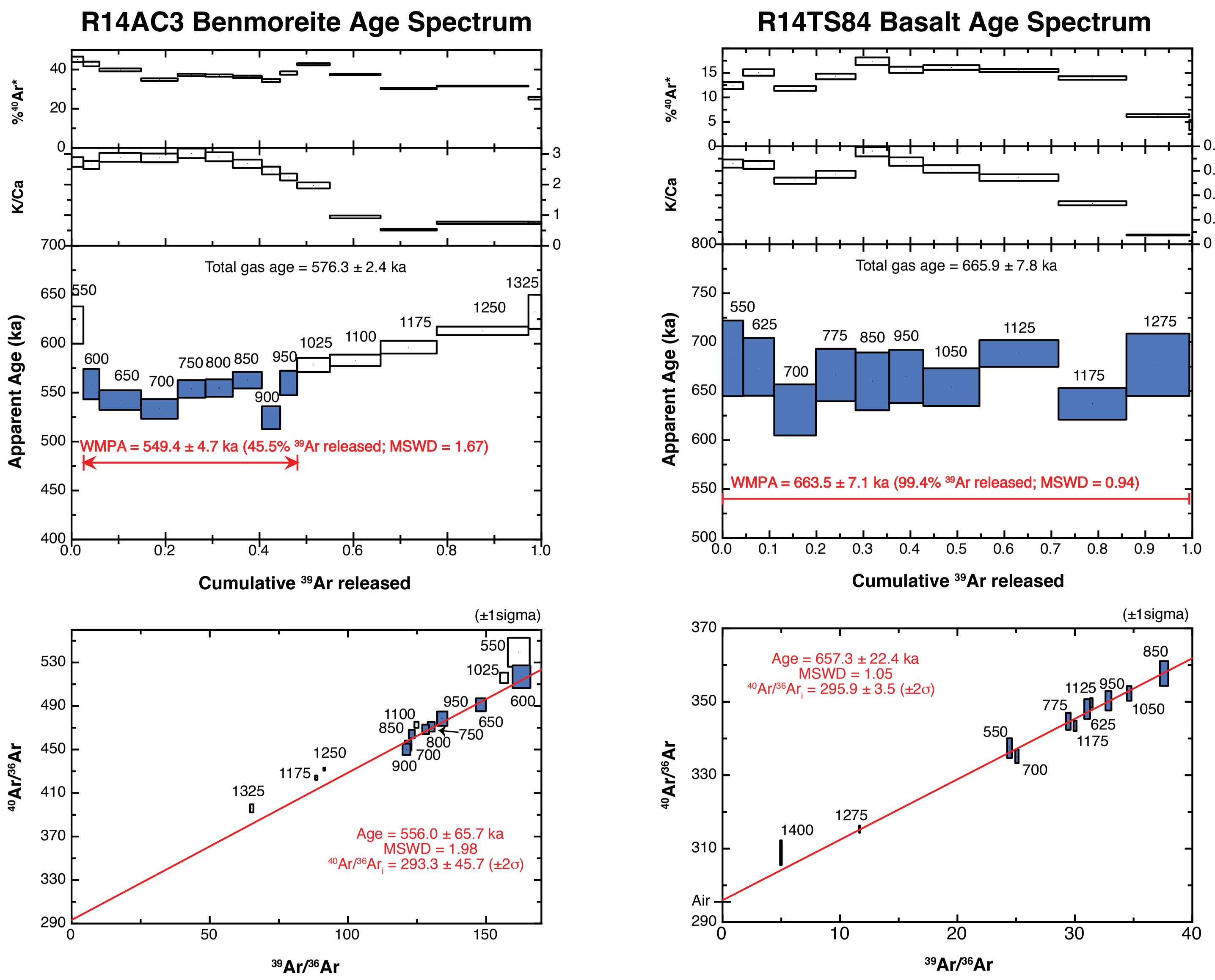

Figure 4.18. Argon age spectra (top plots) and isochron diagrams (bottom plots) for sample R14AC3 of the benmoreite of Gura 3 (unit og3; left) and sample R14TS84 of the basalt of Al Bayadah (unit bba; right). Steps used in calculating the $^{40}Ar/^{39}Ar$ eruption age for each sample are shown in blue (in the age spectra and isochron diagram). Weighted mean plateau ages (WMPA) for the chosen steps are included in the argon age spectra diagram. Isochron ages for the chosen steps are included in the isochron diagram. See table 1 in the main text for a summary of all $^{40}Ar/^{39}Ar$ eruption ages and see Stelten (2021) for the full argon dataset. Uncertainties in plotted data points and reported ages are 1σ. Uncertainties for $^{40}Ar/^{36}Ar_i$ (the isochron intercept) are reported at the 2σ level. Numbers next to the data points correspond to the temperature (in degrees Celsius [°C]) at which the gas was extracted. Preferred age shown in bold font. Colors of the isochron and text are arbitrary. %, percent; ka, kilo-annum; MSWD, mean square of weighted deviates.

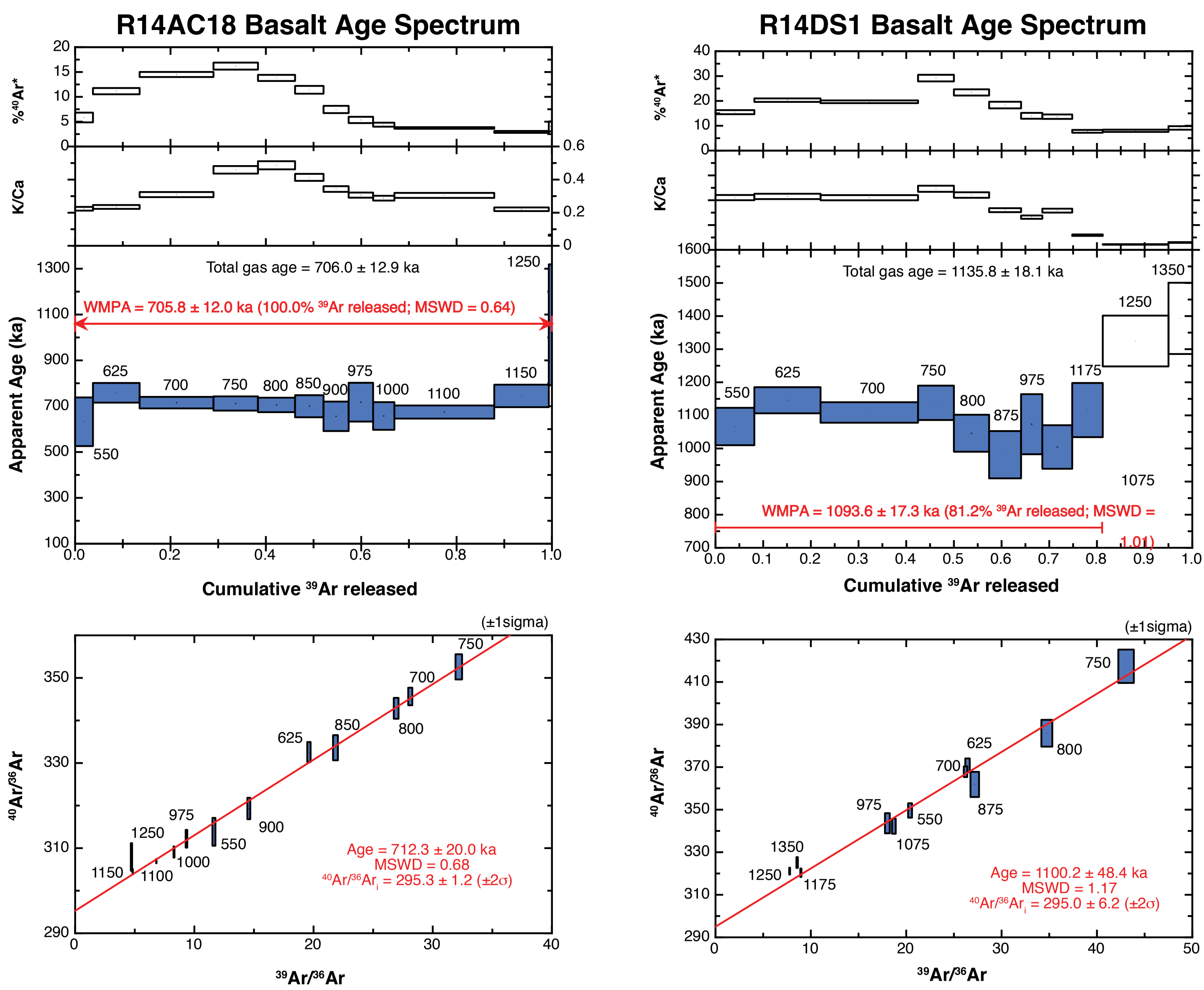

Figure 4.19. Argon age spectra (top plots) and isochron diagrams (bottom plots) for sample R14AC18 of the basalt of Dabaa 1 (unit bd1; left) and sample R14DS1 of the basalt of Gura 3 (unit bg3; right). Steps used in calculating the $^{40}Ar/^{39}Ar$ eruption age for each sample are shown in blue (in the age spectra and isochron diagram). Weighted mean plateau ages (WMPA) for the chosen steps are included in the argon age spectra diagram. Isochron ages for the chosen steps are included in the isochron diagram. See table 1 in the main text for a summary of all $^{40}Ar/^{39}Ar$ eruption ages and see Stelten (2021) for the full argon dataset. Uncertainties in plotted data points and reported ages are 1σ. Uncertainties for $^{40}Ar/^{36}Ar_i$ (the isochron intercept) are reported at the 2σ level. Numbers next to the data points correspond to the temperature (in degrees Celsius [°C]) at which the gas was extracted. Preferred age shown in bold font. Colors of the isochron and text are arbitrary. %, percent; ka, kilo-annum; MSWD, mean square of weighted deviates.

Moffett Field Publishing Service Center, California
Manuscript approved October 7, 2020
Edited by Monica Erdman
Layout and design by Kimber Petersen
Illustration support by JoJo Mangano

Stelten and others—**Magmatic Differentiation from Basalt to Trachyte within the Matan Volcanic Center**—Professional Paper 1862–F

ISSN 1044-9612 (print)
ISSN 2330-7102 (online)
https://doi.org/10.3133/pp1862F